NASS-31716

p-163

VISIBLE-INFRARED REMOTE-SENSING MODEL
AND APPLICATIONS FOR OCEAN WATERS

by

ZHONGPING LEE

A dissertation submitted in partial fulfillment
of the requirements for the degree of
Doctor of Philosophy
Department of Marine Science
University of South Florida

December, 1994

Major Professor: Kendall L. Carder, Ph.D.

ACKNOWLEDGEMENTS

TABLE OF CONTENTS

i

LIST OF TABLES

LIST OF FIGURES

LIST OF SYMBOLS

Symbols	units	Description
a	m^{-1}	Total absorption coefficient, $a_w + a_g + a_p$
a_{dg}	m^{-1}	Absorption coefficient of the sum of detritus and gelbstoff
$a_{d,g,p,w,\phi}$	m^{-1}	Absorption coefficient of detritus, gelbstoff, particles, water, and pigments, respectively
$a.p.d.$	--	Average percentage difference, used to quantify the difference between the measured and modeled R_{rs}
$a_{\phi1,\phi2}$	m^{-1}	Absorption coefficient of pigments at the blue and red peaks, respectively
A_1	mg/m^3	Leading parameter for pigment concentration algorithm
A_2	--	Exponent parameter for pigment concentration algorithm
AOP	--	Apparent optical property
AVG$_{\lambda1}^{\lambda2}$	--	Average value in the range of λ_1 to λ_2
b	m^{-1}	Scattering coefficient
b_b	m^{-1}	Backscattering coefficient
$b_{bw,bp}$	m^{-1}	Backscattering coefficient of pure sea waters, particles, respectively
b^R	m^{-1}	Water Raman scattering coefficient
B	m	Ratio of the volume filtered to the effective surface area on the filter pad

c	m^{-1}	Beam attenuation coefficient, $a + b$
[C]	mg/m^3	Concentration of phytoplankton pigments plus phaeo-pigments
[chl a]	mg/m^3	Concentration of phytoplankton pigments
$D_{d,u}$	--	Distribution function for downwelling, upwelling light field, respectively
$\{D_d\}$	--	Vertically averaged downwelling distribution function
$E_{d,u}$	W/m^2	Downwelling, upwelling irradiance, respectively
E_o	W/m^2	Scalar irradiance
$E_{od,ou}$	W/m^2	Downwelling, upwelling scalar irradiance, respectively
E_o^q	Ein/m^2	Quantum scalar irradiance
E_u^w	W/m^2	Upwelling irradiance from water column (elastic scattering only)
f	--	Parameter to adjust the measured a_p
F	--	Parameter to simulate a_ϕ
g	--	Constant to relate R_{rs} and b_b/a
G	--	Constant to relate R and b_b/a
H	m	Water depth
I	W/sr	Radiant intensity
IOP	--	Inherent optical property
j	radian	Subsurface solar zenith angle
k	m^{-1}	Diffuse attenuation coefficient of radiance
$K_{d,u}$	m^{-1}	Diffuse attenuation coefficient of downwelling, upwelling irradiance, respectively
L	W/m^2/sr	Radiance

$L_{A,G,R,t}$	W/m^2/sr	Radiance for aerosol, diffuse reflector, Rayleigh scattering, and total
$L_{d,u}$	W/m^2/sr	Radiance in downwelling, upwelling hemisphere, respectively
L_{sky}	W/m^2/sr	Radiance from sky light which enters a remote sensor by the surface reflectance
L_u^w	W/m^2/sr	Upwelling radiance from water column (elastic scattering only)
L_w	W/m^2/sr	Water-leaving radiance
$L_w^{b,f,R,w}$	W/m^2/sr	Water-leaving radiance for bottom reflectance, gelbstoff fluorescence, water Raman scattering and water column (elastic scattering only), respectively
n_w	--	Refractive index of sea water
OD	--	Optical density
PAR	Ein/m^2/s	Photosynthetic available radiance
PP	mol C/m^3	Primary production
Q	sr	Ratio of irradiance to radiance
Q_m	sr	"Q factor" for molecular scattering
R	--	Irradiance reflectance
R_G	--	Reflectance of a diffuse reflector
R_{rs}	sr^{-1}	Remote-sensing reflectance
$R_{rs}^{b,f,R,w}$	sr^{-1}	Remote-sensing reflectance from bottom reflectance, gelbstoff fluorescence, water Raman scattering, and water column (elastic scattering only), respectively
R^w	--	Irradiance reflectance from water column (elastic scattering only)

$S_{d,g,dg}$	nm^{-1}	Spectral slope of absorption coefficient of detritus, gelbstoff, and the sum of detritus and gelbstoff, respectively
t	--	Air-sea interface transmittance
$T_{b,p}$		Transmission spectra of the blank pad, sample pad, respectively
[YS]		Concentration of gelbstoff (yellow substance)
α	radian	Scattering angle
$\alpha_{b,f}$	radian	Scattering angle in the backward, forward direction, respectively
β	m^{-1}sr^{-1}	Volume scattering function (VSF)
$\beta_{w,p}$	m^{-1}sr^{-1}	VSF of pure sea water, particles, respectively
$\overline{\beta}_b$	m^{-1}sr^{-1}	Light-averaged-backward-VSF
β_{ie}	m^{-1}sr^{-1}	Volume scattering function of inelastic scattering
β_{pad}	--	Path-length elongation factor of filter pad
Δ	--	Offset of sun glint due to waves or foam
φ	radian	Azimuth angle
ϕ	mol C/Ein	Quantum yield of photosynthesis
ϕ_m	mol C/Ein	Maximum quantum yield of photosynthesis
γ	--	Ratio of [chl a] to total pigment concentration [C]
κ	m^{-1}	Quasi-diffuse attenuation coefficient, $a + b_b$
λ	nm	Wavelength
λ_x	nm	Excitation wavelength for inelastic scattering
η	--	Quantum efficiency of gelbstoff fluorescence

η_b	--	Exponent for particle backscattering coefficient
ψ	m^{-1}nm^{-1}	Inelastic scattering coefficient
τ	--	$= \kappa H$, diffuse optical length
$\tau_{A,G}$	--	Optical length of air, gas, respectively
$\overline{\mu}_{d,u}$	--	Average cosine for downwelling, upwelling irradiance, respectively
ρ	--	Bottom albedo
r	--	Fresnel reflectance
Θ	radian	Zenith angle
$\Theta_{a,w}$	radian	Zenith angle of water-leaving radiance in the air, water, respectively
ν	m^2/Ein	Photoinhibition parameter
ω	sr	Solid angle

VISIBLE-INFRARED REMOTE-SENSING MODEL
AND APPLICATIONS FOR OCEAN WATERS

by

ZHONGPING LEE

An Abstract

Of a dissertation submitted in partial fulfillment of
the requirements for the degree of
Doctor of Philosophy
Department of Marine Science
University of South Florida

December 1994

Major Professor: Kendall L. Carder, Ph.D.

Remote sensing has become important in the ocean sciences, especially for research involving large spatial scales. To estimate the in-water constituents through remote sensing, whether carried out by satellite or airplane, the signal emitted from beneath the sea surface, the so called water-leaving radiance (L_w), is of prime importance. The magnitude of L_w depends on two terms: one is the intensity of the solar input, and the other is the reflectance of the in-water constituents. The ratio of the water-leaving radiance to the downwelling irradiance (E_d) above the sea surface (remote-sensing reflectance, R_{rs}) is independent of the intensity of the irradiance input, and is largely a function of the optical properties of the in-water constituents.

In this work, a model is developed to interpret R_{rs} for ocean water in the visible-infrared range. In addition to terms for the radiance scattered from molecules and particles, the model includes terms that describe contributions from bottom reflectance, fluorescence of gelbstoff or colored dissolved organic matter (CDOM), and water Raman scattering. By using this model, the measured R_{rs} of waters from the West Florida Shelf to the Mississippi River plume, which covered a [chl a] (concentration of chlorophyll a) range of 0.07 - 50 mg/m^3, were well interpreted. The average percentage difference (a.p.d.) between the measured and modeled R_{rs} is 3.4%, and, for the shallow waters, the model-required water depth is within 10% of the chart depth.

Simple mathematical simulations for the phytoplankton pigment absorption coefficient (a_ϕ) are suggested for using with the R_{rs} model. The inverse problem of R_{rs}, which is to analytically derive the in-water constituents from R_{rs} data alone,

can be solved using the a_ϕ functions without prior knowledge of the in-water optical properties. More importantly, this method avoids problems associated with a need for knowledge of the shape and value of the chlorophyll-specific absorption coefficient. The simulation was tested for a wide range of water types, including waters from Monterey Bay, the West Florida Shelf and the Mississippi River plume. Using the simulation, the R_{rs}-derived in-water absorption coefficients were consistent with the values from in-water measurements ($r^2 > 0.94$, slope ~ 1.0).

In the remote-sensing applications, a new approach is suggested for the estimation of primary production based on remote sensing. Using this approach, the calculated primary production (*PP*) values based upon remotely sensed data were very close to the measured values for the euphotic zone ($r^2 = 0.95$, slope 1.26, and 32% average difference), while traditional, pigment-based *PP* model provided values only one-third the size of the measured data. This indicates a potential to significantly improve the accuracy of the estimation of primary production based upon remote sensing.

Abstract Approved: _____

Major Professor: Kendall L. Carder, Ph.D.

Date Approved: *Oct, 25, 1994*

INTRODUCTION

Introduction to Remote Sensing

Remote sensing has become an important tool in the study of ocean science, especially for the synoptic research of large bodies of water, because a large region of the world oceans can be viewed by a remote sensor in a very short time. For example, the Nimbus-7 and TIROS satellites had repeat cycles of 2 days at the equator with $>$ 1 km pixel diameter; at the other end of the scale, however, a blimp can transit Tampa Bay in mere hours measuring at high resolution ($\sim$ 8 x 8 m^2) and lingering long enough to observe changes with time.

The main purpose of oceanic remote sensing in the visible-infrared region of the spectrum is to remotely derive concentrations of certain constituents in the water (principally phytoplankton, dissolved organic matter and suspended inorganic sediments), to estimate the oceanic primary production and to understand ocean circulation. The derivation of these constituents through remote sensing, whether by satellite or aircraft, depends on the signal emitted from beneath the sea surface, the so called water-leaving radiance $L_w(\lambda)$ (definitions of variables are in the List of Symbols; the functionality of one variable to another may not be explicitly expressed unless it is needed for further clarity), or the spectrally digitized water color. There

are two approaches to formulate this derivation from measured L_w: one is empirical, and the other is analytical. The empirical approach, such as the Coastal Zone Color Scanner (CZCS) algorithm for pigments [Gordon et al. 1983], is most often used at present.

The empirical approach is based on observations of the change of water color (spectral ratios) as change of water constituents, and statistical methods are used to find the apparent relationship of one variable to another. Ocean waters show a wide variation of colors, ranging from dark blue through blue/green, green, and green/yellow [Jerlov 1976]. For clear sky days, blue water is usually found in the open ocean, where the water is clear, deep, and very few light absorbers such as phytoplankton are present. Pure sea water (which means the sea water without suspended particles and dissolved organic materials) is a good absorber for wavelengths longer than 570 nm [Smith and Baker 1981]. For upwelling regions, water color turns to green due to the increased concentration of phytoplankton and its associated degradation products (gelbstoff and detritus), which are strong absorbers in the blue/green bands [Jeffrey 1980, Bricaud et al. 1981, Roesler et al. 1989]. For coastal (especially shelf) regions, gelbstoff (yellow substance) or colored dissolved organic matter (CDOM) is abundant due to land run-off and absorbs strongly in the blue, turning the water to greenish yellow colors.

Based on the above observations, it is easy to qualitatively scale the concentrations of in-water constituents such as chlorophyll a ([chl a]) and gelbstoff ([YS]) based on ocean color, and this is the basis for the CZCS algorithm.

The CZCS algorithm is a power law of the ratio of $L_w(443)/L_w(550)$, which was empirically developed. Its accuracy in deriving pigment concentration is about a factor of 2 [Gordon and Morel 1983] for the oligotrophic ocean, and is much worse for coastal waters. This is because the water color is affected by constituents in addition to chlorophyll alone, especially in coastal areas. Water color signals, as observed immediately above the ocean's surface, depend upon the incident irradiance and the concentration and distribution of the in-water constituents. The waters will appear bluer on a bright, sunny day than on an over-cast cloudy day as there is relatively more blue light entering the sensor from reflected sky light rather than cloud light. At the same time, in-water constituents which can affect the water color include chlorophyll, gelbstoff, detritus, bacteria, and inorganic particles. Transpectral responses (water Raman scattering, gelbstoff fluorescence) and bottom reflectance further complicate matters. This is why simple ratios of L_w's do not always work well to derive [chl a] [Carder et al. 1986], especially for coastal waters, when there may be a strong bottom influence. Figure 1 illustrates the schematic relationships between water-leaving radiance and in-water components.

Since there are many components in the water which can affect the water color, it is necessary to separate their individual influences if we want to improve the algorithm. This favors the analytical approach. For the purpose of deriving in-water constituents, first it is essential to understand how each component affects the optical signal. Only after this step, can we have the potential to analytically derive the individual component from the remotely measured signal alone. So, there are two

sensor

$E_d(\lambda)$ $L_w(\lambda)$

$$R_{rs}(\lambda) = \frac{L_w(\lambda)}{E_d(\lambda)}$$

L^f

L^R

$a(\lambda), \ \beta(\lambda)$

chl a, YS, ...

L^b

bottom
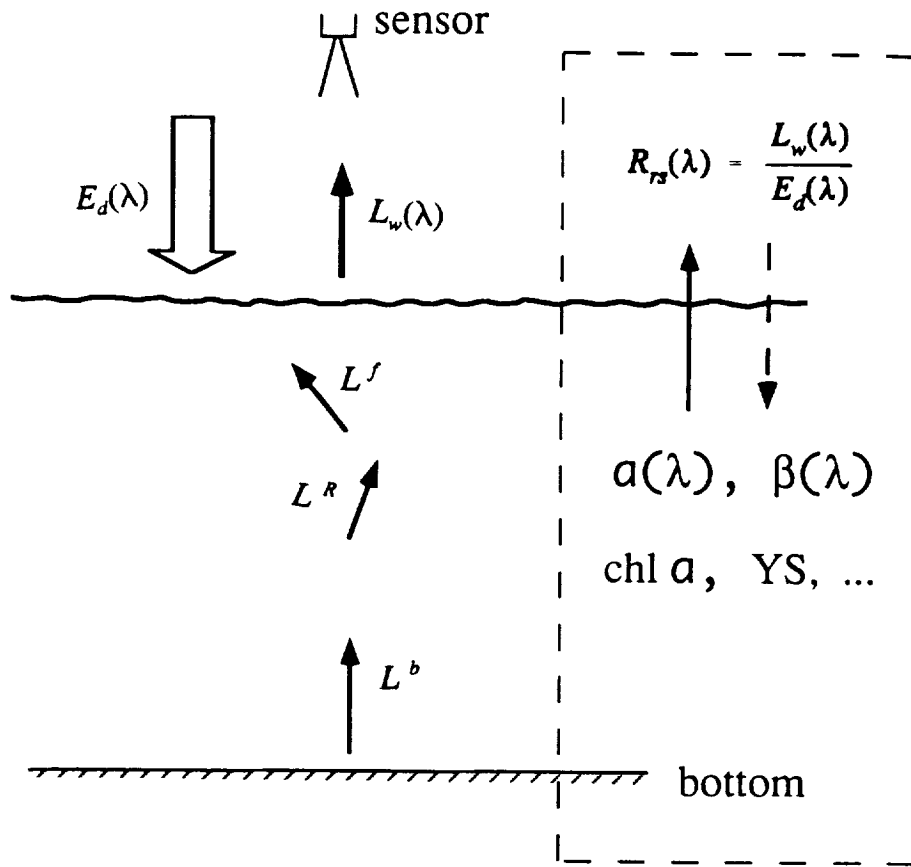
Figure 1. Schematic Relationships between Water Color and In-water Constituents.

steps to the analytical approach as pointed out by Morel [1980]. For the remote-sensing technique, first is the forward step (or the forward problem), i.e., to interpret the observed color based on the measurement of each component (solid arrow in the box of Figure 1); second is the backward step (or the inverse problem), i.e., to derive each component just from the remotely measured signal (dashed arrow in the box of Figure 1).

The forward problem can largely be solved based upon measurements of the optical components. If a few parameters prove difficult to measure, they may be

simulated based on theoretical grounds. This step is important not only for the understanding of the optical scenario, but also for the guidance of future theoretical and experimental studies.

In the forward problem, as upwelling light depends upon the intensity of input irradiance, subsurface irradiance reflectance $(R(0^-))$ and remote-sensing reflectance (R_{rs}) are defined as the ratio of upwelling irradiance to downwelling irradiance just below the surface and the ratio of the water-leaving radiance (L_w) to the downwelling irradiance (E_d) above the sea surface, respectively. In this way, $R(0^-)$ and R_{rs} will be independent of the intensity fluctuation of the input irradiance, and largely a function of the optical properties of the in-water constituents. Since E_d can be very precisely predicted from models [Gregg and Carder 1990, Bishop and Rossow 1991], it is easy to calculate L_w if we know how to accurately determine R_{rs}.

Optical models have been developed for the subsurface irradiance reflectance $R(0^-)$ [Gordon et al. 1975, Morel and Prieur 1977, Gordon 1989b, Kirk 1984, 1991], but satellites measure the upwelling radiance above the water surface. To use satellite radiance data, it is necessary to know how to interpret remote-sensing reflectance instead of irradiance reflectance. Models were suggested by Carder and Steward [1985], and Peacock et al. [1990] to explain the measured R_{rs}, but in each case no bottom reflectance, gelbstoff fluorescence, or water Raman scattering were included. Also, in these works a somewhat arbitrary "Q factor" [Austin 1974] was used.

For the open ocean, in-water constituents are dominated by phytoplankton particles and their derivatives. As a result, R_{rs} is easier to interpret, and is largely

dependent on the concentration of chlorophyll. For these "case 1" [Morel and Prieur 1977] waters, Monte Carlo simulations [Gordon et al. 1988, Morel and Gentili 1993] have been made for $R_{rs}(0^-)$. However, it is not clear whether these simulations can be used for "case 2" waters due to the different volume scattering functions and larger chlorophyll a concentrations.

For coastal waters, as discussed previously, components such as land run-off, suspended sediments and bottom reflectance, which do not co-vary with [chl a], confound the data interpretation. Also, the concentration of gelbstoff in coastal waters is frequently high and can fluoresce strongly in the blue-green region [Coble et al. 1990 and references cited], but it is not clear how this fluorescence might affect the remote-sensing reflectance. Further, it has been found that water Raman scattering can contribute as much as about 10% to the sub-surface irradiance reflectance in the open ocean [Stavn 1988, 1990], but how this would influence the R_{rs} is not clear.

For shallow coastal waters, part of the water-leaving radiance is frequently due to bottom reflectance, so, for the derivation of [chl a] from R_{rs}, the influence of the bottom reflectance needs to be removed first. How we express the bottom influence in R_{rs} needs further development.

For water-depth measurements [Polcyn et al. 1970, Clark et al. 1987] or bottom-feature mapping [Lyzenga 1978], the diffuse attenuation coefficient [Clark et al. 1987] or an "effective" attenuation coefficient [Lyzenga 1978] was used. For shallow water $R(0^-)$, Spitzer and Dirks [1987] used 3.7 a (the total absorption

coefficient) to represent the "effective" attenuation coefficient. It is not clear,

however, how to express the "effective" attenuation coefficient for R_{rs}.

The inverse problem is to use remotely measured data to derive the absorption

and scattering properties and to estimate in-water constituents such as [chl a], [YS],

etc. These derived values can be used to model the spectral light at depth

[Sathyendranath and Platt 1988] and/or to estimate primary production [Morel 1988,

Balch et al. 1992]. Analytically, not much improvement has been made for the

inverse problem in the past studies, mainly because it is not easy to accurately express

the change of each component by a few parameters.

In the application of remote sensing, empirical and semi-analytical approaches

have been studied in the estimation of [chl a], and efforts have been made to estimate

the primary production based on pigment concentration and empirical chlorophyll-

specific absorption coefficients [Morel 1991, Platt et al. 1991, Balch et al. 1992].

But, as the chlorophyll-specific absorption coefficient varies significantly from sample

to sample [Morel and Bricaud 1981, Bricaud and Stramski 1990, Carder et al. 1991,

Carder et al. 1994], the concentration of chlorophyll cannot be derived accurately

from remote sensing without prior knowledge of the chlorophyll-specific absorption

coefficient, which will further influence the primary production. Therefore, for cases

where only water-leaving radiance (or remote-sensing reflectance) is available, better

methods are needed for the derivation of the in-water absorption coefficient and the

estimation of primary production.

The Present Study and Structure

This contribution uses in-water and remote-sensing optical data to develop methodologies that can be used with present and new aircraft and spacecraft sensors to quantify biological, chemical and physical properties of the surface waters from open ocean to coastal waters.

In this study, a mathematical model is first developed to interpret the remote-sensing reflectance (solid arrow in the box of Figure 1) based on previous theoretical and experimental studies. In the model, terms to describe contributions from bottom reflectance, gelbstoff fluorescence and water Raman scattering are developed. In addition, hyperspectral R_{rs} measurements taken from waters ranging from the West Florida Shelf to the Mississippi River plume are selected to demonstrate the model. Differences between the modeled and measured R_{rs} are discussed.

Second, new approaches are suggested for the inverse problem (dashed arrow in the box of Figure 1), which include mathematical and empirical simulations for the absorption curves of phytoplankton pigments (a_ϕ). With these simulations, R_{rs} or upwelling radiance above the surface ($L_u(0^+)$) can be modeled when there are no in-water measurements available. Alternatively the in-water absorption coefficient can be derived from remote signals alone, and the spectral light field at depth as well as the primary production can be calculated.

Part A of this manuscript describes the optical basis of remote sensing and the model development. It is divided into 4 chapters: Chapter 1, the optical properties of

Table 1. Cruise Information where Data Were Collected and Used in this Study.

Cruise Name	Location	Period	Water Type
Monterey (MA)	Monterey Bay	Sep. 1989	green
Monterey (MB)	Monterey Bay	Oct. 1989	green
TBX1 (TA)	West Florida Shelf	Mar. 1990	shallow, green
ML-ML1 (ML)	North Atlantic	May-June 1991	blue
TBX2 (TB)	West Florida Shelf	May 1992	green, blue
GOMEX (GO)	Gulf of Mexico	April 1993	green, blue
COLOR (CO)	Gulf of Mexico	May-June 1993	dark, green
SHAMU (SH)	Tampa Bay	Jan. 1993	shallow

Note: Characters in parentheses will be used in text and tables as a short name.

pure sea water, gelbstoff and phytoplankton pigments, and the relationships between the apparent and inherent optical properties; Chapter 2, model development for remote-sensing reflectance; Chapter 3, data used and measurement methods; Chapter 4, model results; and Chapter 5, conclusions of part A. Part B presents the ways to solve the inverse problem and discusses some applications of remote sensing: Chapter 6, the methods suggested to solve the inverse problem; Chapter 7, comparisons of the derived absorption coefficient from R_{rs} inversion and that from K_d; Chapter 8, discussion of the remote-sensing applications, with a focus on primary production; Chapter 9, conclusions of part B; and Chapter 10, summary of this study and expectations for future work.

Data used in this study came from cruises during the period of 1989 to 1993,
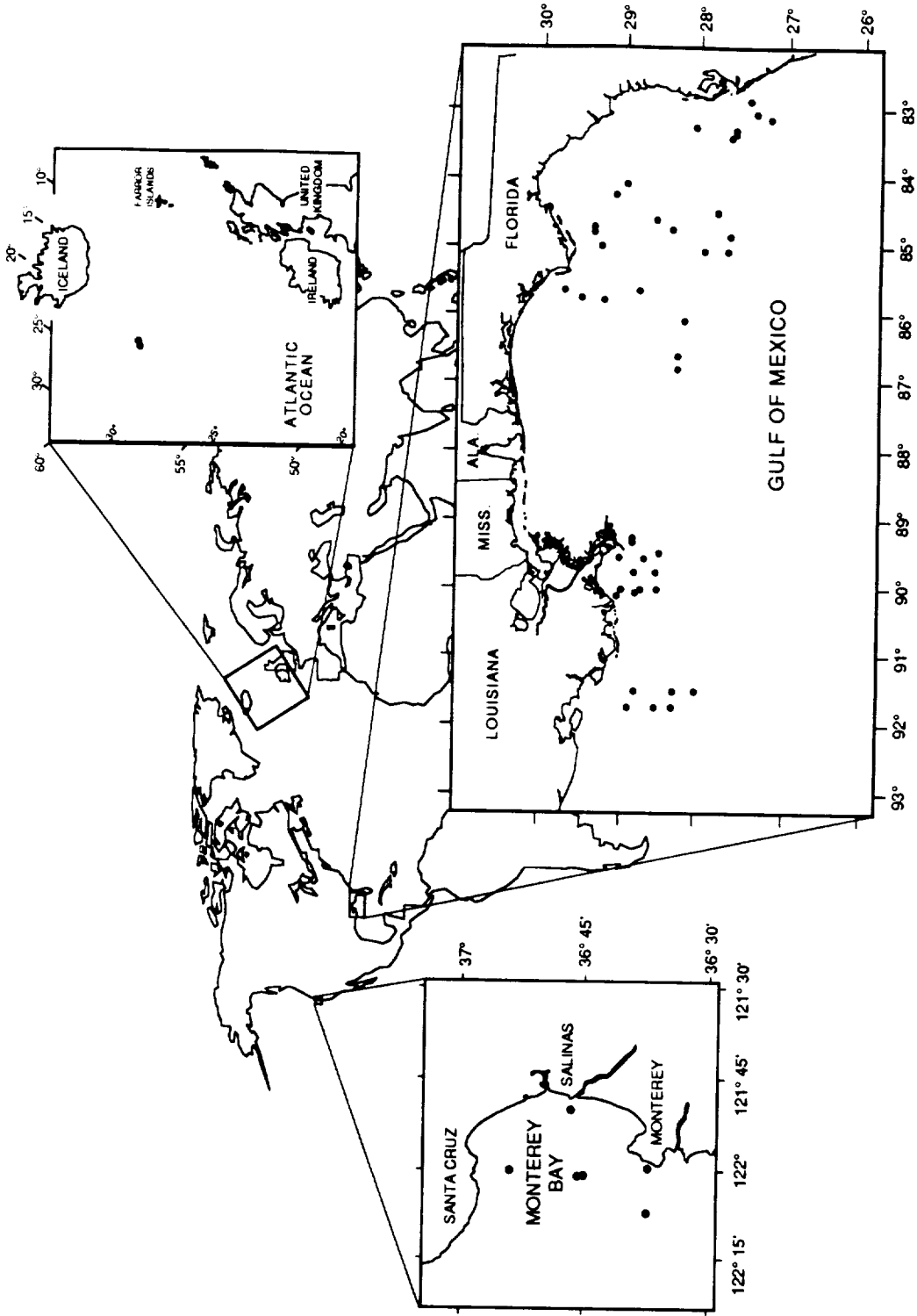
Figure 2a. Map of the Locations where Field Data Were Used.

which covered a wide range of water types, such as high-latitude North Atlantic waters; sub-tropic waters of Monterey Bay; gelbstoff rich, shallow waters of the West Florida Shelf; clear waters in the Loop Current; and the phytoplankton bloom waters in the Mississippi River plume. Table 1 summarizes the cruise information, Figure 2a shows the locations of the data collection, and Figure 2b zooms in on the stations where R_{rs} curves are used for the model demonstration.
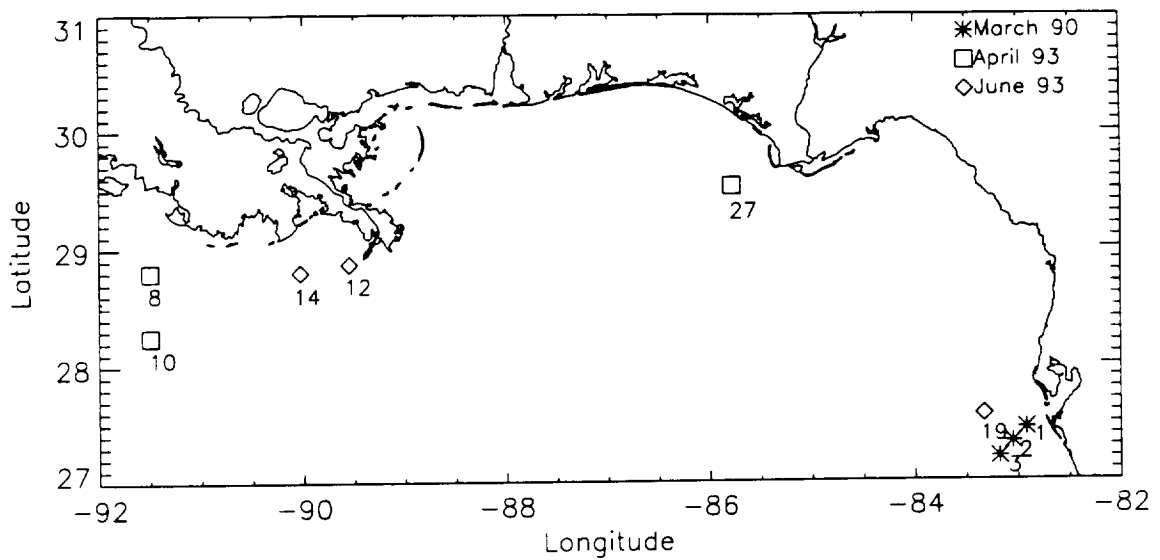
Figure 2b. Stations where Data Were Used to Demonstrate R_{rs} Model.

PART A

THE OPTICAL BASIS AND THE FORWARD PROBLEM

CHAPTER 1

APPARENT AND INHERENT OPTICAL PROPERTIES

1.1 Introduction

There are two kinds of optical properties which relate to the in-water constituents [Presendorfer 1976]: apparent optical properties (AOPs) and inherent optical properties (IOPs). AOPs are functions of both the light field and the in-water constituents, whereas IOPs have no relation to the light field and are solely dependent on the distribution and optical character of the in-water constituents. AOPs are easy to measure routinely in optical ocean studies, but difficult to relate to in-water constituents. For IOPs, the situation is reversed.

One goal of optical oceanography is to derive the IOPs from the AOPs, then to evaluate the physical, biological and/or chemical conditions of the water and global ocean. This process involves some optical quantities that can be measured directly, such as the radiance and irradiance fields. The connections between these optical quantities and the IOPs are through the AOPs. In this chapter, we will briefly discuss these optical quantities and properties.

1.2 Optical Quantities Describing the Light Field

The optical quantities used most widely in describing the light field are radiant

intensity, radiance, vector irradiance, and scalar irradiance:

Radiant intensity, $I(z,\Theta,\varphi)$, is defined as the flux of radiant energy per solid

angle in a specified direction, and has the units W/sr.

Radiance, $L(z,\Theta,\varphi)$, is the radiant intensity per unit area, i.e., $L = dI/dA$. The

area dA is perpendicular to the light beam. Radiance has the units W/sr/m^2.

Vector irradiance describes the total radiant intensity incident on a plane

surface. In ocean optics, two useful vector irradiances are defined: downwelling

irradiance, E_d, and upwelling irradiance, E_u. These two are the values of the

irradiance on the upper and lower faces, respectively, of a horizontal surface.

The relationships between radiance and the downwelling and upwelling

irradiance are as follow:

$$E_d = \int_{2\pi} L(\theta,\varphi)\cos(\theta)d\omega \ ,$$
$$E_u = -\int_{-2\pi} L(\theta,\varphi)\cos(\theta)d\omega \ ,$$

(1)

where the first expression is an integral over the up-looking hemisphere. The negative

sign before the second integral is used to force E_u to be positive. Figures 3a and 3b

show examples of E_d and E_u spectra versus depth, respectively.

Scalar irradiance, E_o, is the total radiant intensity coming from all directions,
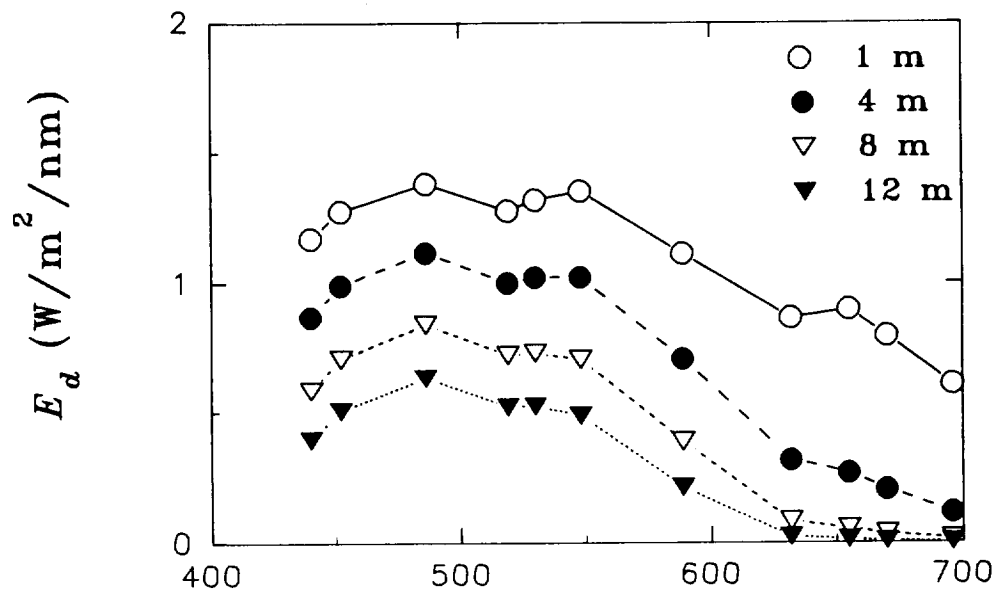
(a)
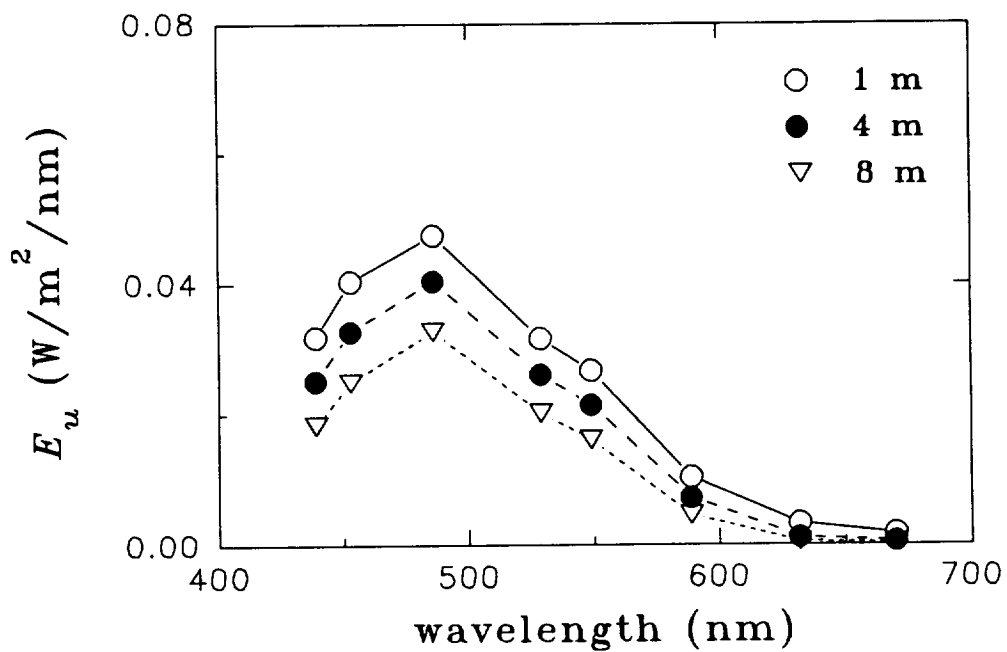
(b)

Figure 3. Examples of Downwelling (a) and Upwelling (b) Irradiance Spectra.
(Courtesy of Dr. J. L. Mueller)

measured at a point in space, so

$$E_o = \int_{4\pi} L(\theta,\varphi)d\omega \ .$$

(2)

This term is appropriate for evaluating the flux received by a phytoplankton cell.

It is useful to divide the scalar irradiance into downwelling (E_{od}) and upwelling (E_{ou}) components, which are integrals of the radiance distribution over the upper or lower hemisphere, respectively,

$$\begin{aligned} E_{od} &= \int_{2\pi} L(\theta,\varphi)d\omega \ , \\ E_{ou} &= \int_{-2\pi} L(\theta,\varphi)d\omega \ . \end{aligned}$$

(3)

Both vector and scalar irradiance have units of W/m^2.

1.3 Apparent Optical Properties (AOPs)

AOPs come from simple manipulation of the optical quantities and are jointly dependent on the IOPs and on the distribution of the ambient light field. The important AOPs are the irradiance reflectance (R), remote-sensing reflectance (R_{rs}), and the diffuse attenuation coefficients for downwelling (K_d) and upwelling (K_u) irradiance.

1.3.1 Irradiance Reflectance, R

Irradiance reflectance (or irradiance ratio), $R(z)$, is the ratio of the upwelling to
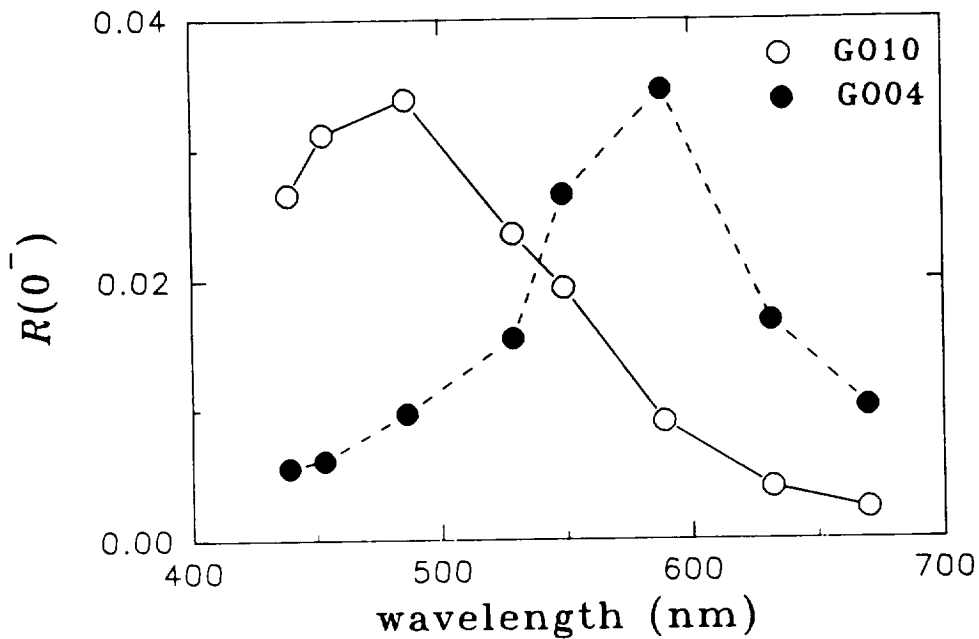
Figure 4. Examples of Irradiance Reflectance for Different Waters.
(Courtesy of Dr. J. L. Mueller)

the downwelling irradiance at a given depth z in the light field:

$$R(z) = \frac{E_u(z)}{E_d(z)} .$$
(4)

R has no units. Figure 4 shows examples of sub-surface R for two different

water types, where [chl a] was 0.12 mg/m^3 for GO10, and 7.4 mg/m^3 for GO04.

1.3.2 Remote-sensing Reflectance, R_{rs}

Remote-sensing reflectance, R_{rs}, is generally defined as the ratio of the

upwelling radiance to the downwelling irradiance at a given depth
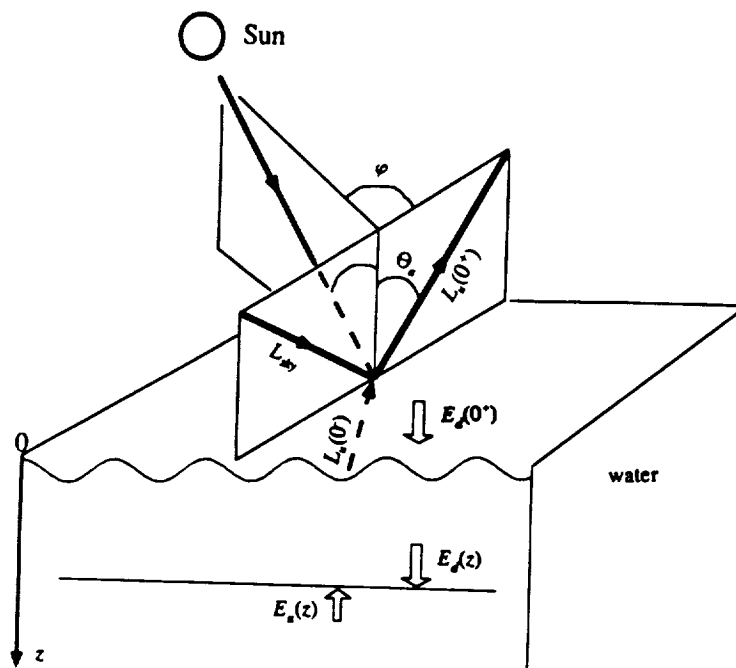
Figure 5. Light Geometry.
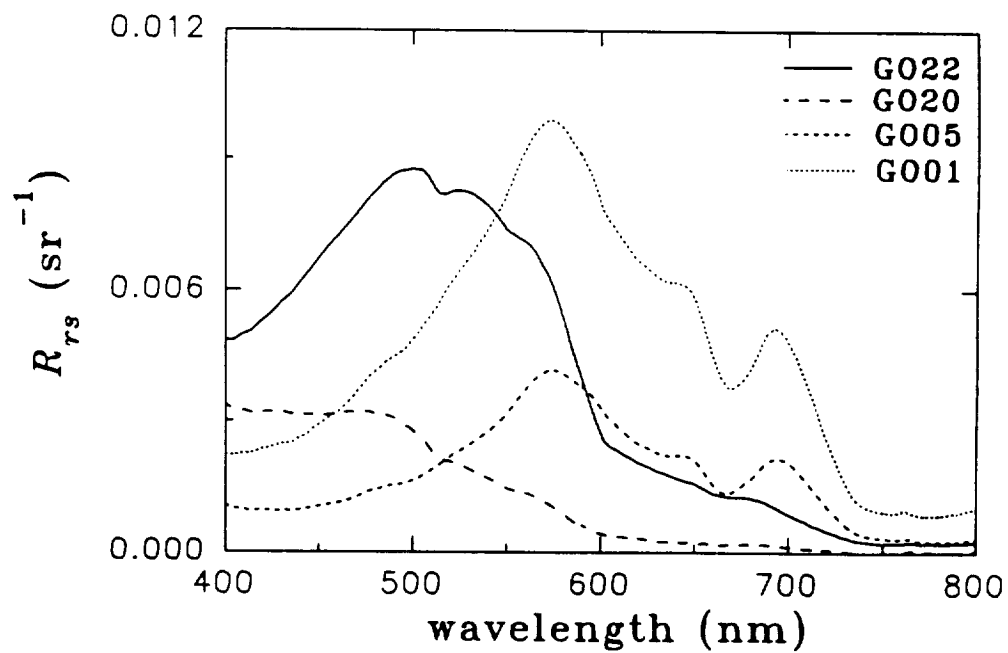
Figure 6. Examples of Remote-sensing Reflectance for Different Waters.

$$R_{rs}(z,\theta_w,\varphi) = \frac{L_u(z,\theta_w,\varphi)}{E_d(z)} , \qquad (5)$$

where Θ_w is the in-water zenith angle and φ is the azimuth angle from the solar

plane, respectively, for the upwelling radiance L_u. Figure 5 shows the light geometry.

R_{rs} has the units of steradian^{-1} (sr^{-1}). Since a satellite or aircraft sensor measures the

radiance leaving the water surface, a very useful form of R_{rs} is

$$R_{rs}(\theta_a,\varphi) = \frac{L_w(0^+,\theta_a,\varphi)}{E_d(0^+)} , \qquad (6)$$

i.e., the ratio of the water-leaving radiance to the downwelling irradiance just above

the surface. Where Θ_a is the in-air zenith angle of the water-leaving radiance, and

$\sin(\Theta_a) = n_w * \sin(\Theta_w)$ (n_w is the refractive index of sea water). In most cases, Θ_a is

within 30° and φ is about 90° from the solar plane for ship-board measurements. In

the following text, Θ and φ may not be explicitly shown for the sake of brevity.

Figure 6 shows examples of R_{rs} of different waters, with [chl a] of 16.2, 2.4, 0.6 and

0.5 mg/m^3 for stations GO01, GO05, GO20, and GO22, respectively.

1.3.3 Diffuse-attenuation Coefficient of Irradiance

This property is divided into two components; one for the downwelling

irradiance, K_d, and another for the upwelling irradiance, K_u. These represent the rate

of change of the natural log of the irradiance with depth,

$$K_d = -\frac{d \ln[E_d(z)]}{dz} ,$$

$$K_u = -\frac{d \ln[E_u(z)]}{dz} .$$

(7)

The minus before the derivative is to force K_d and K_u to be positive, as z is positive downward. The units for K are m^{-1}.

Similar to Lambert-Beer's Law [Gordon 1989a], this definition clearly indicates that, in any absorbing and scattering medium (in this case sea water), all the quantities describing the light field change with depth, z. The change is typically a decrease in E_d and E_u with increasing depth, in an approximately exponential manner. So it is convenient to specify the rate of change as the change of the natural logarithm of the value with depth. When the rate of change and value at one depth are known (e.g. K_d and $E_d(0^-)$), it is possible to estimate the value at another nearby depth for a well mixed ocean.

1.3.4 Distribution Function and Average Cosine

Distribution functions ($D_d(z)$ and $D_u(z)$) and average cosines ($\overline{\mu}_d(z)$ and $\overline{\mu}_u(z)$) for downwelling and upwelling light, respectively, are defined as

$$D_d(z) = \frac{1}{\overline{\mu}_d(z)} = \frac{E_{od}(z)}{E_d(z)}, \qquad D_u(z) = \frac{1}{\overline{\mu}_u(z)} = \frac{E_{ou}(z)}{E_u(z)} . \qquad (8)$$

These factors are simple means of characterizing the shape of the radiance distribution. For example, for completely diffused upwelling light, $D_u = 2.0$, $\overline{\mu}_u = 0.5$. For a collimated downwelling light beam, $D_d = \overline{\mu}_d = 1$.

In most oceanic cases, both D_d and D_u increase with depth, and $D_u/D_d \approx 2$ [Gordon et al. 1975]. For the downwelling distribution function just beneath the surface, $D_d(0) \approx 1/\cos(j)$, with an error of less than 3% for a clear-sky situation [Gordon 1989a], where j is the sub-surface solar zenith angle.

1.4 Inherent Optical Properties (IOPs)

IOPs are those that are independent of the ambient light field (i.e. independent of the intensity and the angular distribution). The important IOPs of any medium are the absorption coefficient, a, the scattering coefficient, b, and the volume scattering function (VSF), $\beta(\alpha)$, which expresses the magnitude and angular distribution of scattered photons. The angle α describes the direction change of the scattered photons from the input photons. An additional inherent optical property is the beam attenuation coefficient, c, given as

$$c = a + b.$$

The beam attenuation coefficient thus represents the fractional loss of photons from a collimated light beam due to absorption and scattering, with units m^{-1}.
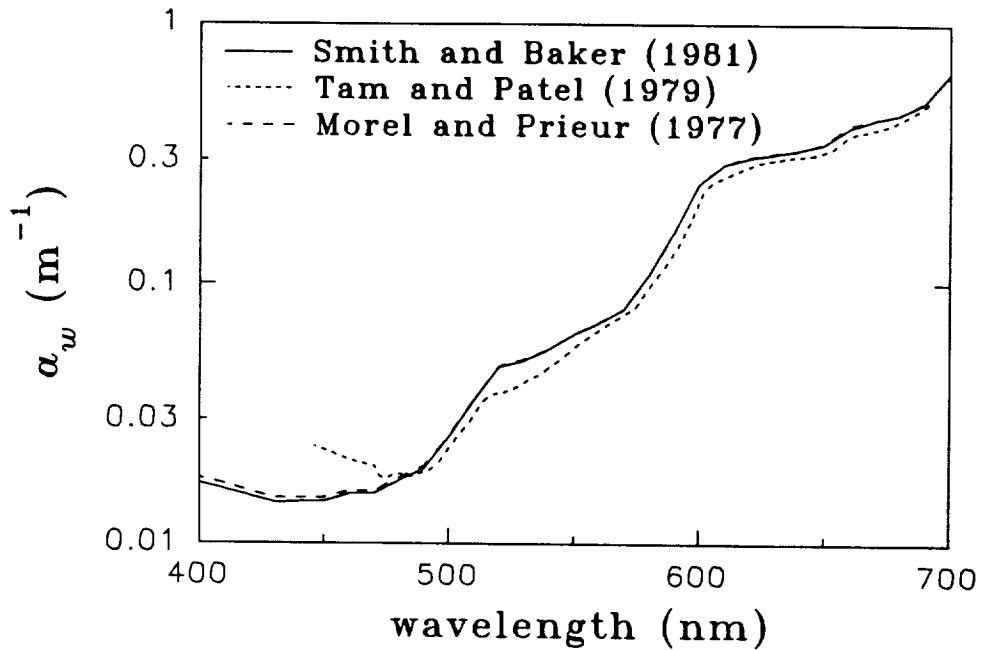
Figure 7a. Absorption Coefficients of Pure Water.

The absorption and scattering coefficients of water as a whole, at a given wavelength, are equal to the sum of the individual coefficients of the components present [Gordon et al. 1980].

1.4.1 Absorption Coefficient

There are three major components for the absorption coefficient of ocean water: water itself, a_w; suspended particles, a_p; and gelbstoff, a_g. a_p can be further divided into two components: the absorption coefficient of phytoplankton pigments, a_ϕ, and

the absorption coefficient of detritus, a_d. So:

$$a = a_w + a_g + a_p \text{ or } a = a_w + a_g + a_d + a_\phi.$$

1.4.1.1 Absorption Coefficient of Water Itself. The absorption coefficient of water itself is one of the most important optical components. Figure 7a shows three measured absorption spectra. Water absorbs light very weakly in the blue and green regions of the spectrum, but increases markedly as the wavelength rises above 570 nm, becoming quite significant in the red region. Also notice in the figure that there are some differences in a_w among researchers. The main reason is the difficulty in obtaining "pure" water for experiments (also see the discussion in Smith and Baker (1981)) and the long path length needed for accuracy at blue wavelengths. We will use the a_w values from Smith and Baker [1981] as their work is more recent and widely used. But, it must be remembered that the accuracy of their a_w was only +25% to -15% between 380 to 800 nm.

For wavelengths in the visible, a_w does not change much between fresh and salt waters [Morel 1974]. However, due to the dissolved ions in the sea water, a_w can change markedly for wavelengths in the UV range [Morel 1974].

Hojerslev and Trabjerg [1990] reported that a_w varies with temperature. However, their results differed from Pegau and Zaneveld [1993]. So, questions about how $a_w(\lambda)$ varies with temperature remain.
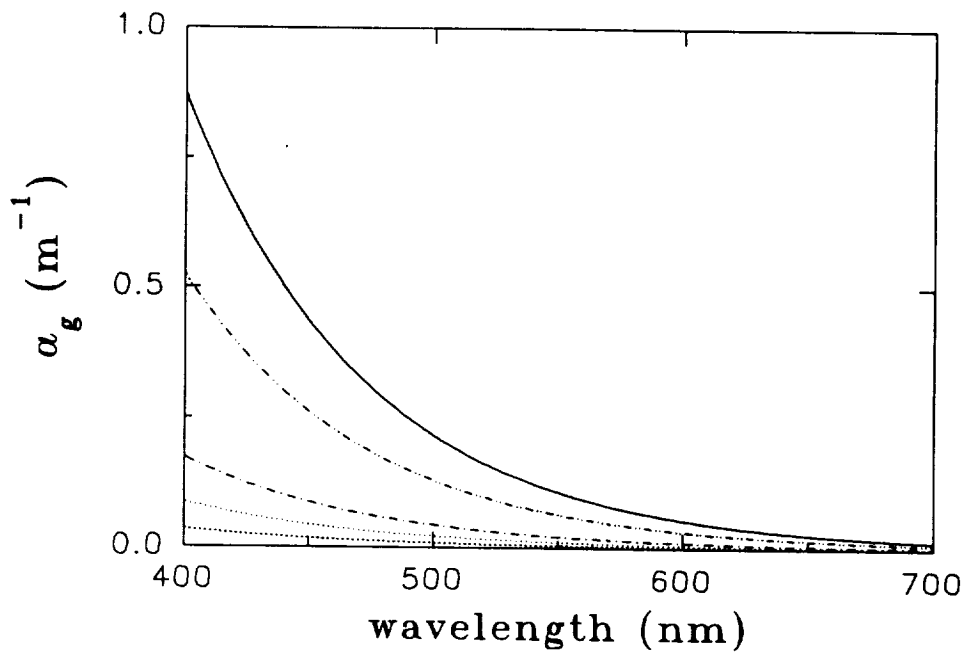
Figure 7b. Examples of Absorption Coefficients of Gelbstoff.

1.4.1.2 Absorption Coefficient of Gelbstoff. Figure 7b shows examples of the spectral

absorption coefficient of gelbstoff. It is a strong blue absorber with exponential

decrease with wavelength. This absorption coefficient can be expressed as [Bricaud et

al. 1981, Carder et al. 1989, Roesler et al. 1989]

$$a_g(\lambda) = a_g(440)e^{-S_g(\lambda-440)} .$$ (9)

The spectral slope S_g varies with different dissolved organic materials, which also

varies slightly with wavelength range [Krijgsman 1994]. At 440 nm, Carder et al.

[1989] found that $S_g \approx 0.011$ nm^{-1} for a marine humic acid and 0.019 nm^{-1} for a

marine fulvic acid. The average of S_g for ocean waters is reported as 0.014 nm^{-1}

[Bricaud et al. 1981, Kishino et al. 1984].
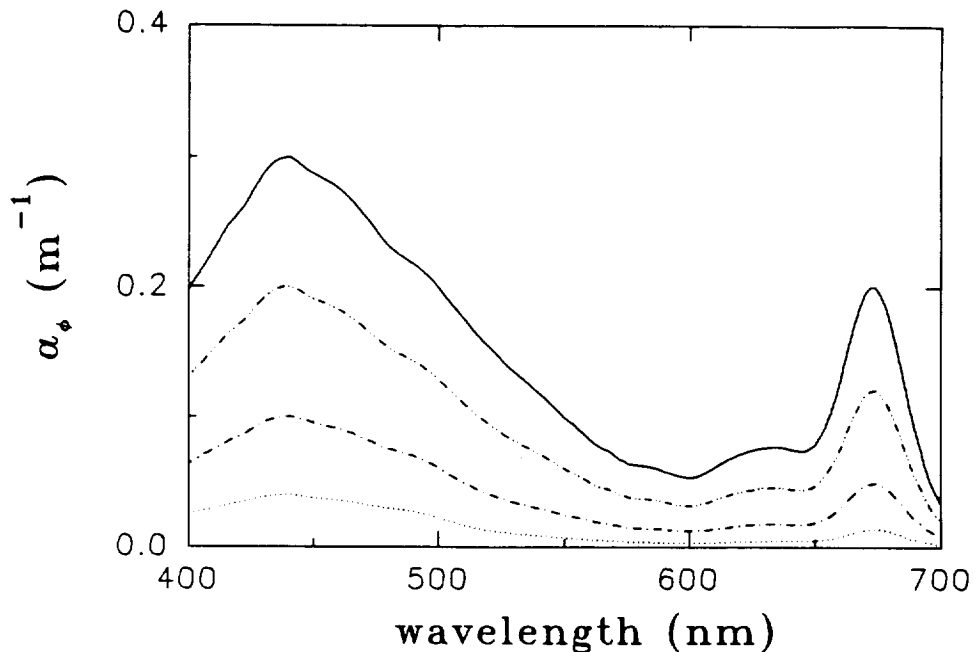
Figure 7c. Examples of Absorption Coefficients of Phytoplankton Pigments.

1.4.1.3 Absorption Coefficient of Phytoplankton Pigments. Figure 7c presents

examples of the spectral absorption coefficient of phytoplankton pigments, which are

the basis of oceanic photosynthesis. This spectrum typically has two peaks, one

around 440 nm, another around 675 nm. These are due to the presence of chlorophyll

a. The shoulders above 440 nm are due to the presence of the accessory pigments,

such as chlorophyll b, chlorophyll c and carotenoids. The width of the peaks around

440 nm and around 675 nm varies from sample to sample, due to the change in

accessory pigments present and the "package effect" [Morel and Bricaud 1981, Kirk

1986]. The "package effect" and the accessory pigments/chlorophyll a ratio also cause

the ratio $a_\phi(440)$ to chlorophyll concentration to be generally non-linear.
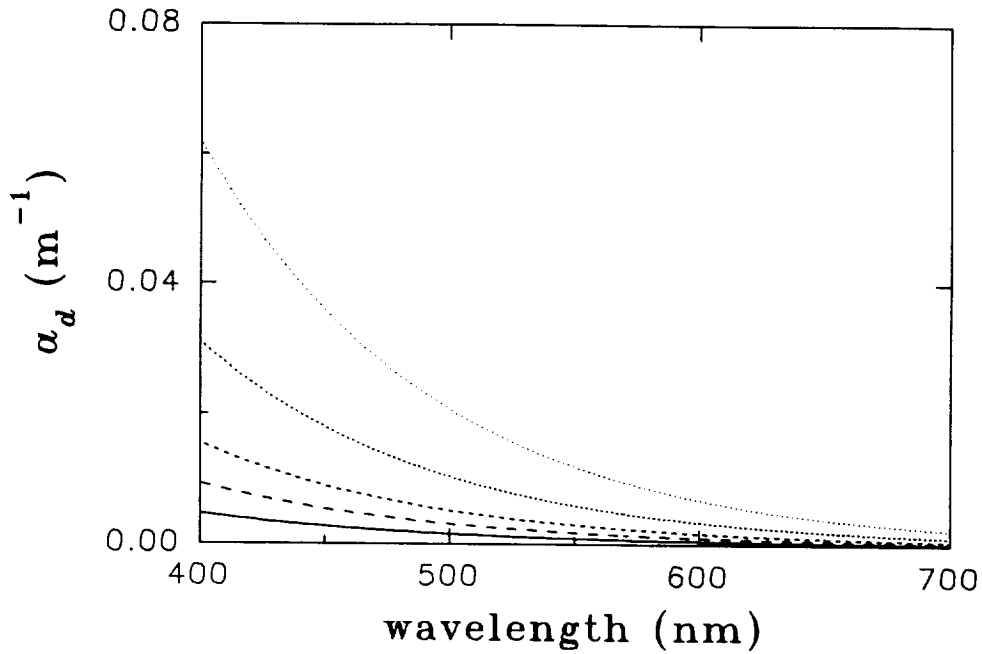
Figure 7d. Examples of Absorption Coefficients of Detritus.

1.4.1.4 Absorption Coefficient of Detritus. Figure 7d presents examples of the

spectral absorption coefficient of detritus. Like gelbstoff, it is a strong absorber in the

blue and exponentially decreases with wavelength, and can also be expressed as:

$$a_d = a_d(440)e^{-S_d(\lambda-440)}, \tag{10}$$

The spectral slope S_d has been reported in the range 0.009 to 0.011 nm^{-1} [Roesler et

al. 1989].

It has been found that the absorption coefficients for fulvic acid and

detritus can be combined. The sum can also be expressed in a form similar to Eqs. 9

and 10, but with an average slope at 440 nm of 0.011 nm^{-1} [Carder et al. 1991].

1.4.2 Volume Scattering Function and Scattering Coefficient

The scattering property of a substance is determined by its volume scattering function, $\beta(\alpha)$, which describes the probability of input photons being scattered to a specific angle, α. The scattering coefficient b is a measure of the sum of all the scattered photons (at all angles).

1.4.2.1 Volume Scattering Function, $\beta(\alpha)$. This property is defined as the scattered radiant intensity in the scattering angle α per unit scattering volume per incident irradiance. Figure 8a shows the VSF of sea water itself (β_w). As this is a molecular scattering mechanism, the scattering is symmetric between the forward and backward directions [Morel 1974].

Figure 8b shows the VSF of some natural waters [Petzold 1972]. Due to the presence of larger "soft," low-index particles, natural waters scatter photons strongly in the forward direction due to diffraction and refraction effects, and very weakly in the backward direction.

1.4.2.2 Scattering Coefficient, b. The integration of $\beta(\alpha)$ over 4π solid angle gives the total scattering coefficient. The scattering coefficient is divided into two parts: the forward scattering coefficient, b_f, and the back-scattering coefficient, b_b.
Mathematically they are
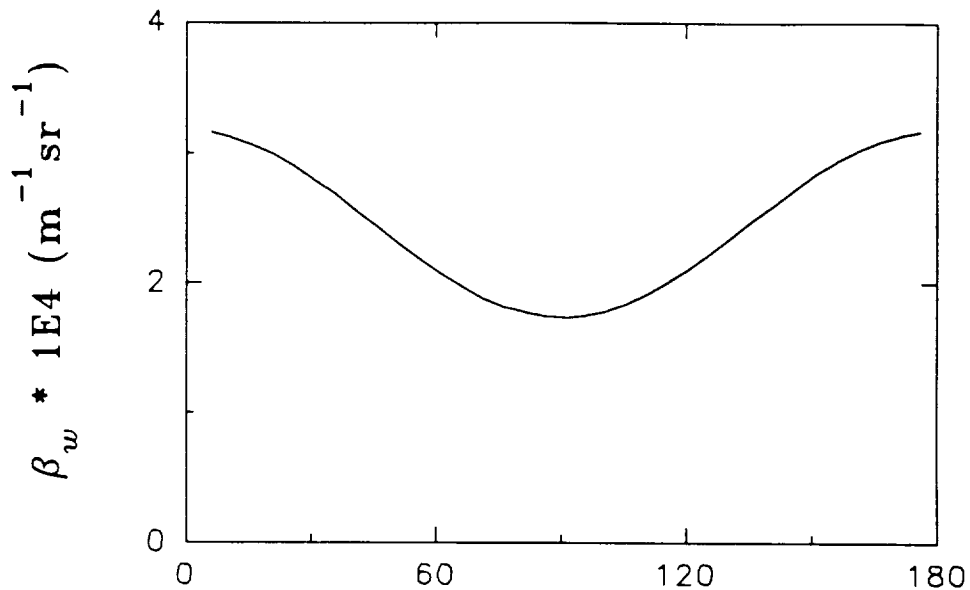
Figure 8a. Volume Scattering Function of Pure Sea Water.
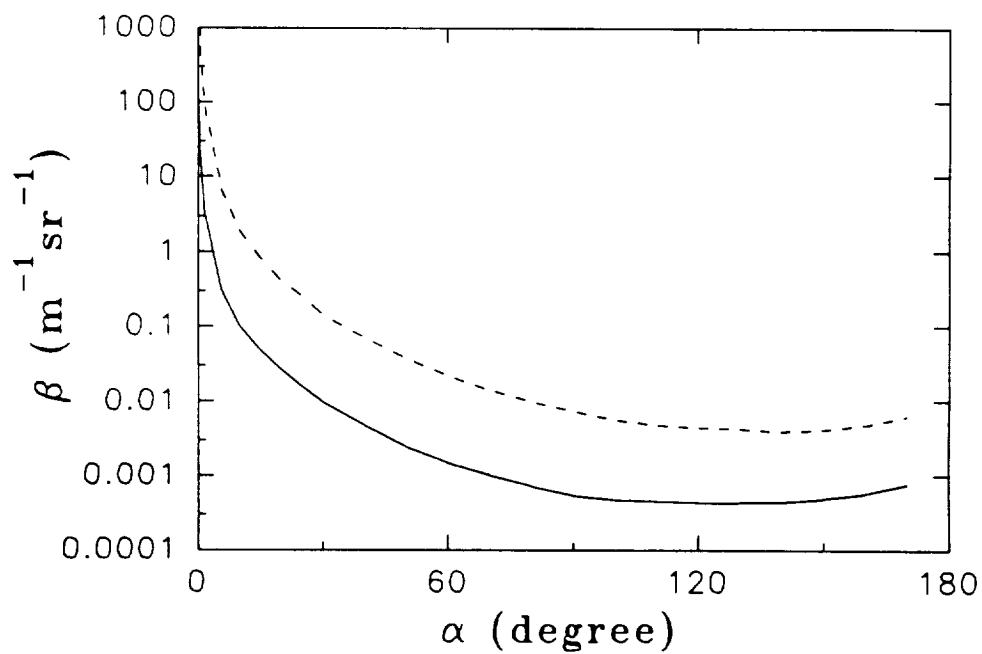
Figure 8b. Volume Scattering Function of Natural Waters.
(From Petzold [1972]).

$$b_f = 2\pi \int_0^{\frac{\pi}{2}} \beta(\alpha)\sin(\alpha)d\alpha,$$

$$b_b = 2\pi \int_{\frac{\pi}{2}}^{\pi} \beta(\alpha)\sin(\alpha)d\alpha. \tag{11}$$

and $b = b_f + b_b$. b_b is the major contributor to the upwelling radiance.

The back-scattering coefficient of sea water can be divided into two components: back-scattering coefficient of pure sea water, b_{bw}, and back-scattering coefficient of suspended particles, b_{bp}. Everything except molecular scattering is included in particle scattering.

Back-scattering coefficient of pure sea water, b_{bw}. Many theoretical and experimental studies have been carried out [e.g. Morel 1974, Smith and Baker 1981] on the back-scattering of pure sea waters. Figure 9 shows the spectrum of the back-scattering coefficient of pure sea water [Smith and Baker 1981], which can be expressed as

$$b_{bw}(\lambda) = b_{bw}(400)\left(\frac{400}{\lambda}\right)^{4.3}. \tag{12}$$

Due to the presence of ions and dissolved material, the scattering coefficient of pure sea water is $\sim 30\%$ higher than that of pure fresh water [Morel 1974].

Back-scattering coefficient of particles, b_{bp}. There are rare measurements of spectral b_{bp} for ocean waters, although a few measurements at single wavelengths have been made (e.g. Petzold 1972), and Whitlock et al. [1981] reported b_{bp} for river
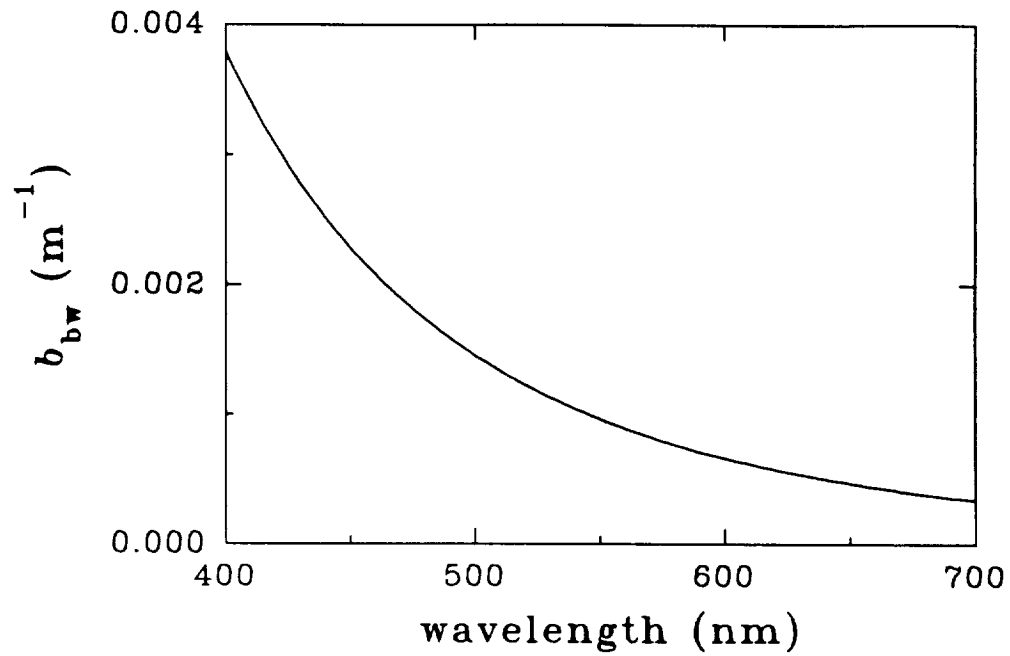
Figure 9. Spectrum of the Back-scattering Coefficients of Pure Sea Water.

samples. It is believed that $b_{bp}(\lambda)$ can be expressed as [Morel and Prieur 1977,

Bricaud et al. 1981, Smith and Baker 1981, Bricaud and Morel 1986, Gordon et al.

1988, Sathyendranath et al. 1989a, Morel and Ahn 1990]:

$$b_{bp}(\lambda) = b_{bp}(400)\left(\frac{400}{\lambda}\right)^{n_b},$$

(13)

with η_b in the range of 0 - 3 for different particles, while the data of Whitlock et al.

[1981] imply an η_b of 1.7 for their river samples.

1.5 Relationships between AOPs and IOPs

1.5.1 Sub-surface Irradiance Reflectance

From Eq. 4, the sub-surface irradiance reflectance, $R(0^-)$, is

$$R(0^-) = \frac{E_u(0^-)}{E_d(0^-)} .$$ (14)

The major contribution to $E_d(0^-)$ comes from the sun light and sky light. The contribution to $E_u(0^-)$, however, is dominated by the following four components [Peacock 1992]: elastic scattering from molecules and particles in the water column $(E_u^w(\lambda))$ and from bottom reflectance $(E_u^b(\lambda))$, and inelastic scattering from gelbstoff fluorescence $(E_u^f(\lambda))$ and water Raman scattering $(E_u^R(\lambda))$. Work by Gordon [1979] and Carder and Steward [1985] dealing with chlorophyll a fluorescence have been reported, but because the fluorescence efficiency of chlorophyll a varies by an order of magnitude and peak chlorophyll a fluorescence occurs in a narrow band centered around 685 nm, chlorophyll a fluorescence is not considered in this study.

For optically deep, homogeneous water, the irradiance reflectance due to the elastic scattering of molecules and particles, $R^w(0^-)$, can be expressed as [Gordon et al., 1975]:

$$R^w(0^-) = \sum_{m=0}^{3} G_m \left(\frac{b_b}{a+b_b} \right)^m. \tag{15}$$

Recently, extensive Monte Carlo simulations have been performed for various sun angles and VSFs [Kirk 1984, 1991; Jerome et al. 1988, Gordon 1989b, Morel and Gentili 1991], and it is found that for $b_b/a < 0.25$, generally,

$$R^w(0^-) \approx G(\overline{\mu}_d(0)) \frac{b_b}{a}, \tag{16}$$

where $G(\overline{\mu}_d(0))$, according to Kirk [1991], is

$$G(\overline{\mu}_d(0)) = M_1 \left(\frac{1}{\overline{\mu}_d(0)} - 1 \right) + M_2 , \tag{17}$$

M_1 and M_2 vary with VSF and range from 0.244 to 0.514 for M_1 and from 0.303 to 0.326 for M_2 (for VSFs reported in Petzold [1972]). Actually, the above expression can be approximated as

$$G(\overline{\mu}_d(0)) \approx \frac{G}{\overline{\mu}_d(0)} , \tag{18}$$

for sun angles $< 80°$ ($0.68 < \overline{\mu}_d(0) < 1.0$) with G varying from 0.304 to 0.344, and averaged to 0.32 ($\pm 7\%$) for the above M_1 and M_2 values. Keeping $G = 0.32$ as a constant and putting the 7% error to the other terms, then Eq. 16 is

$$R^w(0^-) \approx 0.32 D_d(0) \frac{b_b}{a}. \tag{19}$$

This is a re-write of Eq. 16, but it more explicitly shows the variation of $R^w(0^-)$ with solar zenith angle, as $D_d(0) = 1/\overline{\mu}_d(0) \approx 1/\cos(j)$ (section 1.3.4).

For parts due to inelastic scattering and bottom reflectance, there are no simple expressions like Eq. 19. Their contributions to the remote-sensing reflectance will be discussed in Chapter 2.

1.5.2 Remote-sensing Reflectance

Based on the above assumption about the major components which make up the sub-surface upwelling light field, to first order (single scattering and quasi-single scattering [Gordon 1994]) the water-leaving radiance can be expressed as

$$L_w = L_w^w + L_w^b + L_w^f + L_w^R. \tag{20}$$

Breaking Eq. 6 into contributions from the various mechanisms listed in Eq. 20, we have

$$R_{rs} = R_{rs}^w + R_{rs}^b + R_{rs}^f + R_{rs}^R. \tag{21}$$

From Austin [1974], there is

$$L_w \approx \frac{t}{n_w^2} L_u(0^-) . \tag{22}$$

where t is the air-sea interface transmittance. Since $E_d(0^+) = E_d(0^-)/t$, then from Eq. 6,

$$R_{rs} \approx \frac{t^2}{n_w^2} \frac{L_u(0^-)}{E_d(0^-)} = \frac{t^2}{n_w^2} R_{rs}(0^-) . \tag{23}$$

Similar to Zaneveld [1982, 1994], through the radiative transfer equation, the exact solution for nadir remote-sensing reflectance from the elastic scattering part of the water column, $R_{rs}^w(0^-)$, is

$$R_{rs}^w(0^-) \equiv \frac{\overline{\beta}_b}{c+k_L-\epsilon b_f} , \qquad (24)$$

where

$$\overline{\beta}_b = \frac{\int_{2\pi} \beta(\alpha_b) L_d(\theta') d\omega'}{\int_{2\pi} L_d(\theta')\cos(\theta') d\omega'} , \qquad (25)$$

is the light-averaged-backward-VSF (detailed in Appendix 1).

The terms for bottom reflectance and inelastic scattering will be discussed in Chapter 2 and appendices.

1.5.3 Diffuse-attenuation Coefficient of Downwelling Irradiance

Through Monte Carlo simulation, Gordon [1989a] found that

$$K_d(0) \approx 1.04 D_d(0)(a+b_b) , \qquad (26)$$

and

$$K_d(av) \approx 1.08 D_d(0)(a+b_b) , \qquad (27)$$

where $K_d(0)$ and $K_d(av)$ are the diffuse attenuation coefficient for the downwelling

irradiance just beneath the surface, and an average of K_d between the sub-surface E_d

and 10% of the sub-surface E_d value, respectively.

CHAPTER 2

MODEL OF THE REMOTE-SENSING REFLECTANCE

2.1 Introduction

One goal of ocean optics is to be able to interpret water color or remote-sensing reflectance in terms of the in-water constituents. From Eq. 21, we see that remote-sensing reflectance can be broken down into many terms. To interpret the measured remote-sensing reflectance on the left side of Eq. 21, each component on the right side of Eq. 21 needs to be expressed in terms of the optical properties of the water.

2.2 Remote-sensing Reflectance of the Water Column
(elastic scattering only), $R_{rs}{}^w$

In Eq. 24, $\overline{\beta}_b = \overline{\beta}_{bw} + \overline{\beta}_{bp}$, as $\beta = \beta_w + \beta_p$. $\overline{\beta}_b$ is the light-field-weighted average of the backward VSF. Thus, $\overline{\beta}_{bw}$ and $\overline{\beta}_{bp}$ can not be simply expressed using a few parameters, since they depend on the light field. Extensive calculations for different a, VSFs, and light fields are necessary.

For $j > 15°$ and a nadir viewing sensor, Gordon [1986] and Gordon et al. [1988] found through Monte Carlo simulation, that $R_{rs}{}^w(0^-)$ can be expressed as

$$R_{rs}^{w}(0^-) \approx \sum_{i=1}^{2} g_i \left(\frac{b_b}{a+b_b} \right)^i , \qquad (28)$$

where $g_1 = 0.0949$, and $g_2 = 0.0794$. More recently, Morel and Gentili [1993] made

Monte Carlo calculations for "case 1" waters ([chl a] $<$ 3 mg/m^3) using one VSF

shape for particles. For sun angles within 80° from zenith and for satellite viewing

angles ($\Theta_a < 50°$), they found

$$R_{rs}^{w}(0^-) \approx g\frac{b_b}{a}, \qquad (29)$$

where g averaged about 0.0936 (for 440 - 550 nm) and varied slightly with

wavelength, sun angle and view angle. But, as pointed out by Mobley et al. [1993], g

may vary with Monte Carlo computation models, and this variation can be 12% for

high scattering waters and much larger in high absorbing waters [Mobley et al. 1993].

Also, it is not clear yet how g varies for high [chl a] and "case 2" waters.

In another way, with the definition $Q = E_u(0^-)/L_u(0^-)$ [Austin 1974] and Eq. 16,

there is

$$R_{rs}^{w}(0^-) \approx \frac{G}{Q}\frac{b_b}{a}. \qquad (30)$$

This expression introduces a new parameter, the Q factor. However, only a few

measurements of Q exist. Q is extremely sensitive to sensor orientation, so its values

have been reported from 3.2 to 12 [Gordon et al. 1980]. For example, Austin [1979]

takes Q to be about 4.7 and spectrally constant from 440 to 550 nm, while Kirk

[1986] gives Q as ~4.9, and Gordon et al. [1975, 1988] suggest a value of ~3.4. In

some other studies, Q is somewhat arbitrarily chosen as a spectral constant [Carder

and Steward 1985, Peacock et al. 1990]. However, recent measurements [C.O. Davis,

unpublished] and Monte Carlo simulations for "case 1" waters [Morel and Gentili

1993] show that Q increases with wavelength, which is an inverse trend compared to

b_{bp} [Carder et al. 1991].

Using the single and quasi-single scattering approximations of Gordon [1994],

Lee et al. [1992, 1994a] found that for a wide variety of waters, Eq. 30 can be

expanded as

$$R_{rs}^{w}(0^-) \approx \frac{G}{a}\left[\frac{b_{bw}}{Q_m} + X\left(\frac{400}{\lambda}\right)^Y\right], \tag{31}$$

where Q_m is the Q factor for molecular scattering. Q_m can be estimated based on the

molecular VSF shape and the illumination geometry [Lee et al. 1992, 1994a].

Eq. 31 can be seen as a simplification of Eq. 24 for wide situations, with the

first term in the bracket of the right side representing the backscattered photons due to

molecular scattering, and the second term representing the backscattered photons due

to particle scattering.

In Eq. 31, both G and Q_m increase with sun angle [Gordon 1989b, Kirk 1991,

Lee et al. 1992, 1994a], so we expect that $R_{rs}(0^-)$ is less sensitive to the solar zenith

angle than $R(0^-)$. To simplify matters, we can take average values of G and Q_m and

allow any errors due to these simplifications to be embedded into the empirical terms

X and Y. G is about 0.32 according to Gordon et al. [1975], Jerome et al. [1988], and

Kirk [1991]. Q_m is about 3.4 [Lee et al. 1992, 1994a]. Thus, our equation becomes

$$R_{rs}^w(0^-,\lambda) \approx \frac{0.32}{a(\lambda)}\left[\frac{b_{bw}(\lambda)}{3.4} + X\left(\frac{400}{\lambda}\right)^Y\right].$$ (32)

Variations due to VSF, solar zenith angle, and view angle are now all embedded in the two parameters X and Y. Since there is a different wavelength exponent between the scattering coefficients of molecules versus that of particles, errors generated by using average G and Q_m values can not be completely compensated by the adjustment of the X and Y values. However, since $b_{bw}(\lambda)$ is relatively small, the compensation can be close to 100% for turbid waters and larger than 90% for clear waters.

Comparing Eqs. 29 and 32, it is found that if b_{bp} of b_b in Eq. 29 is expressed as $X'(400/\lambda)^{rb}$, then $X' \approx 3.42X + 0.0043b_{bw}(400)$. Since $0.0043b_{bw}(400)$ is very small, Eq. 29 and Eq. 32 are mathematically almost the same. Thus, with two parameters to address b_{bp} and/or Q, R_{rs}^w can be expressed by either Eq. 29 or Eq. 32. Using Eq. 32, $3.42X$ can be used as an estimate of $b_{bp}(400)$. Also, since remote sensing measures part of the backscattered photons, Eq. 32 is more consistent with Eq. 24, the absolute solution.

Actually, Eq. 29 could be derived from Eq. 24 if $c + k_L - \epsilon\, b_f = 3a$, and $\overline{\beta}_b = b_b/3.55$. However, both assumptions depend on the radiance distribution in the downwelling $(L_d(\Theta,\varphi))$ and upwelling $(L_u(\Theta,\varphi))$ hemispheres. If the downwelling light is totally diffused, then $\overline{\beta}_b = b_b/\pi$. But this light field is not totally diffused in general, so $\overline{\beta}_b \neq b_b/\pi$.

Eq. 32 pertains to optically deep water. In optically shallow water, scattering media and the backscattering signals are reduced due to the shorter water column. To

model these optically shallow waters, we consider that the subsurface E_u^w consists of two parts coming from two layers: one from the layer above the bottom, and one from the layer "below" the bottom. Then the subsurface E_u^w coming from the upper layer only can be obtained by reducing the optically deep expression by an amount equivalent to the contribution of the missing water column below H. Thus for shallow waters with depth H and a totally absorbing bottom, with $t = 0.98$, and $n_w = 1.34$, R_{rs}^w is approximated by

$$R_{rs}^w \approx \frac{0.17}{a}\left[\frac{b_{bw}}{3.4} + X\left(\frac{400}{\lambda}\right)^Y\right]\left[1 - e^{-\int_0^H (K_d + K_u) dz}\right],\tag{33}$$

with z positive downward from the surface.

If we define the quasi-diffuse attenuation coefficient as $\kappa = a + b_b$, then $K_d \approx D_d \kappa$ and $K_u \approx D_u \kappa$ [Gordon 1989a]. Since $D_u/D_d \approx 2$ [Gordon et al. 1975], we can rewrite Eq. 33 as

$$R_{rs}^w \approx \frac{0.17}{a}\left[\frac{b_{bw}}{3.4} + X\left(\frac{400}{\lambda}\right)^Y\right]\left[1 - e^{-3(D_d)\kappa H}\right],\tag{34}$$

where $\{D_d\}$ is the vertically averaged downwelling distribution function and $\{D_d\}$ is approximate by $1.08 D_d(0)$ [Gordon 1989a, Lee et al. 1994a].

2.3 Remote-sensing Reflectance of Bottom Reflectance, R_{rs}^b

Assuming that the bottom is an extended Lambertian reflector with bottom

albedo ρ, then for a nadir-viewing sensor, R_{rs}^{b} can be approximated by [Lee et al. 1992, 1994a]

$$R_{rs}^{b} \approx \frac{t^2}{n_w^2} \frac{\rho}{\pi} e^{-((D_u)\kappa + k)H}, \tag{35}$$

where k is the effective attenuation coefficient for the radiance from an extended Lambertian source. How k relates to the quasi-diffuse attenuation coefficient κ is not well understood. Heuristically, it should be a value between c and κ. It was found that k is from 1.36κ to 1.62κ for κH in the range of 0.5 - 2.0 based on the Monte Carlo simulations [Gordon 1989a] for an extended totally diffuse light source (detailed in Appendix 2). As an average in this work, $k = 1.5\kappa$ as is used by Marshall and Smith [1990]. Then Eq. 35 becomes [Lee et al. 1992, Lee et al. 1994a]

$$R_{rs}^{b} \approx 0.17\rho e^{-((D_u)+1.5)\kappa H}. \tag{36}$$

This value depends not only on the optical properties of the water body, but also on water depth and the bottom albedo [Gordon and Brown 1974]. In the modeling work, the water depth was based on the Provisional Chart for the Gulf Coast (#1003), and the bottom albedo was based on measurements of bottom samples from the region with near-shore values of $\rho = 0.1$ to 0.2 (used for station TA01), and offshore values of $\rho = 0.4$ to 0.5 (used for stations TA02 and TA03). Figure 10 shows examples of those albedo spectra. The quasi-diffuse attenuation coefficient κ is assumed to be equal to total absorption a as $b_b << a$ for most of the world ocean [Morel and Prieur 1977].
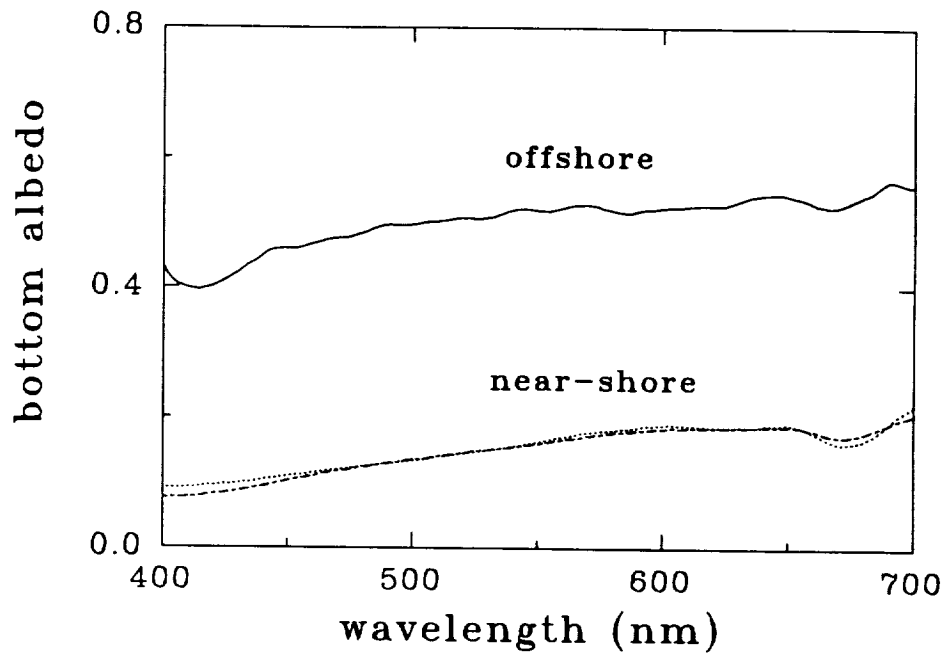
Figure 10. Examples of Bottom Albedo Spectra.

For sensors not viewing the nadir, k in Eq. 35 needs to be adjusted to

$k/\cos(\Theta_w)$. In our experiments, Θ_w is generally within $20°$, i.e. $0.93 \leq \cos(\Theta_w) \leq$

1.0, so $k/\cos(\Theta_w) \approx 1.5\kappa$ could still be used.

2.4 Remote-sensing Reflectance of Gelbstoff Fluorescence, $R_{rs}{}^f$ and Water Raman Scattering, $R_{rs}{}^R$

In general, these terms are due to inelastic scattering. By considering β_{ie} (the

volume scattering function for inelastic scattering) isotropic, remote-sensing

reflectance due to gelbstoff fluorescence and water Raman scattering can be

approximated as [Lee et al. 1992, 1994a] (detailed in Appendix 3)

$$R_{rs}^{f}(\lambda) \approx 0.072 \int_{\lambda_x} \eta(\lambda_x) \frac{\lambda_x}{\lambda} \frac{a_g(\lambda_x) E_d(0^-,\lambda_x)}{[2a(\lambda)+a(\lambda_x)]E_d(0^-,\lambda)} \frac{e^{-s\left[\ln\frac{\lambda-\lambda_f}{\sigma}\right]^2}}{A} d\lambda_x, \qquad (37)$$

and

$$R_{rs}^{R}(\lambda) \approx 0.072 \frac{b^{R}(\lambda_x)E_d(0^-,\lambda_x)}{[2a(\lambda)+a(\lambda_x)]E_d(0^-,\lambda)}. \qquad (38)$$

So, combining Eqs. 34, 36, 37 and 38, after calculating R_{rs}^{R}, R_{rs}^{f} and R_{rs}^{b}, only

X and Y remain as unknowns. By matching the modeled R_{rs}^{w} and the residual of R_{rs} -

R_{rs}^{R} - R_{rs}^{f} - R_{rs}^{b}, X and Y can be derived using the predictor-corrector approach to

modeling as in Carder and Steward [1985].

CHAPTER 3

DATA AND METHODS

3.1 Introduction

From 1989 to 1993, measurements of optical properties for a variety of waters were taken, including sites in the North Atlantic, Monterey Bay, the West Florida Shelf, the Gulf of Mexico and the mouth of the Mississippi River. In these waters [chl a] ranged from 0.07 - 50 mg/m^3, and $a_g(440)$ ranged from 0.005 - 0.5 m^{-1}. Table 1 summarizes the cruise information, while Figure 2a shows the locations of data collection. For each station, hyperspectral R_{rs} and particle and pigment absorption coefficients (a_p and a_ϕ) of surface water samples were measured. For the 1993 Gulf of Mexico stations, a long-path (50 cm or 100 cm) [Peacock et al. 1994] spectrophotometer was used to measure a_g.

In-water optical properties (K_d and $R_{rs}(0^-)$) were calculated based on the profiles of downwelling irradiance and upwelling radiance, which were measured by Dr. J. L. Mueller (San Diego State University) or Dr. C. O. Davis (Jet Prop. Lab) using a Biospherical MER sensor (model 1048A).

3.2 Remote-sensing Reflectance, R_{rs}

Hyperspectral R_{rs} was measured by the method developed by Carder and Steward [1985], using a Spectron Engineering spectroradiometer (Spectron Model SE-590) with 253 spectral channels covering the wavelength range from 370 - 1100 nm. With this instrument, the upwelling radiance above the surface $(L_u(0^+, \Theta_a, \varphi))$ was directly measured, with $\Theta_a \leq 30°$ and φ about $90°$ from the solar plane (see Figure 5 for the geometry). The downwelling sky radiance (L_{sky}) was also directly measured in the same plane as $L_u(0^+)$ but from a direction reciprocal to $L_u(0^+)$. Downwelling irradiance was derived by measuring the radiance (L_G) reflected from a standard diffuse reflector (Spectralon). With these measurements, R_{rs} was derived through

$$R_{rs} = \frac{L_u(0^+) - r L_{sky}}{\pi L_G} R_G - \Delta \ . \tag{39}$$

The upwelling radiance is

$$L_u(0^+) = (R_{rs} + \Delta) \frac{\pi L_G}{R_G} + r L_{sky} \ , \tag{40}$$

where r is the Fresnel reflectance of the water surface, and R_G is the reflectance of the diffuse reflector. Figure 11 shows the values of sea water r for the horizontal and vertical electric components as well as for the unpolarized light. $r \approx 0.018$ (a $20°$ view angle) is usually used when there is a vertical polarizer in front of the sensor, and Δ is the offset for sun glint due to waves and surface foam, which is derived by forcing $R_{rs}(750) = 0$ (usually for offshore waters).
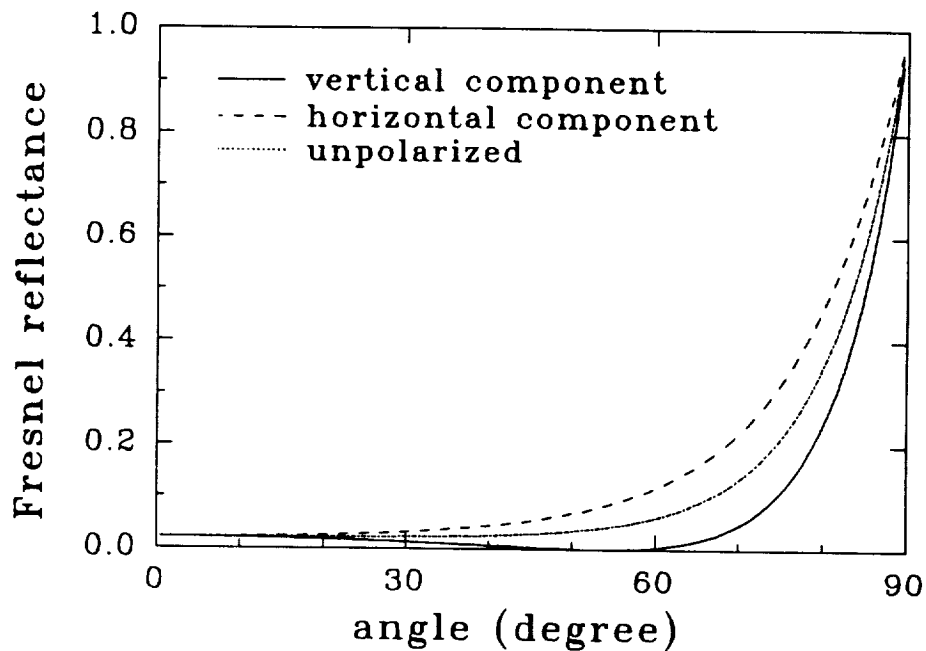
Figure 11. Fresnel Reflectance of Sea Water (n_w = 1.34).

3.3 Absorption Coefficient of Particles and Pigments, a_p and a_ϕ

The method described by Mitchell and Kiefer [1988] was used to measure a_p,

and the method developed by Kishino et al. [1985] and modified by Roesler et al.

[1989] was used to measure a_d and to derive a_ϕ. Briefly, water samples were filtered

onto Whatman GF/F filter pads immediately after collection. Another pad wetted with

filtered sea water served as a blank. The transmission spectra from 380 nm to 800 nm

of these pads (T_p and T_b) were measured by the Spectron. The optical geometry was

designed to illuminate the pad with diffuse light from a Lambertian diffuser added

between the light source and the filter pad. This geometry is very similar to that of

Table 2. Recent Results for "Beta Factor" of GF/F Filter Pad.

Authors	"beta factor" expressions
Nelson and Robertson, 1993	$\beta_{pad} = 1.0 + 0.46\ OD_p^{-0.70}$
Cleveland and Weidemann, 1993	$\beta_{pad} = (0.378 + 0.523\ OD_p)^{-1}$
Bricaud and Stramski, 1990	$\beta_{pad} = 1.63\ OD_p^{-0.22}$
Mitchell, 1990	$\beta_{pad} = (0.392 + 0.655\ OD_p)^{-1}$

Bricaud and Stramski [1990], who illuminated a pad in front of a diffusing window

which was adjacent to an end-on photomultiplier tube. The volume filtered was about

500 - 1500 ml (depending on the water clarity).

Using the measured transmission spectra, the optical density of the sample is

$$OD_p = \log\frac{T_b}{T_p}\ , \tag{41}$$

and the absorption coefficient of the sample is

$$a_p = 2.3\frac{OD_p}{B\beta_{pad}}\ , \tag{42}$$

where B is the ratio of the volume filtered to the effective surface area of sample on

the pad. β_{pad} is the so called "beta factor" [Mitchell and Kiefer 1988], introduced to

describe the optical-path-length elongation due to the filter pad. Table 2 and Figure 12

provide recent results of β_{pad} for GF/F filter pad. Notice the significant differences of

β_{pad} when OD_p is around or less than 0.1. In our calculation of a_p, β_{pad} from Bricaud

and Stramski [1990] (their Eq. 2) was used. In the calculation of the absorption
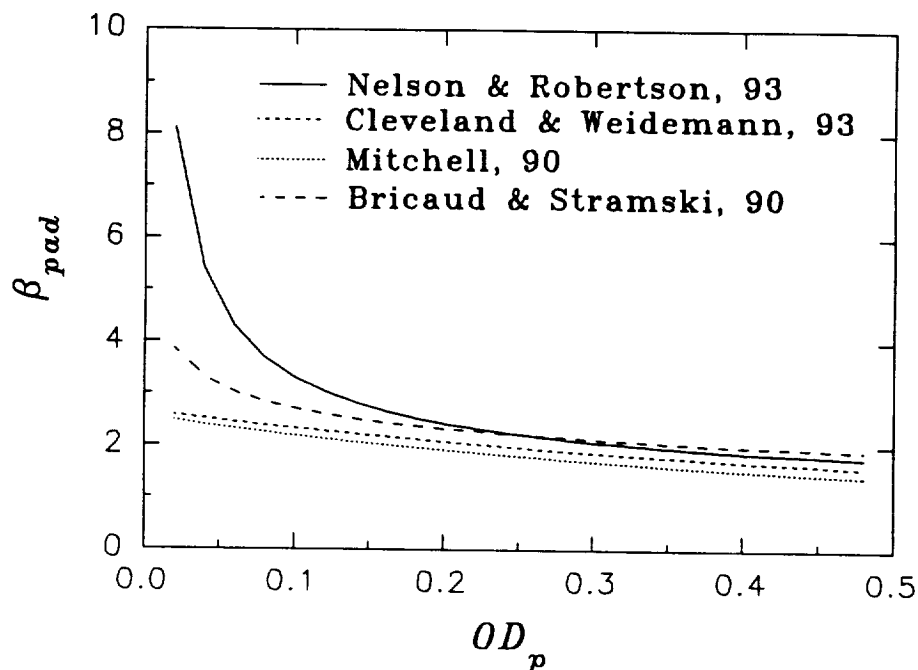
Figure 12. Recent Results for "Beta Factor" of GF/F Filter Pad.

coefficient, large-particle scattering was corrected by assuming $a_p(780) = 0$ from the a_p curve.

After this measurement, the sample pad was soaked in hot methanol [Kishino et al. 1985, Roesler et al. 1989] for about 15 minutes to remove pigments, and its optical density was again determined via Eq. 41, and the detrital absorption coefficient a_d was obtained by Eq. 42.

The difference between the particle and detrital absorption coefficients provided the absorption coefficient of phytoplankton pigments, a_ϕ:

$$a_\phi = a_p - a_d \cdot \qquad (43)$$

3.4 Absorption Coefficient of Gelbstoff, a_g

For stations before 1993, the absorption coefficient of gelbstoff (a_g) was not explicitly measured for visible wavelengths. However, from Eq. 27, the total absorption coefficient could be derived from $K_d(av)$, and a_w and a_p were available, so a_g could be estimated from $K_d(av)$ values, using the expression $a_g \approx K_d(av)/(1.08D_d(0)) - a_w - a_p$, as $b_b << a$. At the 1993 GOMEX and COLOR stations, a_g of water samples were measured using 50-cm or 100-cm path-length instruments, respectively, after filtering the sample through 0.2 μm pore-diameter Gelman Supor-200 filters [Peacock et al. 1994].

3.5 Measurements of In-water Optical Properties, K_d and $R_{rs}(0^-)$

A Biospherical Instrument MER (model 1048A) was used to determine the vertical structure of the water column. The depth profiles of downwelling irradiance ($E_d(z)$) and upwelling radiance ($L_u(z)$) were determined for each cast.

With these measurements, $K_d(av)$ and sub-surface downwelling irradiance ($E_d(0^-)$) and upwelling radiance ($L_u(0^-)$) were derived. The process is similar to that of Smith and Baker [1981]. Briefly,

$$E_d(z) = E_d(0^-)e^{-K_d(av)z} , \tag{44}$$

then,

$$\ln[E_d(z)] = \ln[E_d(0^-)] - K_d(av)z \ . \tag{45}$$

Due to surface-wave-focusing and ship shadow effects [Gordon 1985], the measured $E_d(z)$ and z include errors associated in the field, and we cannot simply use values from two depths to derive $K_d(av)$ and $E_d(0^-)$. In order to correct these errors, linear regression between $\ln[E_d(z)]$ and z were performed for the surface layer. The regression results gave $K_d(av)$ and $\ln[E_d(0^-)]$. The same process was applied to $L_u(z)$ to get $L_u(0^-)$.

CHAPTER 4

RESULTS OF R_{rs} MODELING

4.1 Validation of R_{rs} Model

In previous studies [Carder and Steward 1985, Peacock et al. 1990, Lee et al. 1992, Lee et al. 1994a], qualifying words such as "excellent," "very good" or "good" were used to describe how well the modeled curve fit the measured curve, and they were usually justified visually. There was no quantitative indication regarding the difference between the measured and modeled curves. Here, a modified average percentage difference $(a.p.d.)$ is used to quantify and validate the model results of R_{rs}. It is defined as

$$a.p.d. = \frac{\left[AVG_{400}^{660}\left(R_{rs}^{mea}-R_{rs}^{mod}\right)^2 + AVG_{750}^{830}\left(R_{rs}^{mea}-R_{rs}^{mod}\right)^2\right]^{0.5}}{AVG_{400}^{660}(R_{rs}^{mea}) + AVG_{750}^{830}(R_{rs}^{mea})}, \tag{46}$$

where $AVG_{\lambda_1}^{\lambda_2}$ means the average value in the wavelength range from λ_1 to λ_2.

The cut-off between 660 and 750 nm is because there is no term included to model the chlorophyll a fluorescence in the measured signal. The 750 - 830 nm band is important for turbid waters.

In the forward process, a_g was measured or estimated, a_p was measured, H for shallow waters came from published charts, and the predictor-corrector method

Table 3. Station Chosen for the R_{rs} Model Demonstration.

Station	Latitude	Longitude	Time/Date	Bottom depth	Mod. depth
TA01	27°27' N	82°55' W	+10.5/3-4-90	14m	13.7m
TA02	27°20' N	83°03' W	+13.0/3-4-90	25m	25m
TA03	27°12' N	83°11' W	+14.9/3-4-90	35m	36m
GO08	28°48' N	91°30' W	*08.5/4-12-93	-	-
GO10	28°15' N	91°30' W	*14.0/4-12-93	-	-
GO27	29°32' N	85°47' W	*09.2/4-19-93	-	-
CO12	28°52' N	89°33' W	++10.8/6-5-93	-	-
CO14	28°48' N	90°02' W	++16.1/6-5-93	-	-
CO19	27°34' N	83°20' W	++09.5/6-8-93	33m	35m

Note: " - " indicates that the water is optically deep. +: East standard time,
*: Central daylight time, ++: East daylight time.

[Carder and Steward 1985] was used to obtain the values of X and Y. In this process, it was sometimes necessary to apply a factor f to the measured a_p, such that the absorption coefficient of particles used in the model is $f * a_p$. The purpose of this f is to correct for possible errors due to patchiness, and/or the "beta factor" (see Figure 12). It is necessary to keep in mind that the process here was focused on testing the expressions developed in Chapter 2 using the measured components, so only minor adjustments were applied to the measured components before a small ($\leq$ 0.05) $a.p.d.$ was obtained. Most of the parameter derivation was concentrated on X and Y (and p for shallow waters), and the parameter f was not varied much (usually 0.9 to 1.1) from 1.0 in reducing the $a.p.d.$.

For the calculation of $R_{rs}{}^f$, η, s, λ_f and σ came from the measurements of Hawes

et al. [1992] and Hawes [1992], while $b^R(\lambda_o)$ for $R_{rs}{}^R$ came from Collins et al. [1984].

4.2 Model Results and Discussion

Measured R_{rs} curves for 9 stations were selected to demonstrate the model

developed in Chapter 2. These 9 stations covered a wide range of water types: 1) the

West Florida Shelf with shallow, gelbstoff-rich coastal waters; and 2) Gulf of Mexico

waters with phytoplankton blooms in the Mississippi River plume ($S > 17\permil$).

Table 3 provides the station locations as well as the measured and modeled water

depths for the shallow stations. Figure 2b shows the locations of these stations in the

Gulf of Mexico. As examples, Figures 13a - 13d show the detailed model components

for R_{rs}, and Figure 14 shows the results for the chosen stations. Table 4 lists the

model parameters X, Y, $a_g(440)$, and $a_p(440)$ with $a.p.d.$ and the measured values of

$a_p(440)$ and [chl a] for each station. Table 5 details the fractional contributions that

$R_{rs}{}^w$, $R_{rs}{}^R$, $R_{rs}{}^f$ and $R_{rs}{}^b$ make to the measured R_{rs} at 440 nm and 550 nm.

It can be seen from Figures 13a - 13d that excellent fits were achieved between

the measured and modeled R_{rs} curves for all of the selected stations except for the

spectral region around 685 nm where chlorophyll a fluorescence is present in the field

data. This excellence can also be seen from the $a.p.d.$ values (Table 4) for each

station with the average $a.p.d.$ being 3.1%, which is within the measurement
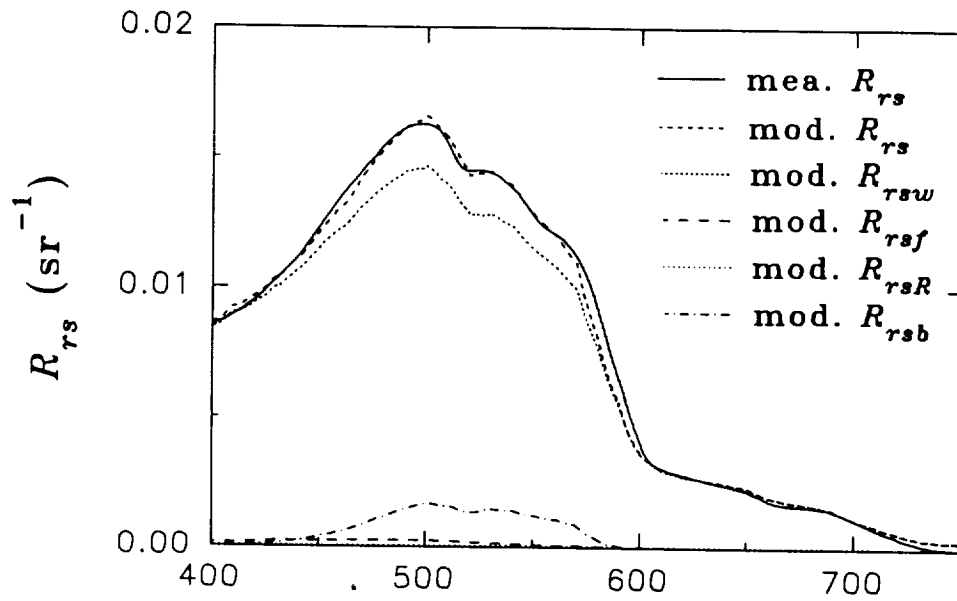
Figure 13a. Detailed R_{rs} Model for Station TA01.
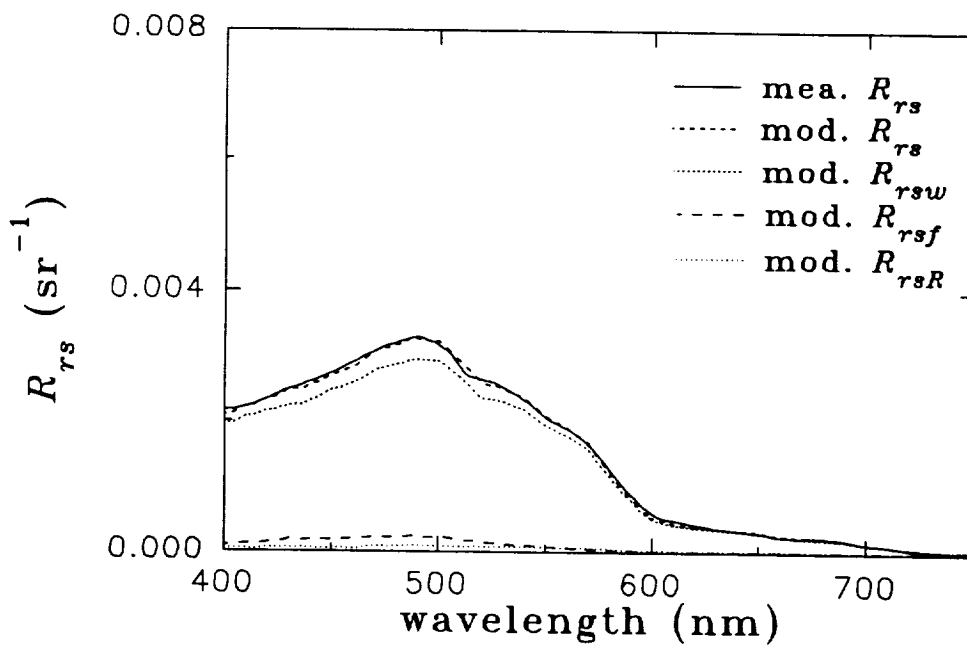
Figure 13b. Detailed R_{rs} Model for Station GO27.
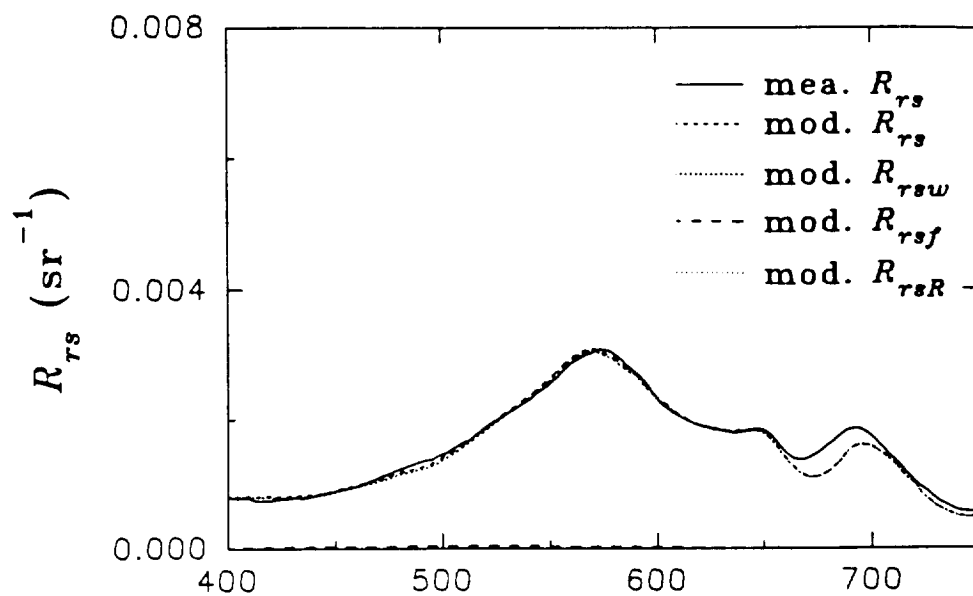
Figure 13c. Detailed R_{rs} Model for Station CO14.
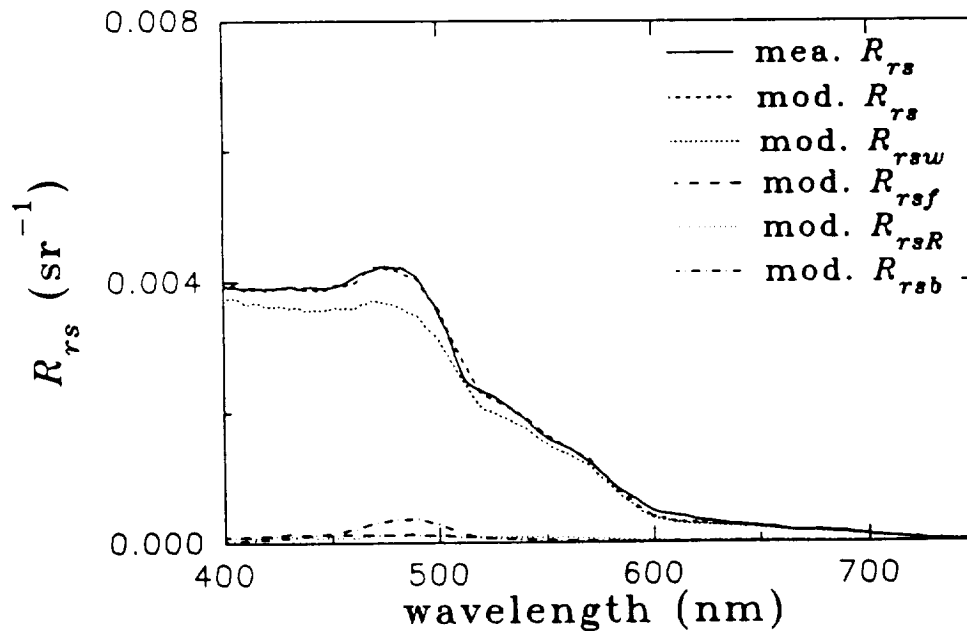
Figure 13d. Detailed R_{rs} Model for Station CO19.

accuracy. For such a small percentage difference, we can reasonably say the model developed here works very well for these waters.

For the stations chosen, the a_p that was required by the model was in general within 10% of the measured a_p except near the Mississippi River at station CO12 (20%), with very high [chl a] (38.6 mg/m3). The average difference between the measured and required a_p is 8.9% (9 stations) (7.5% when station CO12 is excluded). The maximum 15% or 20% difference can perhaps be explained by the water patchiness and/or the accuracy involved in the method of a_p measurement due to the "beta factor" which varies significantly between species and researchers [Bricaud and Stramski 1990, Mitchell 1990, Yentsch and Phinny 1992, Cleveland and Weidemann 1993, Nelson and Robertson 1993] (see Table 2 and Figure 12). This effect may be especially important for station CO12 which was near the Mississippi River mouth where the heavy load of sediments and minerals might cause additional uncertainty in the optical path length elongation. Also, the influence of horizontal and vertical structure of the waters increases for mesotrophic - eutrophic waters, so patchiness can affect accuracies in the more hypertrophic waters. Finally, the low signal obtained for the upwelling radiance measurements at station CO12 made the R_{rs} calculation sensitive to corrections for reflected skylight.

It can be seen from Table 4 that the ratio of $a_g(440)$ to $a_p(440)$ among these waters was highly variable, with a range from 0.3 to 3.0, and the X value does not co-vary with the pigment concentration [chl a] for the waters studied. This illustrates that the model works well over a wide range of conditions, and also suggests why the

0.008

R_{rs} (sr^{-1})

0.004

0.000

400   500   600   700

1. TA02
2. TA03
3. CO19
4. GO10
5. GO27
6. GO08
7. CO14
8. CO12

wavelength (nm)
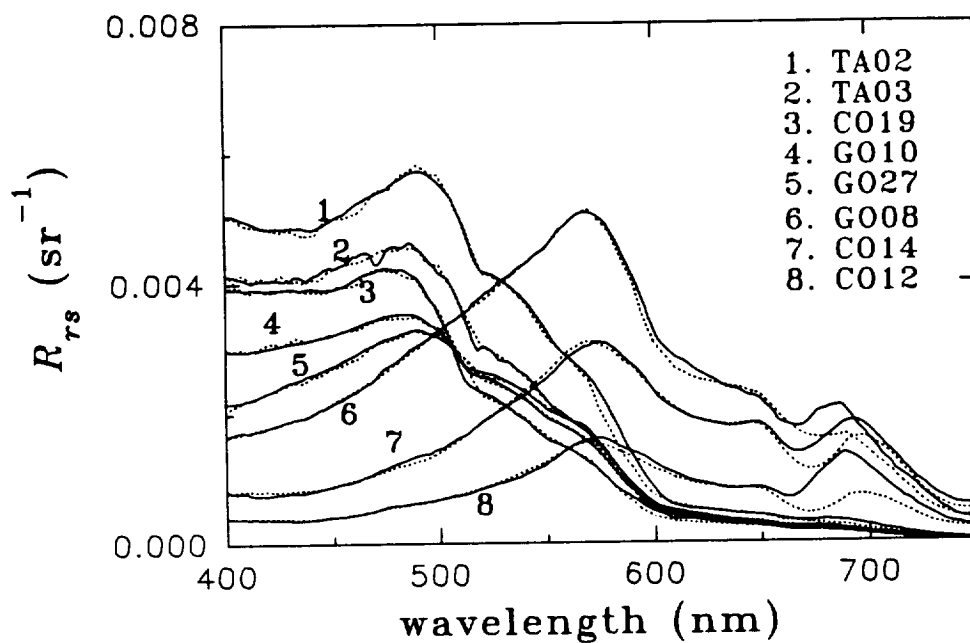
Figure 14. Measured vs. Modeled R_{rs} for the Selected Stations.
Solid: measured, dashed: modeled.

power-law pigment algorithm does not work well for coastal waters because of the lack of co-variation of all optical components with [chl a]. The highest X value, 0.0087 m^{-1}sr^{-1}, was at the shallow, mesotrophic station TA01, suggesting a large scattering effect due to detritus and suspended sediments. Brisk northwesterly winds suspended sediments in the shoal regions to the east and north of the station, and they likely were transported by the ebb tidal currents from Tampa Bay to the study site [Carder et al. 1993].

The Y values were within the range from 0 to 2.4 for the waters reported here, which might be interpreted as being partially due to b_{bp}. For b_{bp}, as mentioned in section 1.4.2.2, the wavelength exponent (η_b) is in the expected range 0 - 3.0 for a

Table 4. Model Parameters for Stations in Table 3.

Station	X	Y	a_{gl}	a_{pl}	a.p.d.	a_{pl}^{mea}	[chl a]
TA01	.0087	1.2	.082	.041	.037	.045	1.05
TA02	.0022	2.4	.042	.033	.025	.035	.61
TA03	.0012	2.3	.034	.027	.029	.026	.70
GO08	.0065	.24	.31	.28	.033	.295	5.27
GO10	.0010	1.8	.059	.023	.023	.021	.12
GO27	.0014	1.9	.078	.029	.021	.034	.20
CO12	.0030	0	.42	1.34	.044	1.12	38.58
CO14	.0068	0	.38	1.21	.031	1.16	20.26
CO19	.0007	2.0	.023	.021	.037	.023	.22

Note: $a_{gl} = a_g(440)$, $a_{pl} = a_p(440)$.

range of particles (e.g. river sample [Whitlock et al. 1981], bacteria [Morel and Ahn 1990], phytoplankton cells [Bricaud and Morel 1986], and coccoliths [Gordon et al. 1988]). For $Y = 2.4$, if the exponent for Q is 1.0, then $\eta_b = 1.4$, which is within the 0 - 3.0 range reported elsewhere, also is within the range of 0 - 2 as used by Sathyendranath et al. [1989a]. Generally Y values were found to be low for turbid water, and high for clear water. The value 2.4 for stations TA02 and TA03 of the West Florida Shelf seems a little bit high for those waters. This might be due to errors in a_g, as a_g was derived from K_d for those stations. For the world ocean, the range of Y needs further study.

At the optically shallow stations (TA01, TA02, TA03, and CO19), the model-required depths were within about 10% of the chart depths without consideration of

any tidal influence (typically <0.5 m). This demonstrates that Eq. 36 works well for

shallow waters, and it indicates a potential to use this model to survey (e.g. by

aircraft overflights) dramatic changes in shelf bathymetry that can occur as a result of

major storms. For station CO19, an albedo value of about 0.1 was used in the model,

suggesting the bottom might contain more heavy minerals or grass at that site. Direct

bottom albedo measurements are lacking at individual stations and are needed for a

wide variety of bottom types.

For stations TA01, TA02, TA03, GO08, CO12 and CO14, the general

agreement between the modeled and measured R_{rs} values is very good ($\sim 3.5\%$

$a.p.d.$), with small differences around 580 nm, where the measured R_{rs} > modeled

R_{rs}. Other than modeling error, there are at least three possible reasons for this: a)

bottom albedo uncertainty, b) phycoerythrin fluorescence [Yentsch and Yentsch 1979,

Yentsch and Phinney 1985], and c) water absorption coefficient uncertainty [Smith

and Baker 1981, Tam and Patel 1979].

A spectrally constant bottom albedo was used for the shallow stations. Soil

reflectance [Tucker and Miller 1977] and earlier measurements of bottom albedo

(Figure 10) did display some spectral dependence. The amount of change spectral

albedo could induce would not provide the sharp spectral increase and then decrease

with wavelength in R_{rs} required for the measured and modeled R_{rs} curves to converge,

however. There also was no bottom contribution to R_{rs} at GO08, CO12 and CO14.

More realistic explanations include the lack of a term in the model for phycoerythrin

fluorescence, the differences between the water absorption coefficients in this

Table 5. Optical Component Contributions to R_{rs} of Stations in Table 3.

Station	R_{rs}^{w}/R_{rs}		R_{rs}^{fR}/R_{rs}		R_{rs}^{b}/R_{rs}		$R_{rs}(440)/R_{rs}(550)$	
	440	550	440	550	440	550	mea. R_{rs}	corr. R_{rs}
TA01	.95	.92	.02	.01	.02	.10	.87	.91
TA02	.91	.82	.05	.06	.05	.11	1.48	1.77
TA03	.87	.83	.10	.12	.02	.04	1.87	1.96
GO08	.97	1.00	.03	.02	-	-	.49	.48
GO10	.92	.94	.08	.07	-	-	1.64	1.61
GO27	.91	.96	.08	.07	-	-	1.34	1.26
CO12	.92	1.03	.09	.03	-	-	.31	.28
CO14	.99	1.02	.03	.01	-	-	.32	.31
CO19	.92	.96	.06	.07	.01	.01	2.46	2.37

Note: $R_{rs}^{fR} = R_{rs}^{f} + R_{rs}^{R}$; corr. R_{rs} = mea. $R_{rs} - R_{rs}^{fR} - R_{rs}^{b}$.

spectral region as reported by Smith and Baker [1981] and by Tam and Patel [1979], and the accuracy of the "beta factor" for low absorbing portions of $a_\phi(\lambda)$ for detritus -rich stations. Further study is required in order to resolve this issue. The differences between the measured and modeled R_{rs} curves around 685 nm, on the other hand, are expected due to the fact that no term is included in the model to describe the chlorophyll a fluorescence [Carder and Steward 1985].

4.3 Contributions by R_{rs}^{f} and R_{rs}^{R}

Model results at station TA03 suggest relatively higher gelbstoff fluorescence and water Raman scattering influences, since a higher η (1.5%) [Hawes et al. 1992]

was used. This value is ~3 times greater than the value suggested by Spitzer and Dirks [1985] for terrigenous gelbstoff. If we exclude this station, 90% or more of the water-leaving radiance is accounted for by the sum of the elastic scattering from molecules, particles and the bottom, which leaves about 10% or less of the measured R_{rs} for gelbstoff fluorescence and water Raman scattering. This is consistent with the reports of Marshall and Smith [1990] and Stavn [1990], as water Raman scattering makes more of a contribution when the water is clear.

It is interesting that the ratio $R_{rs}(440)/R_{rs}(550)$ did not vary widely due to inelastic scattering (see Table 5). Among stations without bottom influence, differences in the ratio were within ~10%, which suggests the spectral radiance ratio algorithm is effective for most deep waters without consideration of gelbstoff fluorescence and water Raman scattering. However, it is obvious that as the bottom influence increases, the usefulness of the power-law algorithm decreases. Also, the power-law algorithm can not distinguish between the absorption of gelbstoff and that of pigments. Note that $R_{rs}^w(490)/R_{rs}(490)$ values as low as 0.77 were determined (not explicitly shown), suggesting that great care must be taken when interpreting remote-sensing curves for the intermediate wavelengths at shallow coastal stations.

CHAPTER 5

CONCLUSIONS OF PART A

5.1 Contributions to the water-leaving radiance spectra for a variety of waters can be attributed to elastic scattering by water molecules, suspended particles, and bottom reflectance, and to inelastic scattering by water Raman scattering and gelbstoff fluorescence. Inelastic scattering by pigments was not considered. For optically deep water, remote-sensing reflectance of the water column part (elastic scattering only), $R_{rs}{}^w(\lambda)$, can be mathematically simulated as follows

$$R_{rs}^w(\lambda) \approx \frac{0.17}{a_w(\lambda)+a_g(\lambda)+a_p(\lambda)}\left[\frac{b_{bw}(\lambda)}{3.4}+X\left(\frac{400}{\lambda}\right)^Y\right], \tag{47}$$

where $b_{bw}(\lambda)$ is known, X and Y are spectral constants, and Y was less than 2.4 for the waters considered. For optically shallow waters, the expression for bottom-reflectance contribution,

$$R_{rs}^b \approx 0.17\rho e^{-((D_d)+1.5)aH}, \tag{48}$$

works well for the shallow waters considered. Together, the water-column term and the bottom-reflectance term accounted for about 90% or more of the total remote-sensing reflectance.

5.2   Close agreement between modeled and measured R_{rs} was achieved for all

selected stations when all of the scattering mechanisms mentioned (both elastic and

inelastic) were included. The average a.p.d. is 3.1%. The ratio $a_g(440)/a_p(440)$

ranged from ~0.3 to ~3.0, indicating the broad usefulness of the model. For

contributions other than from the water column, as much as 23% of $R_{rs}(490)$ is

attributable to water Raman scattering, gelbstoff fluorescence, and bottom reflectance

for an optically shallow (25 m) station. For pigment algorithms based on the power

law of spectral radiance ratio, most "error" comes from reflected bottom radiance for

optically shallow coastal waters.

The a_p required by the model was generally within 10% of the measured a_p with

an average difference of 8.9% (9 stations) (7.5% when station CO12 is excluded).

This suggests a potential to remotely measure the pigment and gelbstoff absorption

coefficients, although derivation of [chl a] will depend upon knowledge of the

chlorophyll-specific absorption coefficient for a region.

5.3   The model-required bottom depths for the optically shallow waters are

within 10% of the chart depths, suggesting its possible use to remotely measure

bottom depth for the shelf waters.

5.4   The contribution of R_{rs}^{f} and R_{rs}^{R} were generally within 10% or less of the

total R_{rs}, covering the whole range from 400 nm to 600 nm. If these two terms were

omitted, this 10% or less difference can be roughly compensated by a small increase

in X value in the modeling. Also, R_{rs}^{f} and R_{rs}^{R} do not significantly affect the

$R_{rs}(440)/R_{rs}(550)$ ratio; thus, the power-law pigment algorithm can be used without the

correction of gelbstoff fluorescence and water Raman scattering with little error if the absorption and scattering properties co-vary with pigment concentration as happened for "case 1" waters. These imply that R_{rs}^{f} and R_{rs}^{R} could be omitted in the R_{rs} modeling to simplify the process.

PART B

THE INVERSE PROBLEM AND APPLICATIONS

CHAPTER 6

THE INVERSE PROBLEM

6.1 Introduction

As discussed previously, the ultimate goal of remote sensing is to derive the in-water constituents through remotely measured signals. Empirical and semi-analytical approaches have been discussed for derivation of pigment concentration [Clark 1981, Gordon and Morel 1983, Carder et al. 1991, Carder et al. 1994], and diffuse attenuation coefficient [Austin and Petzold 1981, Gordon and Morel 1983]. For the analytical approach, an inverse of the process described in Chapter 2, not much improvement has been achieved in the past studies. One of the difficulties is that a_p^* or a_ϕ^* change drastically from region to region, and it is not easy to accurately express these changes by a few parameters such as for a_g or a_d.

For R_{rs} of deep waters at N wavelengths (λ_1, λ_2, ..., λ_N), ignoring R_{rs}^f and R_{rs}^R as discussed in section 4.3, there are N equations

$$R_{rs}(\lambda_1) \approx \frac{0.17}{a_w(\lambda_1)+a_{dg}(\lambda_1)+a_\phi(\lambda_1)} \left[\frac{b_{bw}(\lambda_1)}{3.4}+X\left(\frac{400}{\lambda_1}\right)^Y\right],$$

$$\cdot$$
$$\cdot$$
$$\cdot$$

$$R_{rs}(\lambda_N) \approx \frac{0.17}{a_w(\lambda_N)+a_{dg}(\lambda_N)+a_\phi(\lambda_N)} \left[\frac{b_{bw}(\lambda_N)}{3.4}+X\left(\frac{400}{\lambda_N}\right)^Y\right],$$

(49)

in which a_{dg} can be expressed as [Roesler et al. 1989, Carder et al. 1991]

$$a_{dg}(\lambda) = a_{dg}(440)e^{-S_{dg}(\lambda-440)}.$$

(50)

There are at least N+4 unknowns for the N equations (N for $a_\phi(\lambda)$, 2 for $a_{dg}(\lambda)$

($a_{dg}(440)$ and S_{dg}) and 2 for particle scattering (X and Y)). If only R_{rs} is available,

there will be no certain solution for the above equations unless we dramatically reduce

the unknowns regarding $a_\phi(\lambda)$.

Bidigare et al. [1990] pointed out that a_ϕ can be re-constructed by knowing

concentrations and the specific absorption coefficients for each pigment, but these

cannot be known from remotely sensed data. Hoepffner and Sathyendranath [1991]

suggested that a_ϕ can be modeled by the sum of 11 Gaussian bands. For these 11

Gaussian bands, their center wavelengths and half band-widths would vary from

phytoplankton species to species. Even if the center wavelengths and half band-widths

can be fixed, we still need 11 parameters to simulate a_ϕ. Methods are also suggested

to use average specific absorption coefficient [Morel 1980, Sathyendranath and Platt

1988, Carder et al. 1991] or average absorption curves [Roesler and Perry 1994].

With these approaches, only one unknown (the pigment concentration or a scale

factor) is needed to model a_ϕ. Thus, if N is equal to or greater than 5, theoretically

the series of N equations could be solved and the unknowns related to the absorption

and scattering could be derived. But, due to the "package effect" and changing

environments, it is well known that the $a_\phi{}^*$ curves vary widely from sample to sample

[Morel 1980, Bricaud and Stramski 1990, Bidigare et al. 1990, Hoepffner and

Sathyendranath 1991, Carder et al. 1994]. No single shape or value for $a_\phi{}^*$ can be

used globally. So, for the inverse problem in remote sensing, simpler expressions

with adequate accuracy for a_ϕ would be very useful. The following section will

discuss the possible simple methods to simulate $a_\phi(\lambda)$ with the consideration of the

change of a_ϕ shape with water sample.

6.2 Simulation of $a_\phi(\lambda)$

Generally, there are two ways to simulate $a_\phi(\lambda)$: one is by the combination of

mathematical functions [Hoepffner and Sathyendranath 1991, Lee et al. 1994b], which

use a few parameters to simulate the whole spectrum; another is to empirically relate

a_ϕ of each wavelength to a specific value such as total pigment concentration [Morel

1980], or [chl a] [Carder et al. 1991] or a_ϕ at one wavelength [Carder et al. 1994,

Roesler and Perry 1994]. The first method is simple and has more power to adjust the

a_ϕ curve. This method, however, creates a smooth a_ϕ curve, and sacrifices the finesse

of the a_ϕ curve containing the pigment composition information when the number of

simulation parameters is limited. The second method shows the averaged finesse of

the a_ϕ curve, and has less potential to adjust the a_ϕ curve as generally it is controlled by one parameter.

6.2.1 Mathematical functions

By analyzing surface $a_\phi(\lambda)$ data collected from the Gulf of Mexico in April, 1993, which covered a [chl a] range from 0.07 to 40 mg/m^3, an expression for $a_\phi(\lambda)$ was suggested by Lee et al. [1994b], which is a combination of 3 simple functions involving 6 parameters. Among the 6 parameters, 2 parameters vary only slightly for different waters, and only 2 parameters have strong effects on the whole a_ϕ curve. There were a few a_ϕ curves from deep water samples which were greatly different from those of the surface samples, and could not be well simulated by the suggested simple expressions. But this is not important for remote sensing as 90% of the observed photons derive from the top attenuation depth $(1/K_d)$ [Gordon and McCluney 1975]. For species recognition, the methods of Bidigare [1990] and Hoepffner and Sathyendranath [1991] might be better.

For the wavelength range of 400 nm $\leq \lambda \leq$ 700 nm, the simple mathematical simulation for $a_\phi(\lambda)$ is:

$$400 \leq \lambda \leq 570, \quad a_\phi(\lambda) = a_{\phi 1}e^{-F\left(\ln\frac{\lambda-\lambda_1}{100}\right)^2}, \tag{51}$$

$$570 < \lambda < 656, \quad a_\phi(\lambda) = a_\phi(570) + \frac{a_\phi(656) - a_\phi(570)}{656 - 570}(\lambda - 570), \tag{52}$$

and

$$656 \leq \lambda \leq 700, \quad a_\phi(\lambda) = a_{\phi 2}e^{-\frac{(\lambda - \lambda_2)^2}{2\sigma_2^2}}. \tag{53}$$

The wavelength range for Eq. 51 was 400 - 590 nm in Lee et al. [1994b], but it is better for R_{rs} modeling if the range is adjusted to 400 - 570 nm.

With Eqs. 51 - 53, a_ϕ curves can be simulated. Figures 15a - 15d show examples of the simulated versus measured a_ϕ. For the a_ϕ samples, the normalized root-mean-square (rms) error is in the range of 5 - 20% with an average of 11%. Most of the variation occurred around 570 nm for clear water stations when the measured a_ϕ values were low.

In Eqs. 51 - 53, there are 6 parameters, $a_{\phi 1}$, F, λ_1, $a_{\phi 2}$, λ_2 and σ_2. Parameter F describes the width of the a_ϕ curve from 400 nm to ~ 560 nm, $100 + \lambda_1$ is the wavelength of the blue peak, λ_2 is the wavelength of the red peak and $2.355\sigma_2$ determines the half band-width around the red peak. For the samples studied [Lee et al. 1994b], F varies from 1.6 to 4.2, λ_1 varies from 338 - 342 nm with 80% at 340 nm, λ_2 varies from 672 to 675 nm with most at 674 nm, and $2.355\sigma_2$ ranged from 21 to 34 nm. $a_{\phi 1}$ varies from 0.01 to 0.83 m^{-1} while $a_{\phi 2}/a_{\phi 1}$ varies from 0.21 to 0.85. So, for the 6 parameters, λ_1 and λ_2 are almost fixed, and $a_{\phi 2}$ and σ_2 only affect a small
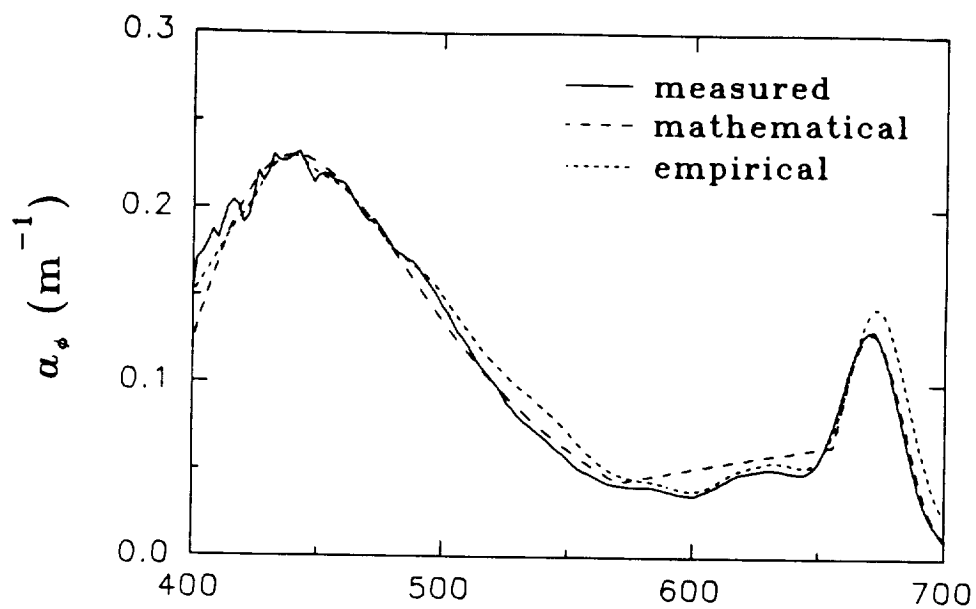
Figure 15a. Measured vs. Simulated a_ϕ for Station GO03.
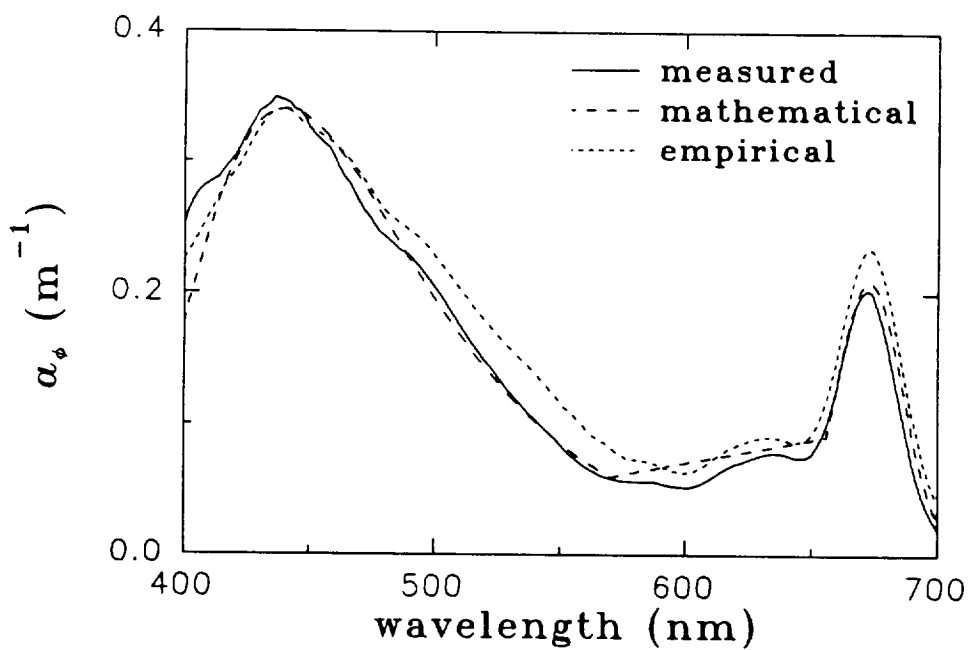
Figure 15b. Measured vs. Simulated a_ϕ for Station GO04.
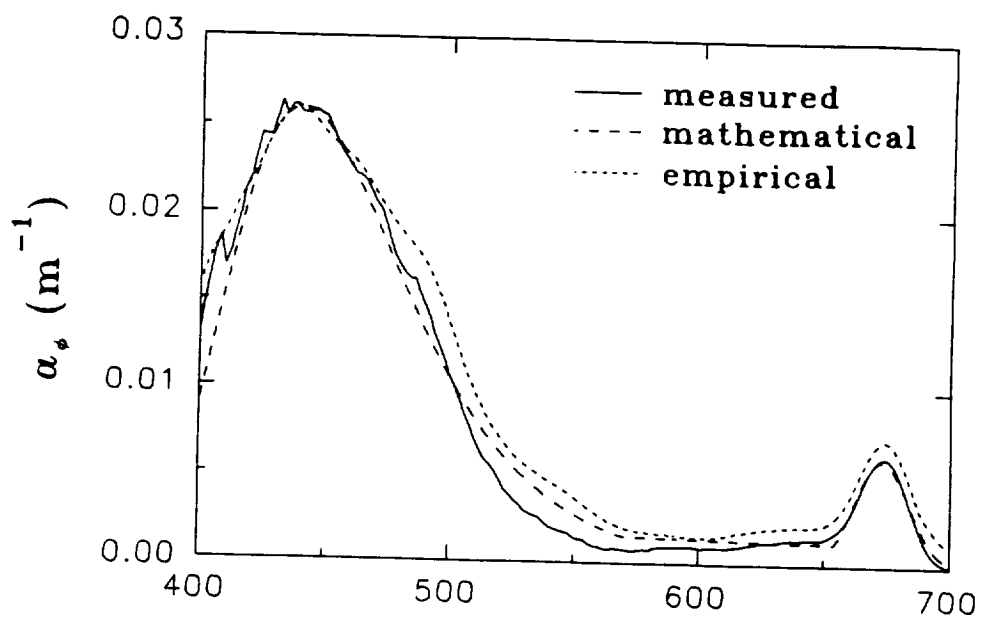
Figure 15c. Measured vs. Simulated a_ϕ for Station GO15.
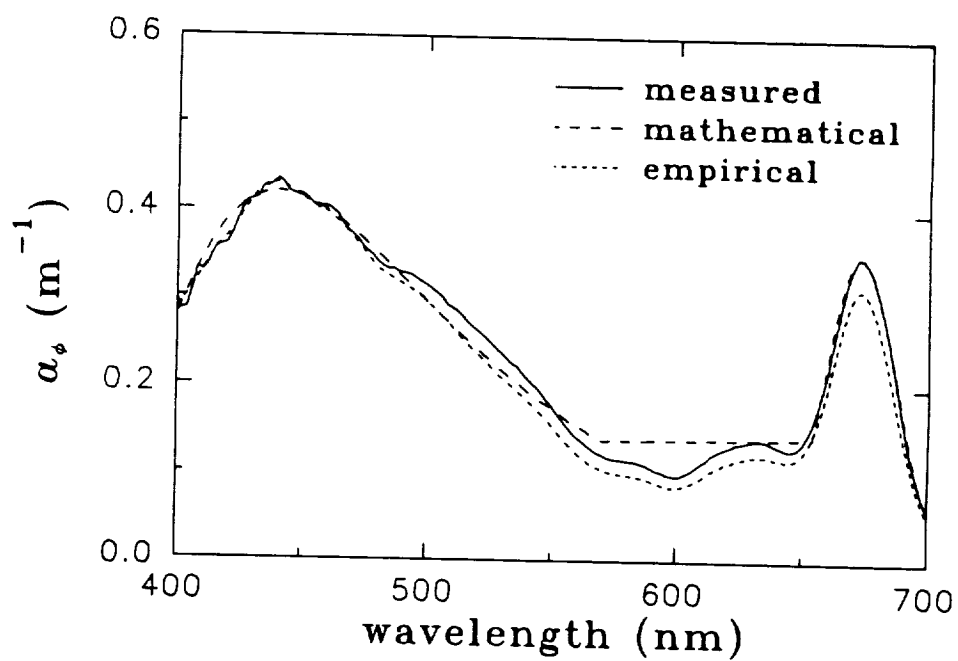
Figure 15d. Measured vs. Simulated a_ϕ for Station CO15.
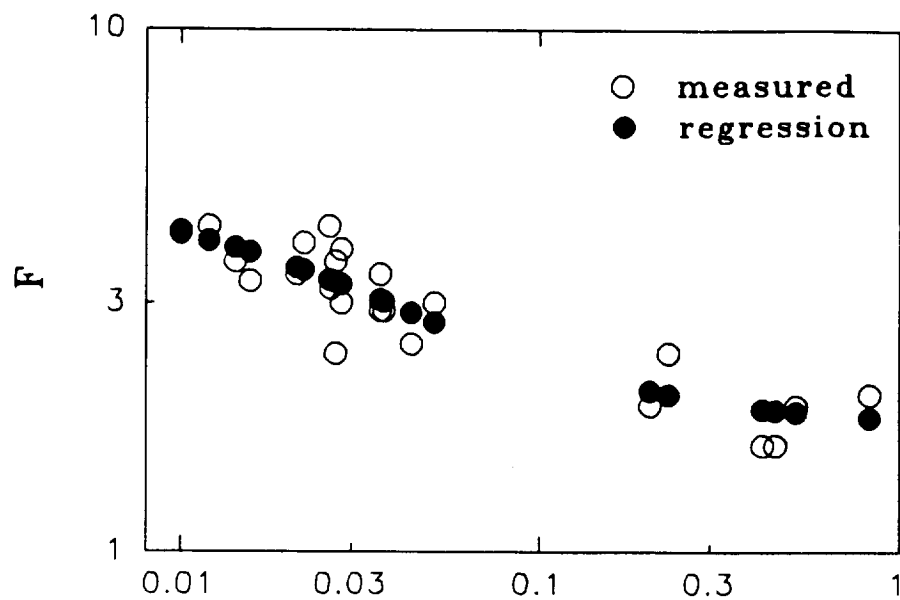
Figure 16a. Parameter F of a_ϕ Simulation vs. $a_\phi(440)$.
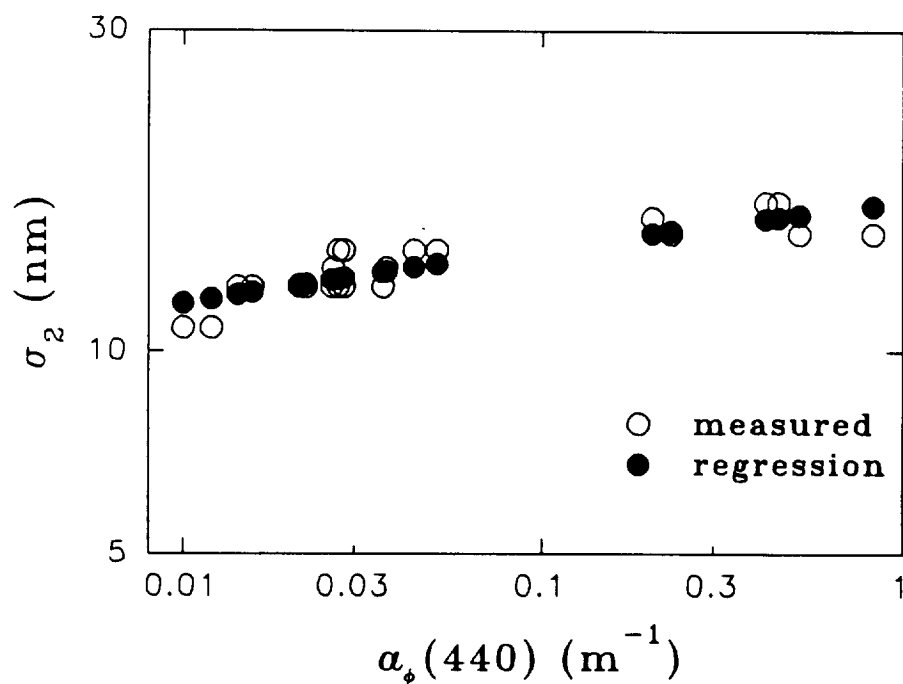
Figure 16b. Parameter σ_2 of a_ϕ Simulation vs. $a_\phi(440)$.
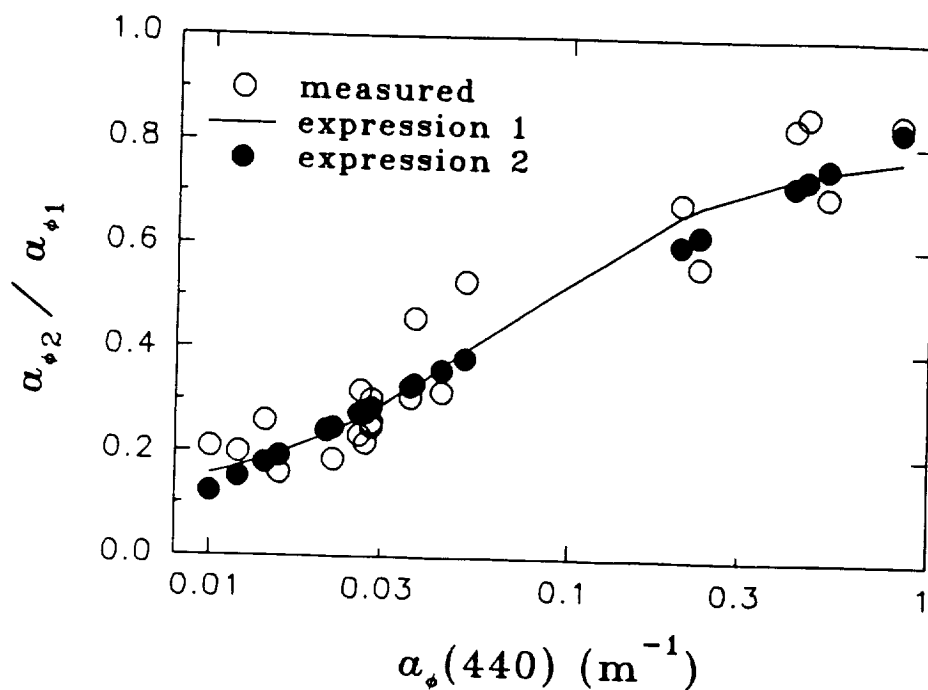
Figure 16c. Ratio $a_\phi(675)/a_\phi(440)$ vs. $a_\phi(440)$.
Solid curve: Eq. 54; filled circle: Eq. 55.

region of the a_ϕ curves. Thus, only 2 parameters, $a_{\phi l}$ and F, are important to the a_ϕ curve.

F, σ_2 and $a_{\phi 2}/a_{\phi l}$ are indicators of the "package effect". The greater the "package effect," the smaller the parameter F, the bigger the band-width $2.355\sigma_2$ and larger the ratio $a_{\phi 2}/a_{\phi l}$. That means, for *in vitro* phytoplankton pigment absorption coefficients (i.e. no "package effect"), from the above results, the "fatness" factor F will be close to 4.2, $a_{\phi 2}/a_{\phi l}$ around 0.2, and the half band-width $(2.355\sigma_2)$ around the red peak will be close to 21 nm (a similar value as reported by Hoepffner and Sathyendranath [1991]).

Unlike Lee et al. [1994b] who related the parameters to measured R_{rs}, the a_ϕ

parameters can be related to $a_\phi(440)$ after nonlinear regression analysis. Figures 16a -

16c show how those parameters relate to the measured $a_\phi(440)$. It is found that:

$$a_{\phi2}/a_{\phi1} = 0.86 + 0.16\ln(a_{\phi1}), \text{ normalized rms error: } 17.2\%,$$

$$F = 2.89\exp[-0.505\tanh[0.56\ln(a_{\phi1}/0.043)]], \text{ normalized rms error: } 12.4\%,$$

$$\sigma_2 = 14.17 + 0.9\ln(a_{\phi1}), \text{ normalized rms error: } 5.6\%.$$

In this way, the a_ϕ curve can still be estimated if the measured R_{rs} is contaminated by

bottom reflectance.

6.2.2 Empirical Relationship

For the measured surface a_ϕ of cruises GOMEX and COLOR, Carder et al.

[1994] found that for the SeaWiFS channels, $a_\phi(\lambda)/a_\phi(675)$ can be expressed by a

hyperbolic tangent function, i.e.

$$a_\phi(\lambda) = a_0(\lambda)e^{a_1(\lambda)\tanh[a_2(\lambda)\ln(a_\phi(675)/a_3(\lambda))]}a_\phi(675) , \qquad (54)$$

where the parameters a_0, a_1, a_2, and a_3 are empirically determined for each SeaWiFS

wavelength [Carder et al. 1994]. By the above expression, the value of $a_\phi(\lambda)/a_\phi(675)$

approaches an asymptote at very high or very low values of $a_\phi(675)$ (see Figure 16c).

For $a_\phi(440)$ in the range of 0.01 to 1.0 m^{-1} ([chl a] equivalent is in the range of

0.07 to 50 mg/m^3), a simplified expression is

$$\frac{a_\phi(\lambda)}{a_\phi(440)} = a_0(\lambda)+a_1(\lambda)\ln[a_\phi(440)] , \qquad (55)$$

with parameters a_0 and a_1 empirically derived for each wavelength and presented in Table 6.

Table 6. Parameters for the Empirical $a_\phi(\lambda)$ Simulation.

λ	a_0	a_1	r^2	λ	a_0	a_1	r^2
390	.5813	.0235	.057	560	.3433	.0659	.784
400	.6843	.0205	.081	570	.2950	.0600	.806
410	.7782	.0129	.058	580	.2784	.0581	.834
420	.8637	.0064	.032	590	.2595	.0540	.848
430	.9603	.0017	.005	600	.2389	.0495	.845
440	1.0	0	--	610	.2745	.0578	.875
450	.9634	.0060	.113	620	.3197	.0674	.892
460	.9311	.0109	.220	630	.3421	.0718	.898
470	.8697	.0157	.235	640	.3331	.0685	.893
480	.7890	.0152	.179	650	.3502	.0713	.891
490	.7558	.0256	.356	660	.5610	.1128	.884
500	.7333	.0559	.710	670	.8435	.1595	.893
510	.6911	.0865	.815	680	.7485	.1388	.886
520	.6327	.0981	.836	690	.3890	.0812	.840
530	.5681	.0969	.823	700	.1360	.0317	.751
540	.5046	.0900	.805	710	.0545	.0128	.645
550	.4262	.0781	.779	720	.0250	.0054	.531

Using these expressions (Eqs. 54 or 55), the number of unknowns related to $a_\phi(\lambda)$ is reduced to 1 ($a_\phi(675)$ or $a_\phi(440)$). However, with 4 or 2 parameters for each wavelength, the $a_\phi(\lambda)$ shape will no longer be the same for different waters, and the

changes of $a_\phi(\lambda)$ due to "package effect" or pigment composition are considered, at least to the first order.

Due to the limited data sets, it is improper to claim that the values in Table 6 are final and universally usable. However, these values work very well for the waters in this study. Improved empirical results are anticipated with increased data sets and better measurements.

In the following sections, simulations of $a_\phi(\lambda)$ by mathematical functions (Eqs. 51 - 53) and by empirical relationships (Eq. 55) are tested in the R_{rs} inversion for waters from the Monterey Bay and Gulf of Mexico, where both measured $R_{rs}(\lambda)$ and $K_d(\lambda)$ are available. In the application chapter, efforts are concentrated on using the mathematical simulation, however.

6.3 Derivation of the Absorption Coefficient from R_{rs}

From the above a_ϕ simulations, it is found that $a_\phi(440)$ is the most important parameter for the $a_\phi(\lambda)$ curve. The other parameters can either be fixed or be estimated from $a_\phi(440)$. For instance, for the mathematical simulation method, λ_1 and λ_2 can be fixed at 340 nm and 674 nm, respectively. If the relationships of $a_{\phi2}/a_{\phi1}$, σ_2 and F versus $a_{\phi1}$ are used in the R_{rs} inversion, the number of total unknowns is reduced to 5 for the N equations: $a_{\phi1}$, $a_{dg}(440)$, S_{dg}, X and Y. By minimizing the a.p.d. defined in section 4.1, it is possible to derive the 5 unknowns if $N \geq 5$. Before we do this, however, ranges for the unknowns have to be set as there exist

realistic limits for them. It is possible that values outside of these limits may provide smaller *a.p.d.* values.

For the exponent Y, there are no measurements available. Part of Y is η_b, and as discussed in section 1.4.2, η_b changes with particle size. Generally, it is assumed that $\eta_b \sim 1.0$ for open ocean and that $\eta_b \sim 0$ for coastal waters [Gordon and Morel 1983, Morel 1988], although η_b can be as high as 1.7 for river samples [Whitlock et al. 1981] and 3.0 for coccolithophorid blooms [Gordon et al. 1988]. Due to the similar curvature of the b_b and a_{dg} spectra, however, the range for Y cannot be simply set as $0 \leq Y \leq 3$, because when the absorption is dominated by a_{dg} (very common for coastal waters), the compensation between the a_{dg} and b_b parameters becomes strong. Therefore a narrow range for Y for each station must be specified. Previous model results yield a rough relationship similar to that of Carder et al. [1994]: $Y \approx 0.86 + 1.2\ln(\chi)$ with $\chi = R_{rs}(440)/R_{rs}(490)$. Thus, the range for Y is set as:

$$0.9 * (0.86+1.2\ln(\chi)) \leq Y \leq 1.1 * (0.86+1.2\ln(\chi)),$$

i.e., within 10% of the regression value and keeping $Y \geq 0$.

S_{dg}, which depends on the relative abundance between detritus and gelbstoff, varies from sample to sample [Roesler et al. 1989]. By considering a detritus-to-gelbstoff ratio less than 1.0, the range for S_{dg} is set as

$$0.012 \leq S_{dg} \leq 0.016,$$

as S_g varies from 0.011 nm^{-1} to 0.019 nm^{-1} for different materials [Carder et al. 1989, Hawes et al. 1992], and averaged about 0.014 nm^{-1} for ocean waters [Bricaud et al. 1981].

The ranges for $a_{\phi l}$, a_{d_g} and X are much easier to establish:

$$a_{\phi l} > 0, \ a_{d_g}(440) > 0, \text{ and } X > 0.$$

By minimizing the $a.p.d.$ defined in Chapter 4, the 5 unknowns are derived for each measured R_{rs} curve. Since there were R_{rs} values at ~ 180 channels from 400 nm to 850 nm for each station, there were about 180 equations available.

By using the above method, R_{rs} curves measured from waters of Monterey Bay and the Gulf of Mexico were inverted to determine the unknowns. The results and discussion are summarized in Chapter 7.

CHAPTER 7

RESULTS AND DISCUSSION OF THE INVERSE PROCESS

For R_{rs} curves measured from waters of Monterey Bay and the Gulf of Mexico, the parameters $a_{\phi l}$, $a_{d_g}(440)$, X and Y, as well as the total absorption coefficients $a(440)$, $a(486)$ and $a(550)$, were derived by minimizing the a.p.d. for each station. The variable estimates were obtained using Quattro Pro 5.00, by applying the quadratic feature.

For R_{rs} measurements, the measured L_{sky} may not be from the same part of the sky as that reflected off the sea-surface and entering the sensor when $L_u(0^+)$ is measured due to the sea-surface roughness. Cloudy conditions can worsen this mismatch. Therefore, instead of forcing $r = 0.018$, we let r and Δ in Eq. 39 be variables in the R_{rs} inversion; thus r and Δ were also derived when the a.p.d. was minimized. For the 45 stations available, the overall average a.p.d. is 3.4%.

From Eq. 27, $a(440)$, $a(486)$ and $a(550)$ were also derived from the measured $K_d(av)$. As $R_{rs} \approx 0.05 b_b/a$ (Eqs. 23 and 29),

$$a \approx \frac{K_d(av)}{1.08 D_d(0)(1+20R_{rs})} .$$ (56)

In the calculation of a by Eq. 56, two sets of $D_d(0)$ were used. One was $1/\cos(j)$, and

the other was derived by forcing the $K_d(av)$-derived $a(\lambda)$ to approximate $a_w(\lambda)$ + $a_p(\lambda)$ + $a_g(\lambda)$ for λ > 600 nm. In this way, errors due to sea surface roughness (wave focusing of light) and ship shadow can be reduced, and $D_d(0)$ can be estimated for cloudy days when j is uncertain.

7.1 Comparison of $a(440)$, $a(486)$ and $a(550)$ Derived Using R_{rs} and K_d Methods

Figures 17a - 17c compare the results of the total absorption coefficients derived from the R_{rs}-inversion and those from K_d methods (using derived $D_d(0)$) at 440 nm, 486 nm and 550 nm, respectively. From Figure 17a, it can be seen that R_{rs}-derived $a(440)$ is consistent with the K_d-derived $a(440)$, with $r^2 = 0.94$ (n=45), a slope equal to 1.03 and an average difference of 31% for $a(440)$ in the range of 0.03 m^{-1} to 2.5 m^{-1}. However, the average difference dropped to 19% for $a(440)$ less than 0.5 m^{-1}, perhaps because patchy data are more likely for turbid stations. When $1/\cos(j)$ was used to replace $D_d(0)$ to derive $a(\lambda)$ from $K_d(\lambda)$, the difference between the R_{rs}-derived and K_d-derived $a(440)$ was 73% for the whole $a(440)$ range. This indicates that the method used to derive $a(\lambda)$ from $K_d(\lambda)$ is preferable. These results also demonstrate that the method to obtain $a(\lambda)$ from $R_{rs}(\lambda)$ inversion works very well even for this wide range of water types.

The 31% difference between the results can be caused by the following factors:

1) the errors in the measurements of L_u, L_{sky}, $E_d(0^+)$ and $E_d(z)$, which will be transferred to R_{rs} and K_d; 2) simplifications in the model development; 3) errors in a_ϕ
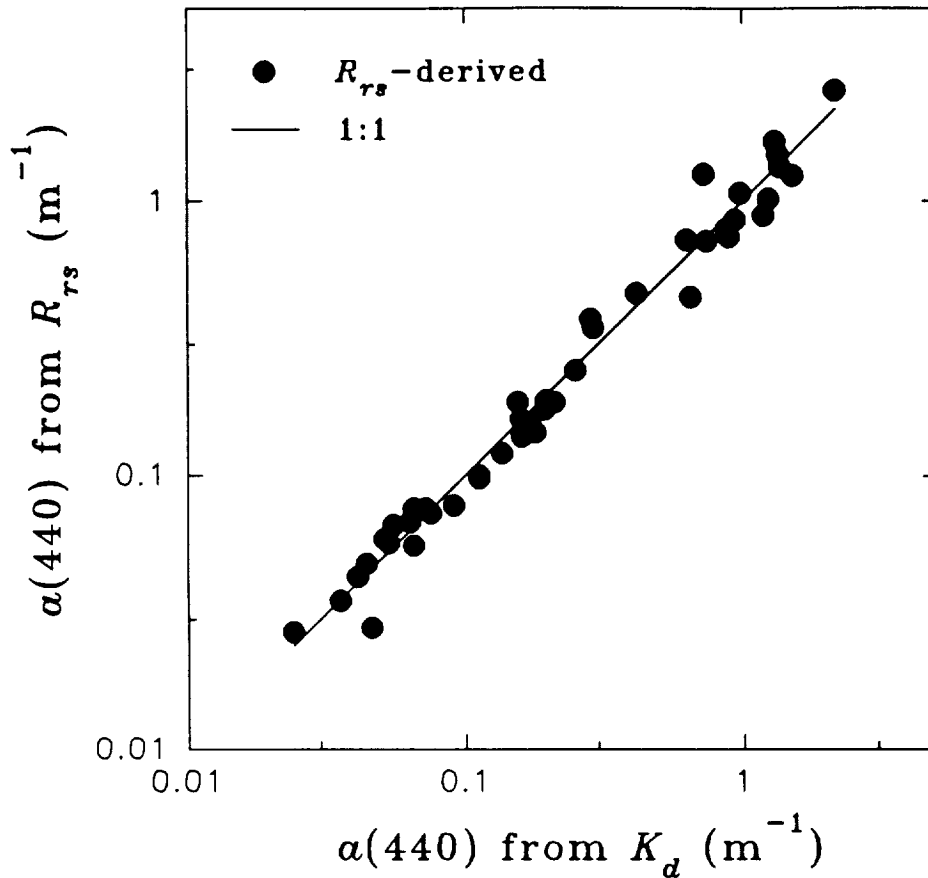
Figure 17a. Comparison of R_{rs}-derived to K_d-deriv d $a(440)$.
For Details See Text.

simulation; 4) water inconsistencies between the R_{rs} and K_d measurements (temporal and spatial patchiness); and 5) method to obtain a from K_d. With the consideration of these possible sources of error, a 31% difference seems rather small, and it can be claimed that we can not only qualitatively, but quite accurately derive the in-water absorption coefficient using remote-sensing techniques.

Figures 17b and 17c compare $a(486)$ and $a(550)$ derived using the two methods. r^2 for $a(486)$ is 0.97 (slope 1.04) between the two sets of results, with an average
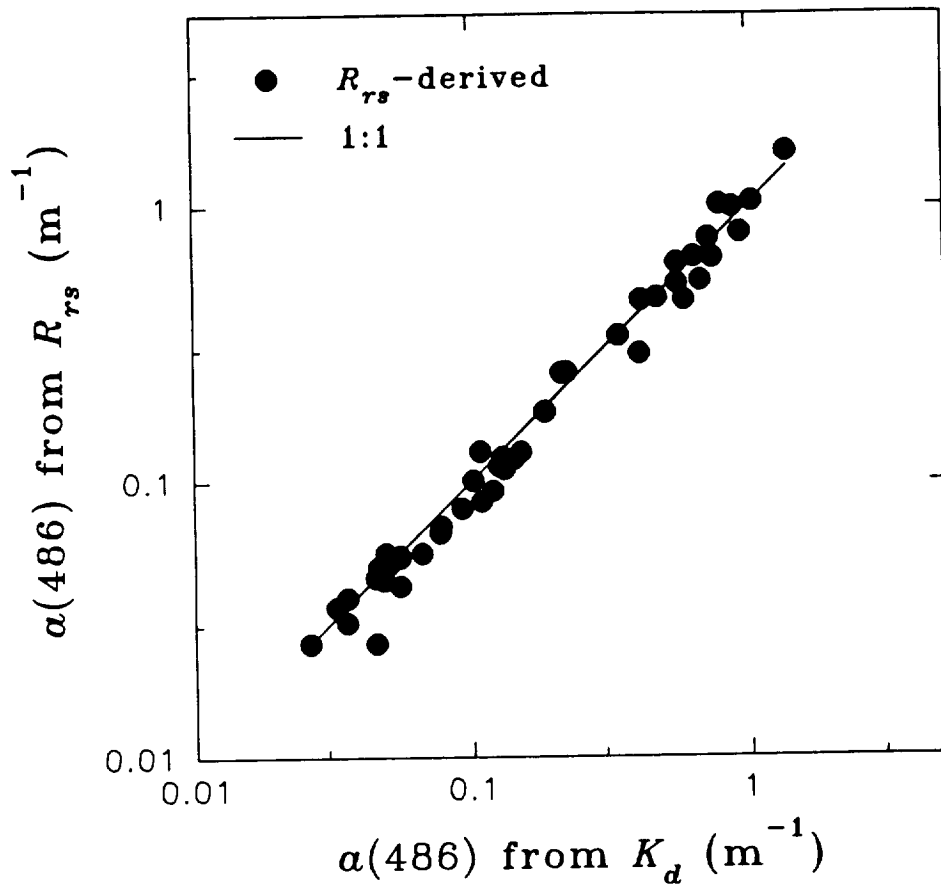
Figure 17b. Comparison of R_{rs}-derived to K_d-derived $a(486)$.
For Details See Text.

error of 21%, while r^2 for $a(550)$ is 0.97 (slope 0.87) with average error of 25%. The

0.87 slope for $a(550)$ means that the $a(550)$ derived by R_{rs} inversion is consistently

lower than that derived by $K_d(av)$, with the implication that most of the 25%

difference are systematic rather than random. One speculation is that simulated

$a_\phi(550)$ might be low because of a large F value. This does not always happen,

however; for many clear water situations, where phytoplankton particles are small and

less "package effect" occurs, the simulated $a_\phi(550)$ is usually greater than the
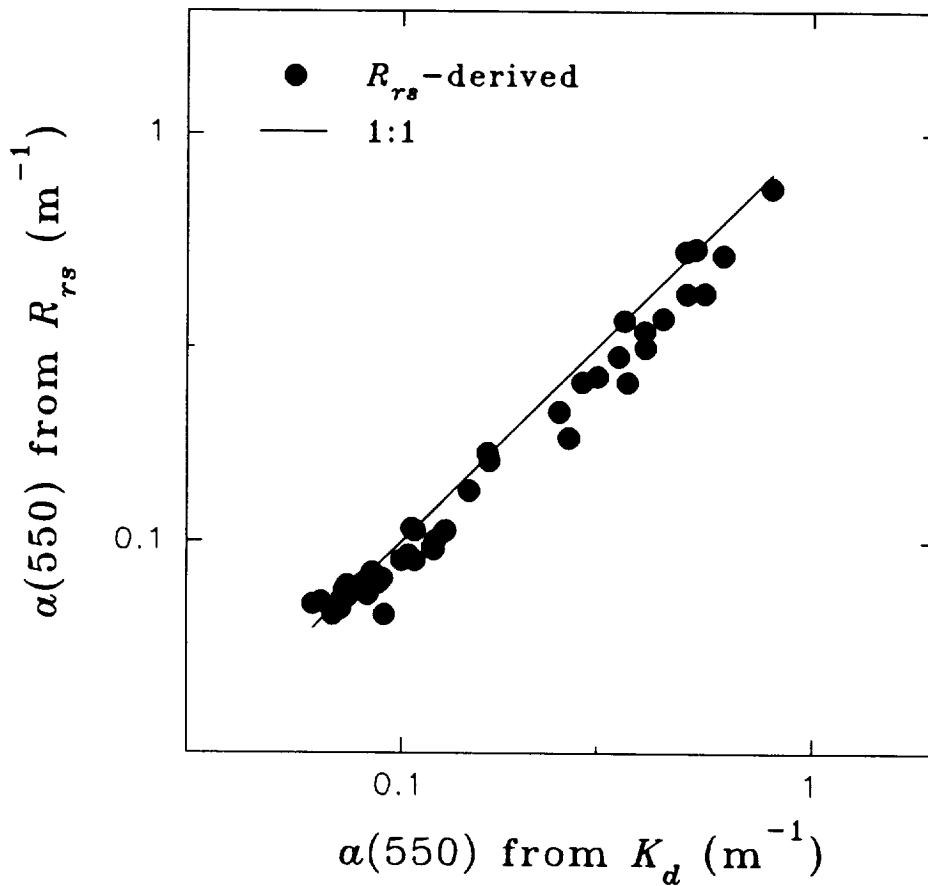
Figure 17c. Comparison of R_{rs}-derived to K_d-derived $a(550)$.
For Details See Text.

measured $a_\phi(550)$. Furthermore, for clear water, most of $a(550)$ come from $a_w(550)$ (≈ 0.064 m^{-1}), so error in $a_\phi(550)$ simulations has only little influence on $a(550)$, and it could not explain the 0.87 slope for clear water. Other possible sources of errors include the pure water absorption coefficient, the measurement of $E_d(z)$, and the possibility that the actual $D_d(0)$ for 550 nm might be higher than the derived values since D_d increases with scattering [Kirk 1991]; and there were relatively higher b_b/a

ratio at 550 nm for many waters. However, how much higher $D_d(0, 550)$ should be is not clear. Further study is needed on this issue.

7.2 Comparison of R_{rs}-derived $a(440)$, $a(486)$ and $a(550)$ Using Simulated a_ϕ and Measured a_p

In order to see how the simulated a_ϕ curve performs compared to the measured a_p curve, the R_{rs} inversion process was also undertaken using the measured a_p curve for each station. This time, it was assumed that we knew the curvature (shape) of a_p for each station, but not the magnitude. The factor f was applied to the measured a_p with no limitation set for its range. f was then derived by minimizing a.p.d.. Eq. 9 was used for $a_g(\lambda)$ because a_d was contained in a_p. The range for S_g was set as 0.013 $\leq S_g \leq$ 0.017 nm^{-1}, and the same range for Y as in section 6.3 was used. By the same process described in section 6.3, f, $a_g(440)$, S_g, X and Y were derived by minimizing a.p.d..

Figures 18a - 18c compare the results of R_{rs}-derived $a(440)$, $a(486)$ and $a(550)$ values determined using the measured a_p curves versus those determined using the simulated a_ϕ curves. It can be seen that the results at all three wavelengths show close agreement. For the mathematical a_ϕ simulation (Eqs. 51 - 53), the r^2 values for $a(440)$, $a(486)$ and $a(550)$ are 0.99 (n=48), while the average difference is 15.2% for $a(440)$, 10.3% for $a(486)$ and 10.5% for $a(550)$. For the empirical relationships (Eq. 55), the r^2 is 0.98 for $a(440)$, and 0.99 for $a(486)$ and $a(550)$ (n=48), while the average difference is 23.2% for $a(440)$, 18.6% for $a(486)$ and 10.6% for $a(550)$.
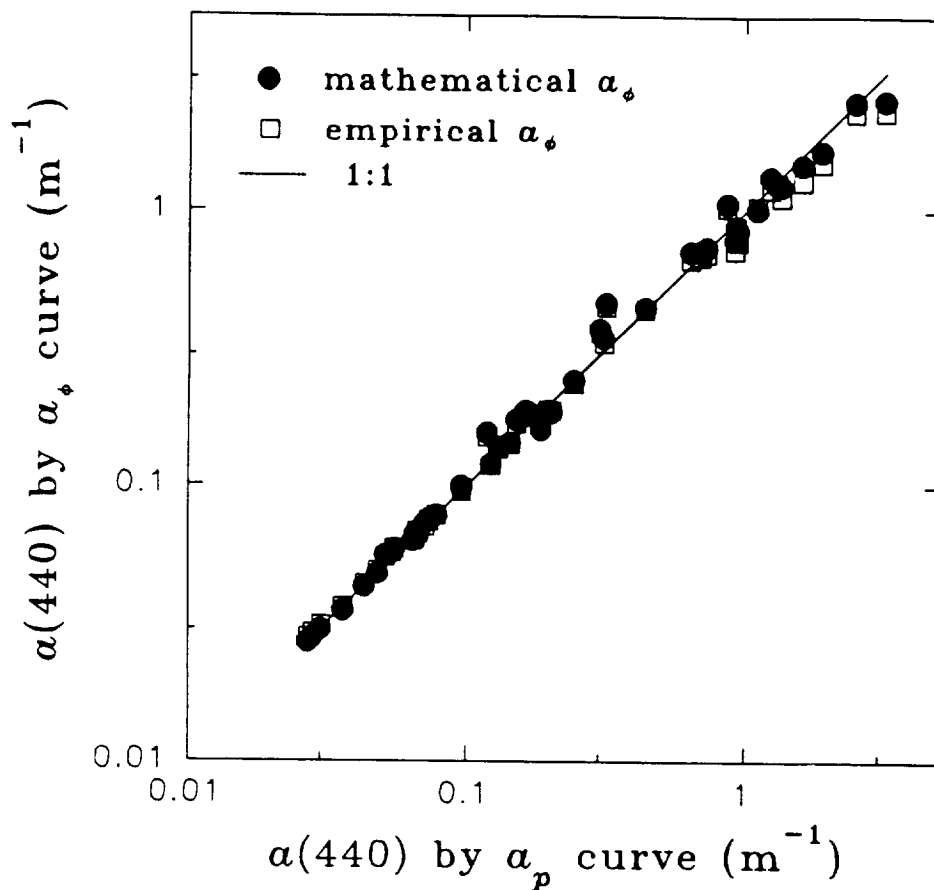
Figure 18a. Comparison of R_{rs}-derived $a(440)$ Using Simulated a_ϕ and Measured a_p.

The empirical a_ϕ simulation causes higher differences for the three absorption coefficients, which might be due to the simplification in the a_ϕ expression. From these results, we can say that the simulated a_ϕ curves work very well for the R_{rs} inversion process and can be used to replace the measured a_p curve.

In this process, the factors f for each station were also derived. For all stations, it varied from 0.18 to 2.34 with an average of 0.94, and more than 70% of the values fell in the range 0.7 to 1.3. Part of the f variation can be explained by
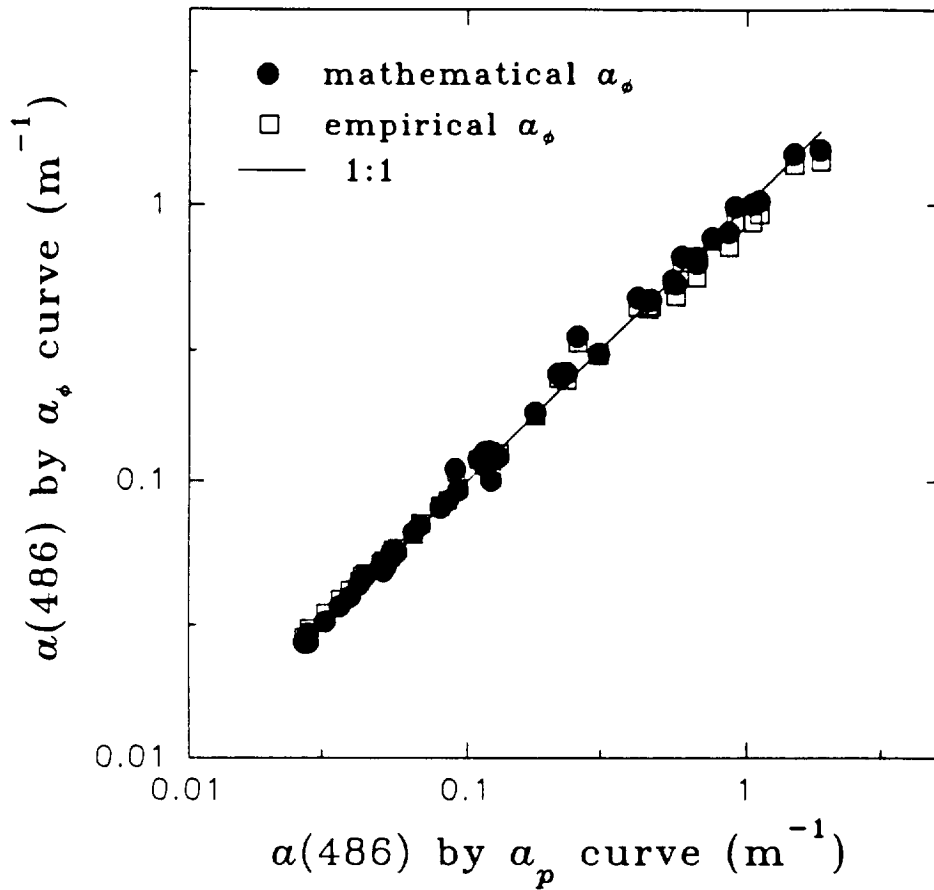
Figure 18b. Comparison of R_{rs}-derived $a(486)$ Using Simulated a_ϕ
and Measured a_p.

patchiness and vertical structure, as the measured a_p from one position may not represent the effective particle absorption coefficient of the upper water column, especially when a strong vertical structure exists. Additionally, f includes the errors introduced in the model development, variation of a_w, and compensation among the parameters.

For ideal situations, i.e. the water column is well mixed, correct values for a_w, a_g and scattering are used, and the R_{rs}-inversion process is well performed, f will be a
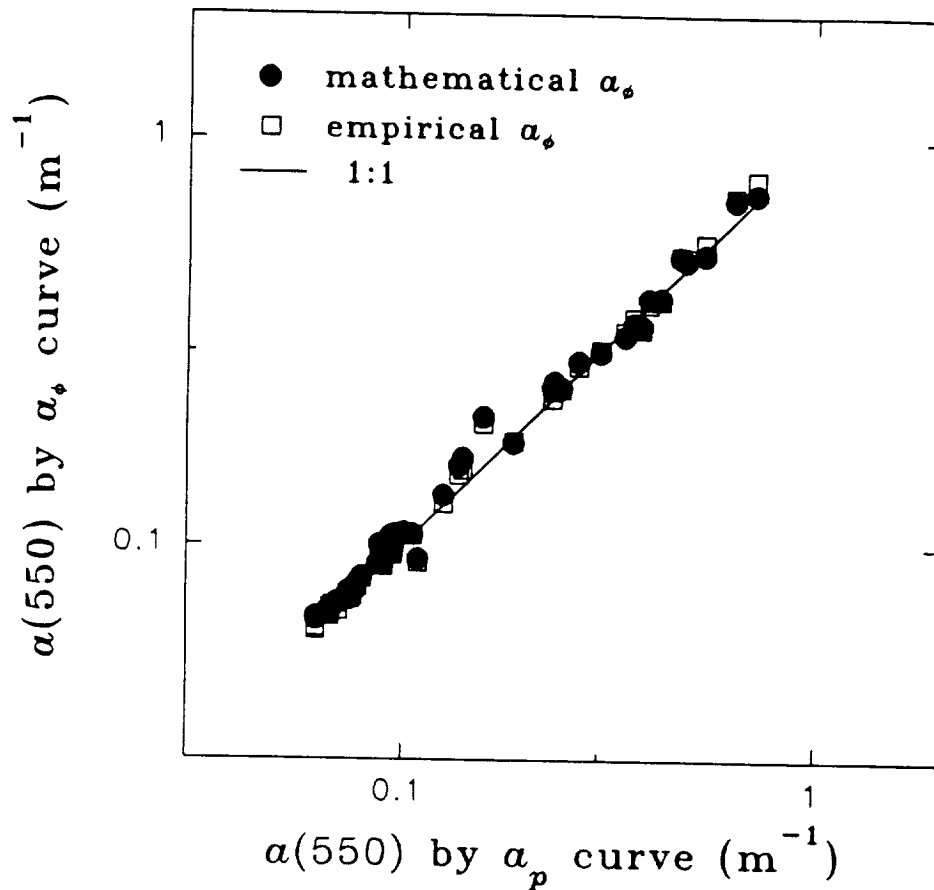
Figure 18c. Comparison of R_{rs}-derived $a(550)$ Using Simulated a_ϕ
and Measured a_p.

factor correcting the "beta factor" used in the a_p calculation, since it is difficult to

determine which "beta factor" is appropriate for our field samples (see Table 2 and

Figure 12) as discussed in section 4.2. For offshore waters, pigment absorption

coefficient is generally low. If the volume of filtered sea water is not enough, it is

quite possible that the filer pad OD_p is less than 0.10 (a_p equivalent is ~ 0.06 m^{-1} if

the volume is 500 ml with GF/F 25 mm filter and using the "beta factor" of Bricaud

and Stramski [1990]) where β_{pad} varies most. Thus, for better measurement of a_p
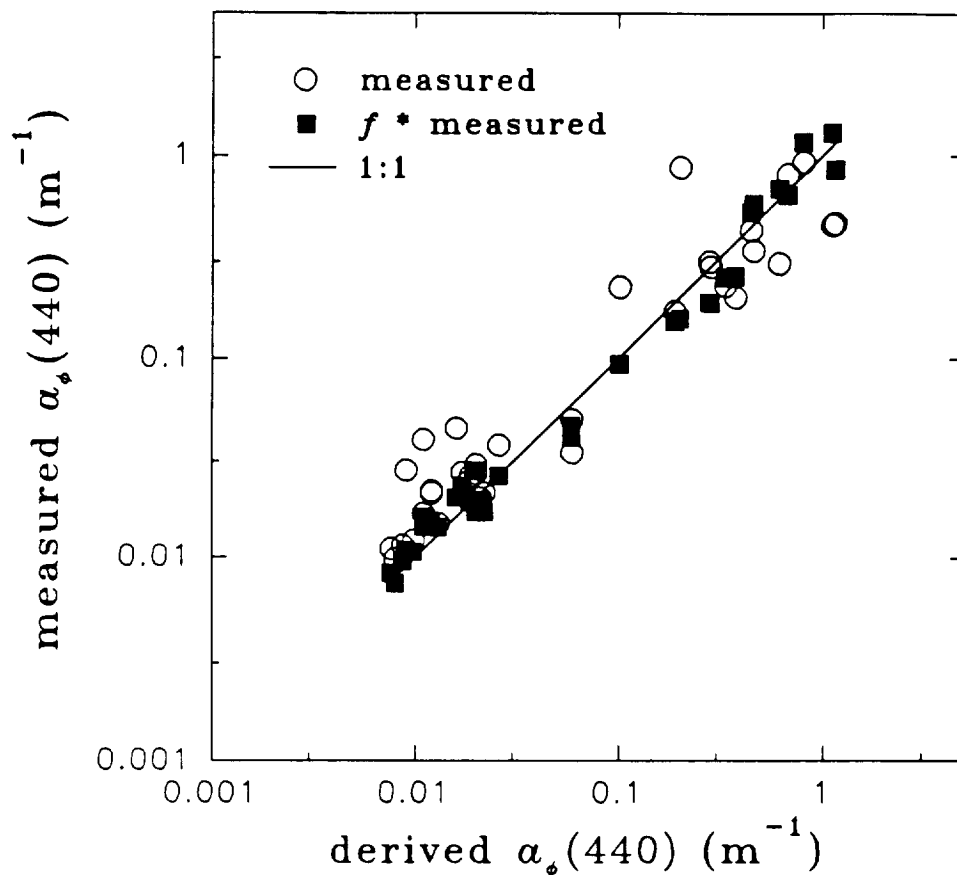
Figure 19. Comparison of R_{rs}-derived $a_\phi(440)$ to the Measured $a_\phi(440)$.

regardless of the "beta factor" used, a large volume of water sample must be filtered in order to reduce the "beta factor" uncertainties; this is consistent with a recent independent study by Patch et al. (in preparation).

7.3 Comparison of R_{rs}-derived $a_\phi(440)$ to Measured $a_\phi(440)$

Using the a_ϕ simulations described in section 6.2, surface layer a_ϕ values

could be derived just from R_{rs} without prior knowledge of the "package effect" or the chlorophyll-specific absorption coefficients. Figure 19 compares the derived $a_\phi(440)$ to the measured $a_\phi(440)$. The r^2 is 0.55 (n=36), but it becomes 0.92 (with 46% difference) if f is applied to the measured values, where the f values were derived as in section 7.2. As pointed out by Gordon and Clark [1980] and Gordon [1992], derived values from R_{rs}-inversion are optical averages of the upper water column, which can not be directly compared to in-water measurements made at a discrete position when the water is not homogeneous. Hence, f might be needed to compensate for possible differences due to water patchiness, vertical structure, and/or the "beta factor." These results indicate that at this stage, the $a_\phi(440)$ values derived by the R_{rs}-inversion method can be accurate to within 50% of the phytoplankton absorption at 440 nm in the upper water column.

CHAPTER 8

APPLICATIONS

8.1 Introduction

Since an overflight can view a large area of the ocean in a short time period, applications of remote sensing via aircraft or satellite have become increasingly popular and important. These applications include surveys of pollutant flow, sediment transport, ocean circulation, estimation of [chl a] and [YS], modeling the water color at depth, and estimation of primary production, etc. In the following sections, some of these applications will be discussed, as well as the modeling of upwelling radiance of Tampa Bay measured from a low flying aircraft.

8.2 Estimation of Chlorophyll Concentration

The amount of phytoplankton in the ocean, often measured by the concentration of chlorophyll a ([chl a]), contributes significantly to regulation of the global climate system through its effect on the carbon cycle. It also indicates the trophic status of waters, and contributes to the conversion of light into heat.

Since the 1970's, efforts have been made to remotely estimate [chl a] in the

ocean. Empirical and semi-analytical algorithms have been reported for different waters and seasons [Gordon et al. 1980; Gordon and Morel 1983 and references cited there; Carder et al. 1991; Carder et al. 1994].

Applying the analytically derived $a_\phi(440)$ and the relationship between $a_\phi(440)$ and $a_\phi(675)$, [chl a] can be derived through

$$[chl\ a] = \frac{a_\phi(440)(0.86 + 0.16\ln(a_\phi(440)))}{a_\phi^*(675)} , \tag{57}$$

where $a_\phi^*(675)$ is the chlorophyll-specific absorption coefficient at 675 nm.

In addition to the $a_\phi(440)$ value derived from R_{rs}-inversion, the derivation of [chl a] depends on $a_\phi^*(675)$ if we use Eq. 57. This value varies regionally and seasonally, but it has been shown to be more stable than $a_\phi^*(440)$ as there is less influence due to the "package effect" at 675 nm [Carder et al. 1994]. Thus, if we know the value of $a_\phi^*(675)$, [chl a] can be derived using Eq. 57 with the R_{rs} derived $a_\phi(440)$.

It is necessary to keep in mind that R_{rs}-derived [chl a] is an optically averaged value of the upper water column [Gordon and Clark 1980, Gordon 1992]. Only when the water column is well mixed, can R_{rs}-derived [chl a] be directly compared to measured [chl a] from a discrete location.

8.3 Estimation of the Gelbstoff Absorption Coefficient

Generally, a_d and a_g have similar absorption spectra in the visible wavelengths,

so it is not easy to clearly separate a_g from a_{dg}, unless by active remote sensing such as laser induced gelbstoff fluorescence [Hoge et al. 1993]. The scattering effects of detritus and gelbstoff are different, however, making it possible to estimate $a_d(440)$ from the X or R_{rs} values. Then $a_g(440)$ can be separated from the R_{rs}-derived $a_{dg}(440)$ as discussed in sections 6.3 and 7.1.

Figure 20 shows the relationship between measured $a_d(440)$ and the derived X values. In the log-log format, r^2 between $a_d(440)$ and X is 0.89 (n = 39); and the best regression fit is

$$a_d(440) = 61.44 X^{1.31} .$$ (58)

Thus, with the $a_{dg}(440)$ and X values derived by R_{rs} in section 7.1,

$$a_g(440) = a_{dg}(440) - 61.44 X^{1.31}.$$

Eq. 58 might be strongly driven by the sediments from the Mississippi River. For other regions, different regression results may occur. Also, there may be a difference between the "beta factor" of detritus and that of phytoplankton [Bricaud and Stramski 1990, Nelson and Robertson 1993]. More data sets and better measurements are expected to improve Eq. 58.

As $a_g(440) = a_g^*(440) * [YS]$, it is possible to estimate the gelbstoff amount if we know the gelbstoff-specific absorption coefficient, $a_g^*(440)$. Unfortunately, as with the chlorophyll-specific absorption coefficient, $a_g^*(440)$ varies for different sources of gelbstoff [Carder et al. 1989, Hawes 1992], making it difficult to estimate [YS]. How $a_g^*(440)$ varies is beyond the scope of this research, although we can choose an averaged $a_g^*(440)$ value for the calculation of [YS].
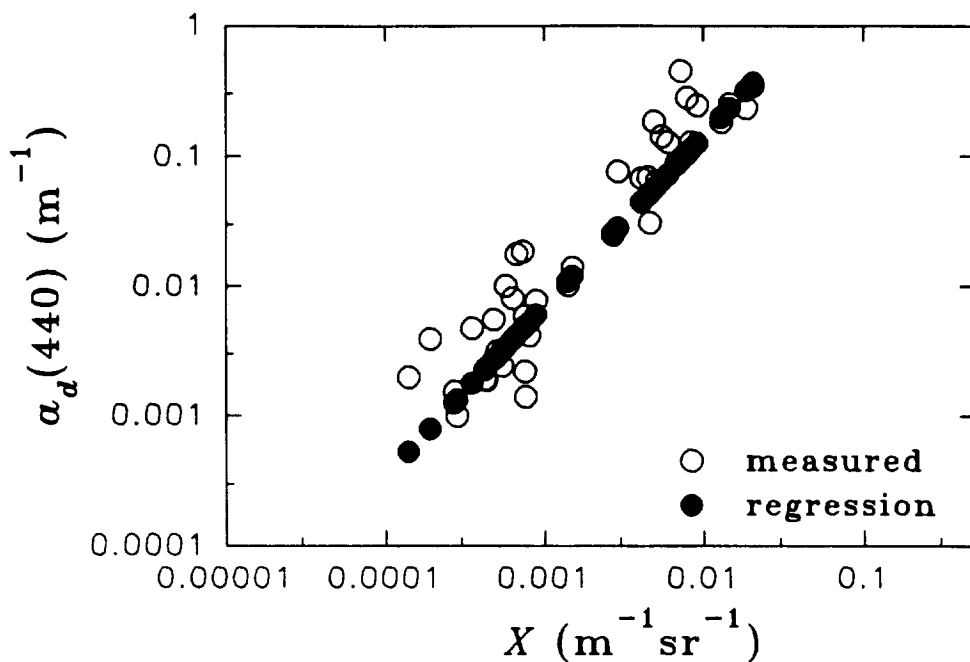
Figure 20. R_{rs}-derived X vs. Measured $a_d(440)$.

8.4 Algorithm for the Absorption Coefficient at 490 nm, $a(490)$

Optical water types can be classified by the attenuation or absorption coefficient at 490 nm [Jerlov 1976; Austin and Petzold 1981], and $1/K_d(490)$ yields a measure of the penetration depth of solar light [Gordon and McCluney 1975] in meters. By analyzing the diffuse attenuation coefficient $K(490)$ (which is proportional to $K_d(490)$) and the in-water upwelling radiance ratio at 443 and 550 nm, Austin and Petzold [1981] developed the algorithm

$$K(490) = 0.0883\left(\frac{L_u(443)}{L_u(550)}\right)^{-1.491} + 0.022 \ , \qquad (59)$$

where the 0.022 is the attenuation coefficient of pure sea water at 490 nm [Austin and Petzold 1981] in units of m^{-1}.

Applying this algorithm to the West Florida Shelf data and other stations, Carder et al. [1992] found that the correlation between $a(490)$ and the ratio $R_{rs}(442)/R_{rs}(550)$ is less than that between $a(490)$ and $R_{rs}(520)/R_{rs}(560)$ (Figure 21a). This may partly be explained by the influence of bottom reflectance and other components that do not co-vary with chlorophyll for "case 2" waters.

For regions that include shallow, coastal and "case 2" waters, an algorithm similar to Eq. 59 is presented for the calculation of $a(490)$ based on the study of 45 stations. These stations include blue-sky and cloudy sky conditions. Alternatively, $a(490)$ could be analytically derived by using high-resolution R_{rs} values as discussed in sections 6.3 and 7.1.

For the algorithm development, K_d-derived $a(490)$ ($\approx a(486)$, using derived $D_d(0)$) is considered as the true value. Figure 21a shows the relation between the reflectance ratio and K_d-derived $a(490)$. For $a(490)$ ranged from 0.03 to 1.5 m^{-1}, it is found that r^2 is 0.96 (n=45) between $\ln(a(490))$ and $\ln(R_{rs}(520)/R_{rs}(560))$, while r^2 is 0.89 between $\ln(a(490))$ and $\ln(R_{rs}(442)/R_{rs}(550))$. Thus, for the best fit, an algorithm for $a(490)$ is
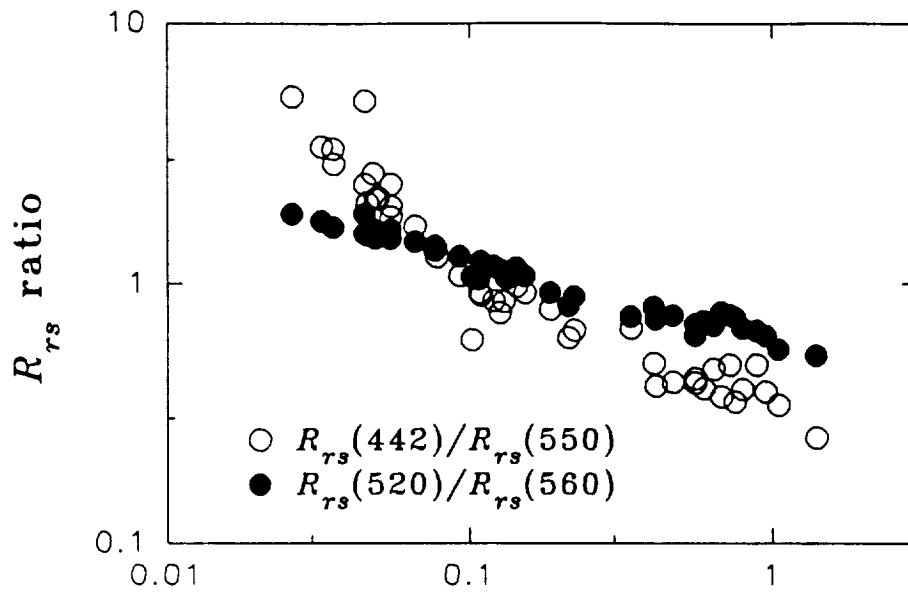
Figure 21a. $a(490)$ vs. $R_{rs}(442)/R_{rs}(550)$ and $R_{rs}(520)/R_{rs}(560)$.
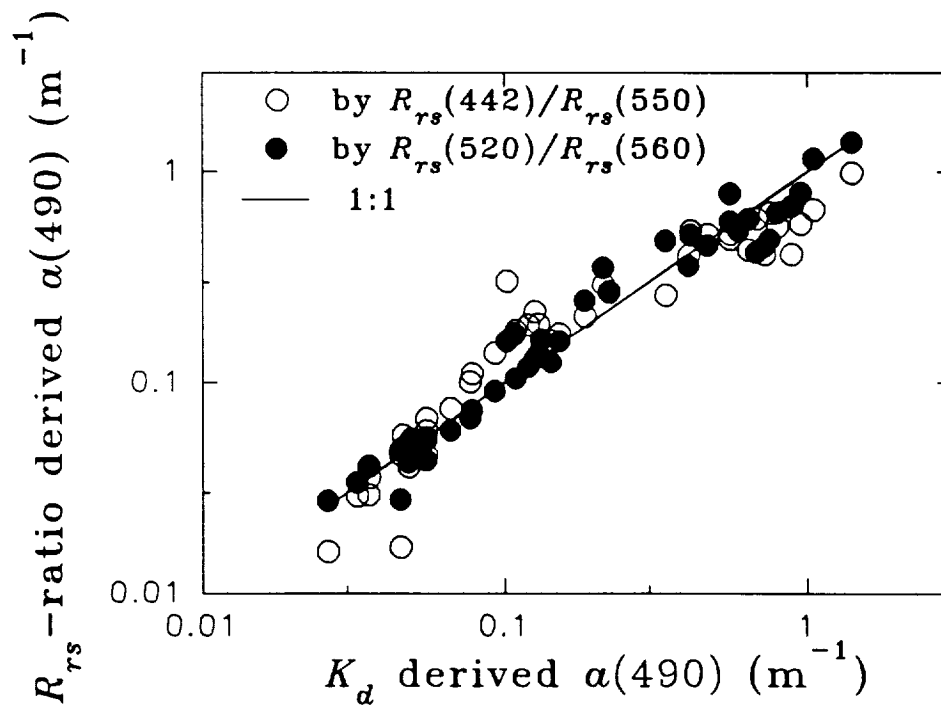
Figure 21b. Comparison of the $a(490)$ Algorithms.

$$a(490) = 0.19\left(\frac{R_{rs}(520)}{R_{rs}(560)}\right)^{-3.11} , \tag{60}$$

with average error of 32.5%. However, if the ratio $R_{rs}(442)/R_{rs}(550)$ is used instead, the best fit generates

$$a(490) = 0.15\left(\frac{R_{rs}(442)}{R_{rs}(550)}\right)^{-1.37} , \tag{61}$$

with average error of 49.6%. Remember that the error was only 21% when the hyperspectral R_{rs}-inversion method (section 7.1) was employed. Figure 21b shows the results from Eq. 60 and Eq. 61.

8.5 Modeling the Water Color at Depth

Combining Eqs. 27 and 44, one can derive

$$E_d(z) \approx E_d(0^-)e^{-1.08D_d(0)az} . \tag{62}$$

Since $D_d(0) \approx 1/\cos(j)$ [Gordon 1989a], $E_d(z)$ can be modeled if $E_d(0^-)$ and a are known. From sections 6.3 and 7.1, a can be derived from R_{rs} inversion, and $E_d(0^-)$ can be calculated by models [Gregg and Carder 1990, Bishop and Rossow 1991]. As examples, Figures 22a - 22d show the modeled versus measured $E_d(z)$ for station GO10 at wavelengths 440, 486, 520 and 550 nm, respectively, with $E_d(0^-)$

$$E_d(440) \ (\mathrm{W/m^2})$$
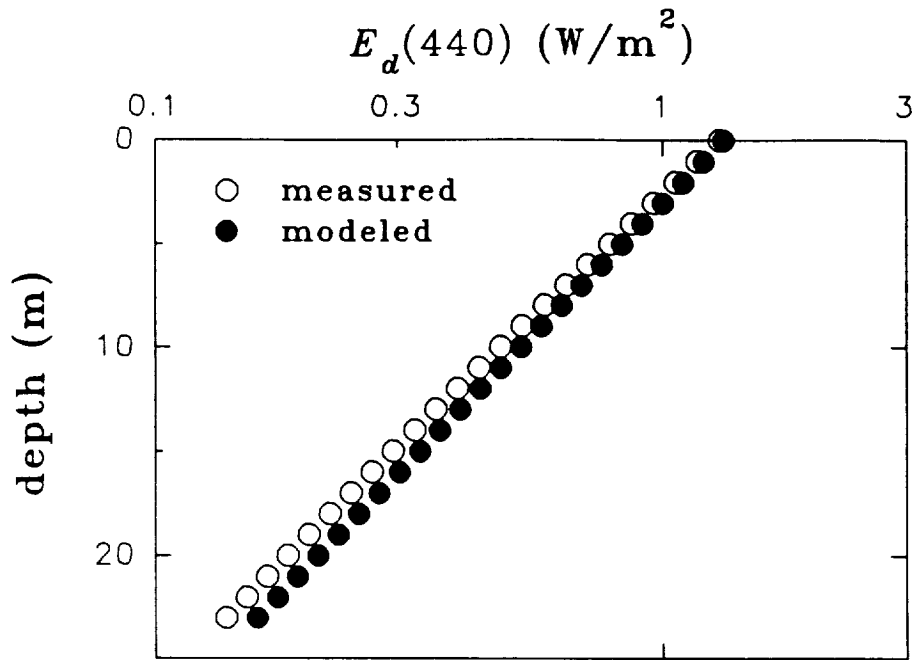
Figure 22a. Measured vs. Modeled $E_d(440)$ of Station GO10.

$$E_d(486) \ (\mathrm{W/m^2})$$
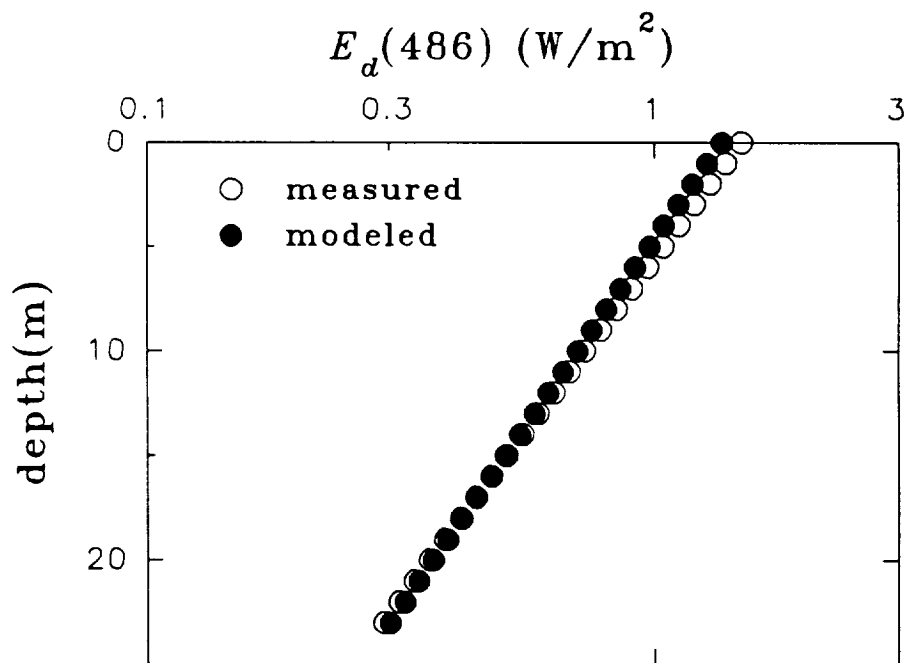
Figure 22b. Measured vs. Modeled $E_d(486)$ of Station GO10.
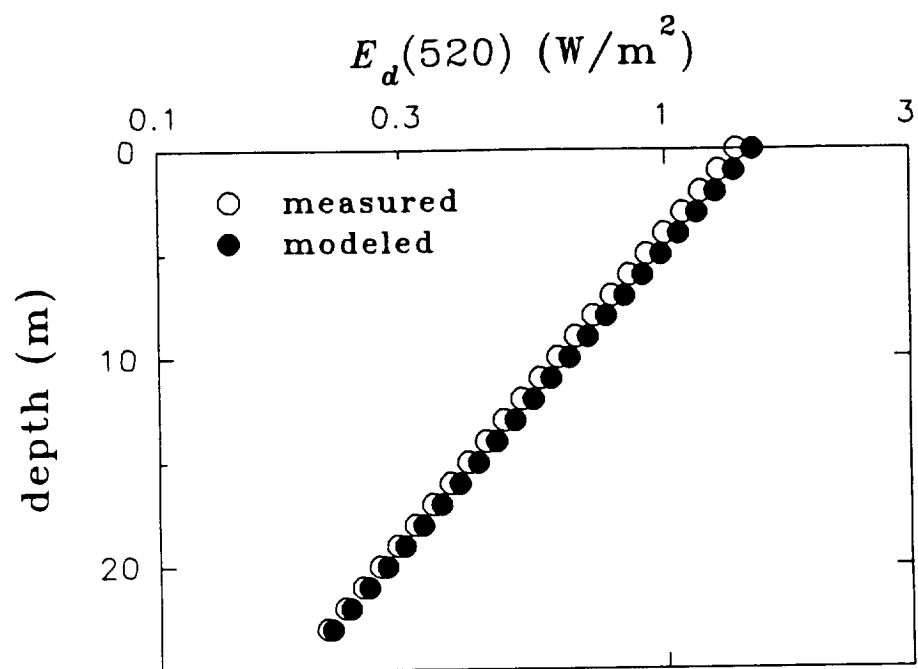
Figure 22c. Measured vs. Modeled $E_d(520)$ of Station GO10.
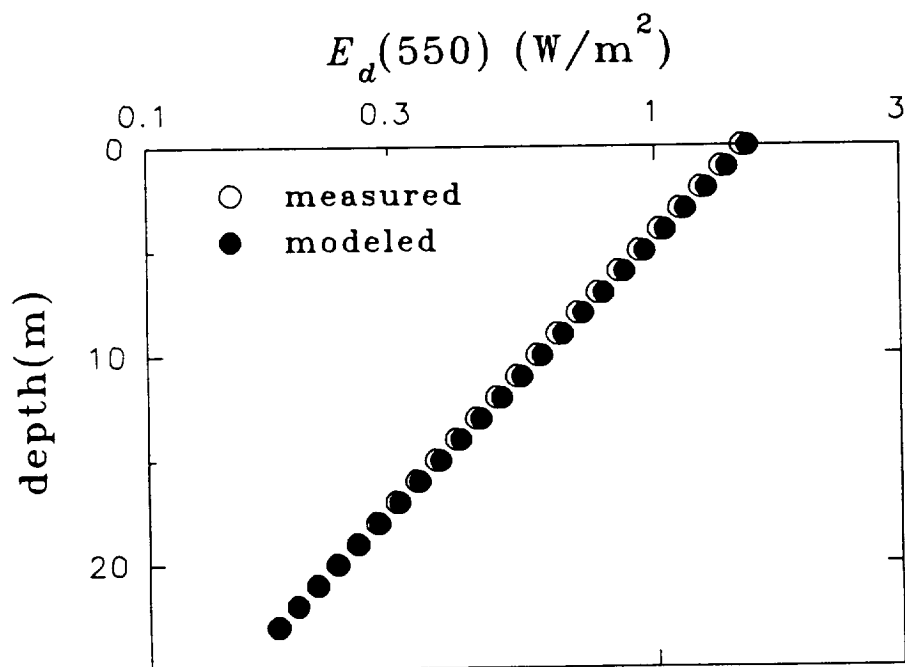
Figure 22d. Measured vs. Modeled $E_d(550)$ of Station GO10.

calculated by the model of Gregg and Carder [1990]. It can be seen that the model

gives very close subsurface irradiance (about 10% difference) compared to the

measured values; and the calculated irradiance profiles were consistent with the

measured for the upper water column.

8.6 Estimation of Primary Production

In the past decades, primary production models have been based on pigment

concentration, either by light available (P-I relationship of Platt et al. [1991]) or light

absorbed (P-AQ relationship of Bidigare et al. [1992]), using spectral or non-spectral

expressions. Recent popular models use the light absorbed approach, i.e.: chlorophyll

a concentration multiplied by the irradiance and two factors: averaged chlorophyll-

specific absorption coefficient, and the quantum yield for carbon fixation. Thus the

photosynthesis rate at depth z is [Kishino et al. 1986, Smith et al. 1989, Cullen 1990,

Morel 1991, Marra et al. 1992, Zaneveld et al. 1993]:

$$PP(z) = \phi(z)[chl\ a]\overline{a_\phi^*}PAR(z) , \qquad (63)$$

where $\phi(z)$ is the quantum yield for carbon fixation, and [chl a] is the chlorophyll a

concentration (mg/m^3). $\overline{a_\phi^*}$ is the spectrally-averaged chlorophyll-specific absorption

coefficient over 400 - 700 nm (m^2(mg chl a)$^{-1}$):

$$\bar{a}_\phi^* = \frac{\int_{400}^{700} \frac{a_\phi(\lambda)}{[chl\ a]} E_o^q(z,\lambda)d\lambda}{\int_{400}^{700} E_o^q(z,\lambda)d\lambda} , \qquad (64)$$

and $PAR(z)$ is the photosynthetically available irradiance, computed by

$$PAR(z) = \int_{400}^{700} E_o^q(z,\lambda)d\lambda , \qquad (65)$$

where $E_o^q(z,\lambda)$ in Equations 64 and 65 is the spectral scalar irradiance in quanta/m^2/nm/s. From Sathyendranath and Platt [1988],

$$E_o^q(z,\lambda) \approx E_o^q(0^-,\lambda)e^{-K_d(\lambda)z} . \qquad (66)$$

Quantum yield ϕ, a measure of the phytoplankton growth rate [Platt 1986], varies with light intensity, physiological status, temperature and nutrient stress of the phytoplankton population [Langdon 1988, Cleveland et al. 1989, Smith et al. 1989]. We choose the empirical formula suggested by Kiefer and Mitchell [1983] to express how ϕ changes with PAR,

$$\phi(z) = \phi_m \frac{PAR_\phi}{PAR_\phi + PAR(z)} , \qquad (67)$$

where ϕ_m is the maximum quantum yield, PAR_ϕ (K_ϕ in Smith et al. 1989) is the PAR value at which $\phi = \phi_m/2$.

Therefore, combined with the photoinhibition expression suggested by Platt et al. [1980], primary production at depth z can be expressed as

$$PP(z) = AP(z)\frac{\phi_m PAR_\phi}{PAR_\phi + PAR(z)}e^{-\nu PAR(z)} , \tag{68}$$

with

$$AP(z) = \gamma[C]\overline{a_\phi^*}PAR(z) , \tag{69}$$

where ν in Eq. 68 is a parameter to describe photoinhibition.

Eq. 69 accounts for the absorbed photons by the phytoplankton pigments, in which γ determines the fraction of chlorophyll a relative to the total pigment and phaeo-pigment concentration $[C]$.

Traditional estimates of primary production based upon remote measurements are accomplished using Eqs. 68 and 69, i.e. $[C]$ is estimated first from remotely measured signals [Vargo et al. 1987, Platt et al. 1991, Balch et al. 1992] using, for example, the CZCS algorithm:

$$[C] = A_1\left[\frac{L_w(443)}{L_w(550)}\right]^{A_2} \approx 0.95^{A_2}A_1\left[\frac{R_{rs}(443)}{R_{rs}(550)}\right]^{A_2} , \tag{70}$$

where $A_1 = 1.13$ and $A_2 = -1.71$ [Gordon et al. 1983]. The 0.95 value comes from $E_d(443)/E_d(550) \approx 0.95$. With this estimated $[C]$, the diffuse attenuation coefficient of irradiance can be approximated by the empirical relationship suggested by Morel [1988]:

$$K_d(\lambda) = K_w(\lambda) + d(\lambda)[C]^{e(\lambda)} , \tag{71}$$

in which values for K_w, d and e are found in tables calculated by Morel [1988].

With the measured or calculated $E_o^q(0^-)$ and K_d, PAR at any depth can then be

estimated. However γ, ν, ϕ_m, PAR_ϕ and $\overline{a_\phi}^*$ must be estimated for the calculation of

PP. γ varies from 0.3 to 0.9, with an average of 0.75 [Morel and Berton 1989, Balch

et al. 1992], the value used for our calculation. ϕ_m, ν and PAR_ϕ vary with

phytoplankton physiological status, which at this point cannot be derived based upon

remotely sensed measurements and must be estimated from other information. ϕ_m has

been reported to range from 0.03 mol C (Ein absorbed)$^{-1}$ to 0.1 mol C

(Ein absorbed)$^{-1}$ [Bannister and Weidemann 1984, Smith et al. 1989, Morel 1991]. As

a kind of average for productive waters, ϕ_m is assumed to equal 0.074 mol C

(Ein absorbed)$^{-1}$, a value suggested by Cullen [1990]. There is little literature

information, however, about the values of ν and PAR_ϕ. Platt et al. [1980] found ν

varied from 0 to 0.0028 (W/m^2)$^{-1}$. If we choose 0.0028 (W/m^2)$^{-1}$ for ν, its equivalent

value is $\nu \approx 0.01$ (Ein/m^2/day)$^{-1}$. Kiefer and Mitchell [1983] found that PAR_ϕ equals

about 10 Ein/m^2/day, a value assumed for the waters in this study.

The only unknown remaining is $\overline{a_\phi}^*$. This value varies with phytoplankton

condition ($a_\phi^*(\lambda)$) and the light environment [Morel 1978, Kishino et al. 1986]. If

only remote-sensing information is available, $\overline{a_\phi}^*$ must be estimated from other data,

or an empirical value has to be picked for $\overline{a_\phi}^*$. In many studies, an $\overline{a_\phi}^*$ value of

0.015 (mg chl a/m^2)$^{-1}$ has been used [Bannister 1974, Dubinsky et al. 1984, Smith et

al. 1989 and Marra et al. 1992] and assumed to be vertically constant.

Using the CZCS algorithm, [C] is found to be accurate to about a factor of 2

[Gordon and Morel 1983], and $a_\phi^*(440)$ can vary by a factor of 4 [Morel and Bricaud

1981, Bricaud et al. 1988, Laws et al. 1990, Stramski and Morel 1990, Carder et al.

1991] due to pigment composition, "package effects," and the color of the light field.

That means the combined variation of $[C]$ and $\overline{a_\phi}^*$ for AP could be off on a global

scale by a factor of 8 when other terms are known, although the range of uncertainty

is probably significantly less than 8 here as we are not in subtropical waters (e.g. see

Laws et al. 1990).

Eq. 63 is actually a simplified version of a complete spectral expression as

noted by Sathyendranath et al. [1989b], Morel [1991] and Platt et al. [1991]; i.e.

$$PP(z) = \phi(z) \int_{400}^{700} a_\phi(\lambda) E_o^q(z,\lambda) d\lambda \ , \tag{72}$$

and the absorbed photons are

$$AP(z) = \int_{400}^{700} a_\phi(\lambda) E_o^q(z,\lambda) d\lambda \ . \tag{73}$$

However, those full spectral models were based on the pigment or chlorophyll a

concentration, similar to Eq. 63. If $a_\phi(\lambda)$ and $a(\lambda)$ can be obtained directly and

analytically from remotely measured signals (e.g. remote-sensing reflectance), instead

of using the pigment concentration based model and the empirical relationships to

obtain $[C]$ and the attenuation coefficient for $AP(z)$, the problems involved in the

estimation of $[C]$ and choosing values for γ and $\overline{a_\phi}^*$ will be avoided, and the accuracy

of estimating AP and PP would be improved when $E_o^q(0^-)$, ϕ_m, ν and PAR_ϕ are

certain.

From the discussions in Chapters 6 and 7, we know $a_\phi(\lambda)$ and $a(\lambda)$ can be

derived solely from measured $R_{rs}(\lambda)$. Thus, scalar irradiance at depth z can be

calculated through Eq. 66 with $K_d \approx 1.08\, D_d(0)\, a$ [Gordon 1989a]. $E_o^q(0^-)$ can be determined from models of Gregg and Carder [1990] or Bishop and Rossow [1991]. Therefore, when ϕ_m, PAR_ϕ and ν are known, PP for any depth can be calculated through Eqs. 68 and 73.

For data collected from the Marine Light-Mixed Layer (ML-ML) study (21°W/59°N) of May 1991 (PAR and primary production measurements are in Marra et al. [1994]), two sets of calculations were made. One set is derived using Eqs. 68 and 69 (referred to as the "pigment" method hereafter), as discussed at the beginning of this section. The other set is derived by Eqs. 68 and 73 (referred to as the "absorption" method hereafter), where the absorption coefficients of the pigments and the total absorption coefficients are analytically derived from measured remote-sensing reflectance.

In both calculations, measured $PAR(0)$ for each station was used for the calculation of $PAR(z)$ and comparisons of the two methods, because most of the stations were taken during cloudy weather. $D_d(0)$ is approximated as 1.2 [Platt et al. 1991] in the "absorption" method as most of the stations were under clouds. The calculated results for each day at each depth were compared with the measured primary production values, and the water-column-integral production.

Comparisons of calculated to measured PAR and calculated to measured PP are presented in Figures 23a - 23d and Figures 24a - 24d, respectively. All data are summarized in Table 7 and all PP data in Figure 25.

It can be seen that the "absorption" method yields close estimates of $PAR(z)$,

while $PAR(z)$ values calculated by the "pigment" method were consistently higher, particularly at depth. One reason for this is that the CZCS pigment algorithm estimated [chl a] as much as a factor of 5 lower than the measured surface values for these waters. This had the consequence that K_d values calculated from these [C] ([chl a]/0.75) were small. This difference could be the result of an incorrect CZCS algorithm for that environment [e.g. Balch et al. 1989, Mitchell and Holm-Hansen 1991], or less likely there were substantial errors or discrepancies in the measurements of R_{rs} or "sea truth" [chl a]. Additionally, the empirical relationship between K_d and [C] (Eq. 71) might not hold for these waters. The same field data, however, are used for both methods; so models and algorithms will be largely responsible for differences between the methods.

Primary production values calculated using the "absorption" method were highly comparable to the measured values, whereas the "pigment" method significantly underestimated PP, particularly in the surface waters. The average difference of the water-column-integrated PP is 20% between the measured and the "absorption" method, while it is 61% between the measured and the "pigment" method (Table 7). The r^2 is 0.95 (n=24) for a linear regression between the values calculated by the "absorption" method and that of the measurements, with a slope of 1.26 and + 32% difference; whereas the r^2 is 0.85 (n=24) between the values calculated by the "pigment" method and that of the measurements, with a slope of 0.34 and - 78% difference (see Figure 25). These results indicate that there is a factor of 3
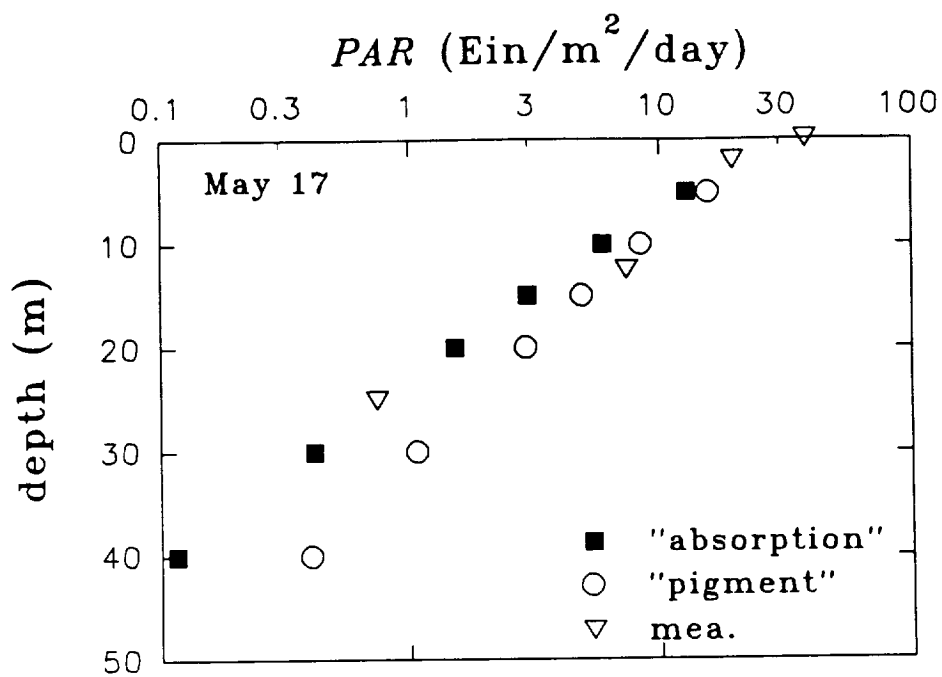
PAR (Ein/m^2/day)

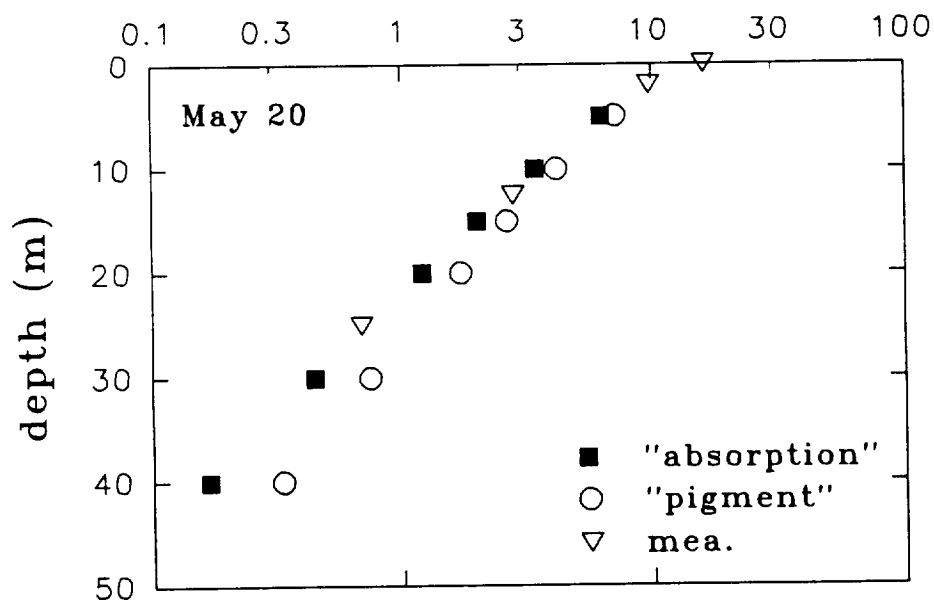Figure 23a. Measured vs. Modeled *PAR* of May 17 in ML-ML.

Figure 23b. Measured vs. Modeled *PAR* of May 20 in ML-ML.
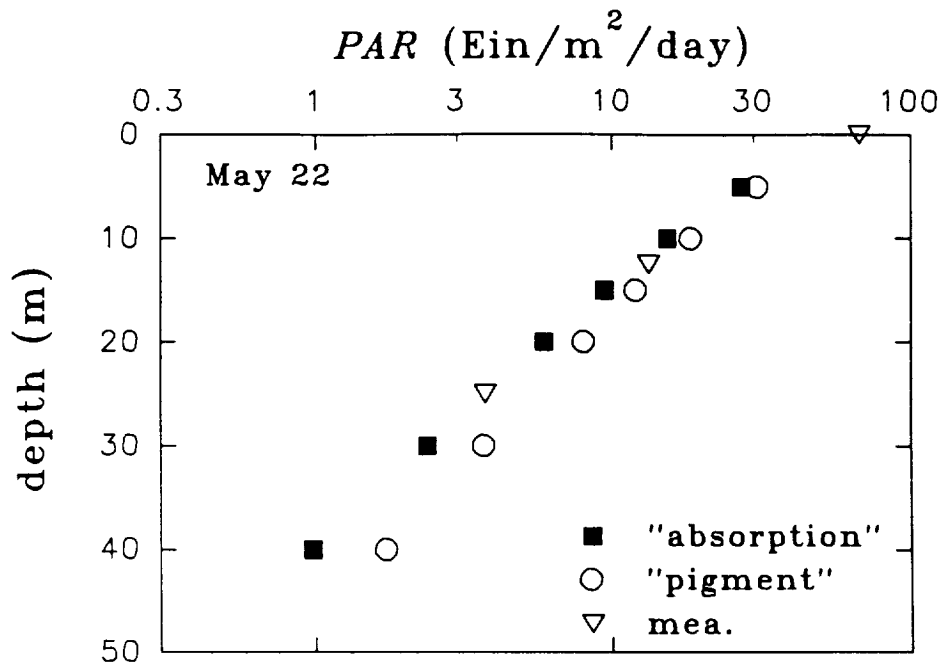
Figure 23c. Measured vs. Modeled *PAR* of May 22 in ML-ML.

Figure 23d. Measured vs. Modeled *PAR* of May 24 in ML-ML.

Table 7. Results about *PP* Calculation of ML-ML, May 1991.

Day	May 17	May 20	May 22	May 24
$PAR(0)$ (Ein/m^2/day)	38.27	16.25	65.72	28.73
$R_{rs}(443)/R_{rs}(550)$	1.2	1.6	1.8	1.8
surface [chl *a*] (mg/m^3)	2.9	1.3	1.5	1.0
CZCS [chl *a*] (mg/m^3)	0.67	0.43	0.36	0.34
Mea. integral *PP* (m mol C/m^2/day)	190	98	89	99
Est. integral *PP*: "absorption" (m mol C/m^2/day)	235	94	105	89
Est. integral *PP*: "pigment" (m mol C/m^2/day)	77	34	62	40

improvement in the accuracy of *PP* calculation from remote sensing for ML-ML waters using the "absorption" method.

For May 17, the calculated *PP* values by the "absorption" method in the euphotic zone were generally greater than the measured values. Factors that can account for these differences include possible errors in measurement and R_{rs} inversion, grazing effects on the measured values, and either the photoinhibition factor used was smaller than the "real" situation, or ϕ_m and PAR_ϕ used were higher than the "actual" values.

For May 20 and May 24, the *PP* values calculated by the "absorption" method were very close to those measured, which suggests that our assumed values of ϕ_m, PAR_ϕ and ν for these two days were close to the realistic situation.

The greatest differences between measured and calculated values from both the

PP (umol C/l/day)
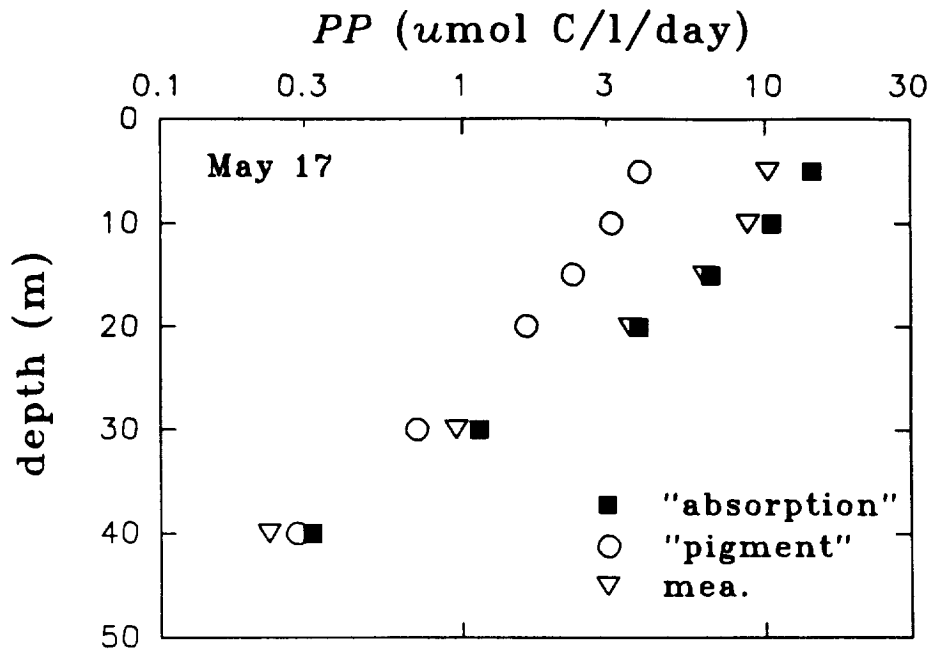
Figure 24a. Measured vs. Modeled *PP* of May 17 in ML-ML.
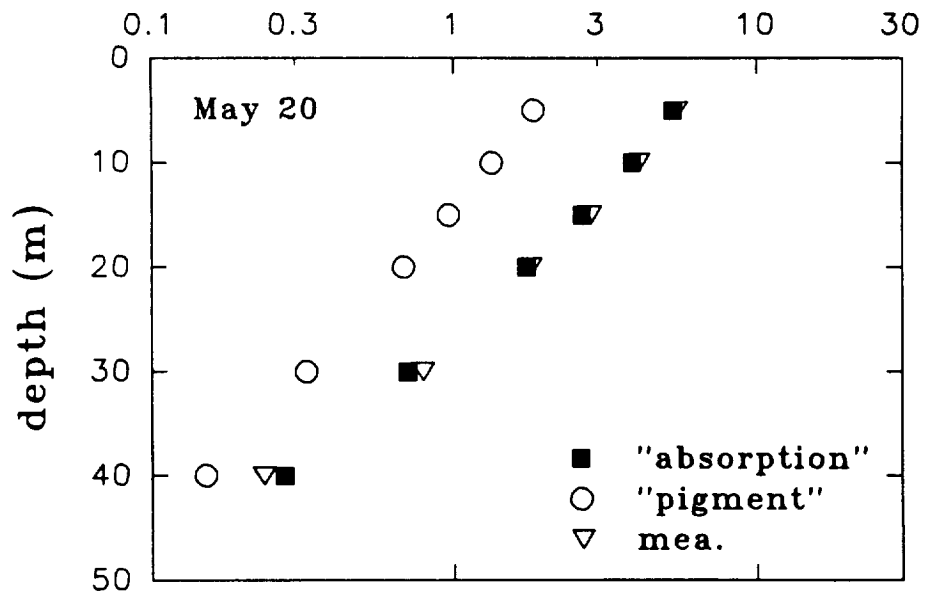
Figure 24b. Measured vs. Modeled *PP* of May 20 in ML-ML.

PP (umol C/l/day)

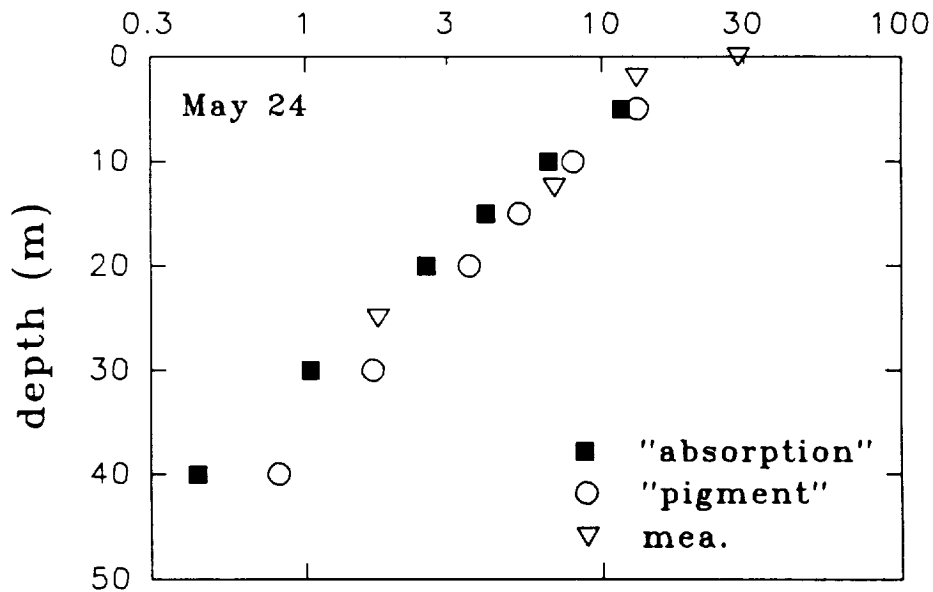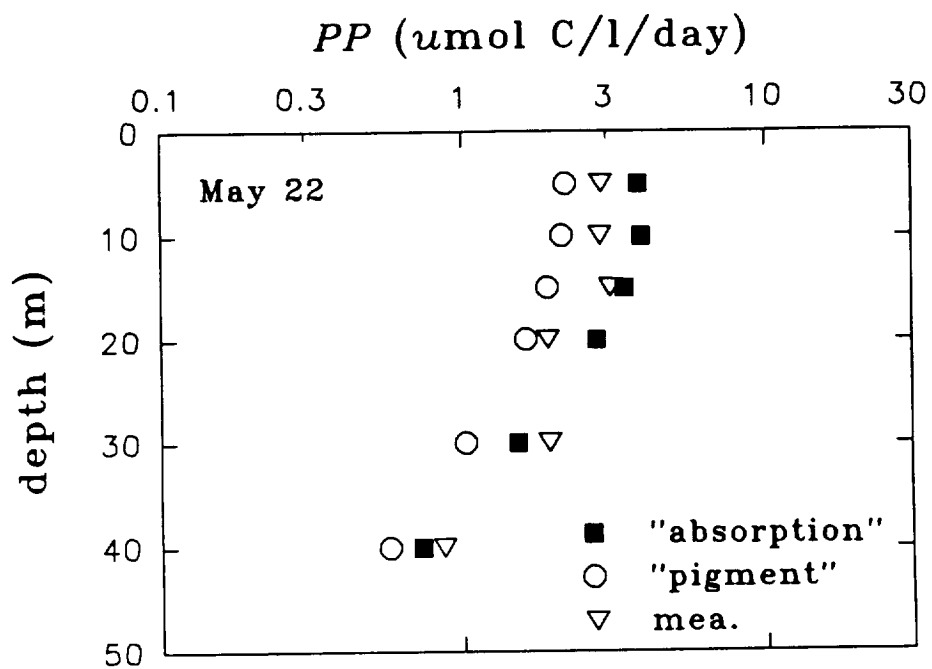Figure 24c. Measured vs. Modeled PP of May 22 in ML-ML.
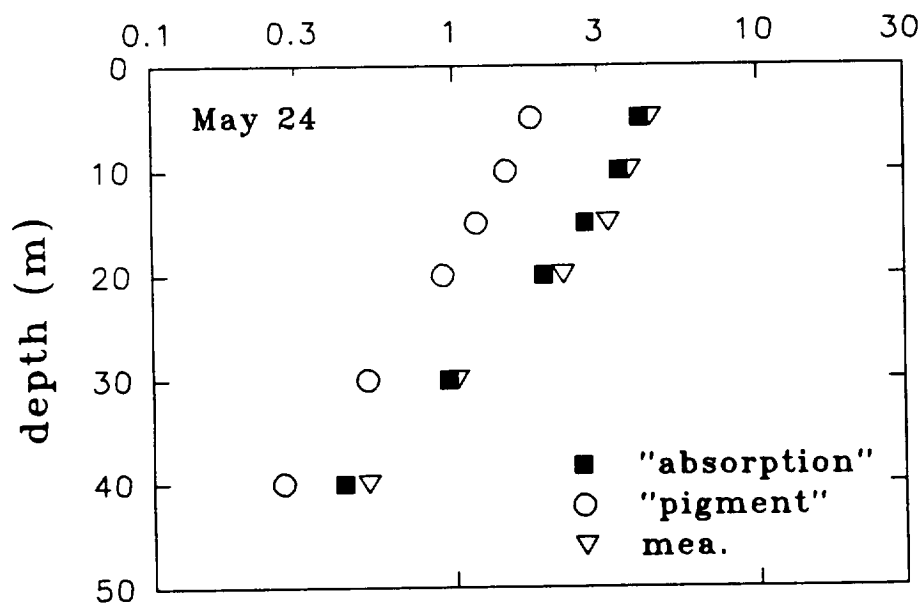
Figure 24d. Measured vs. Modeled PP of May 24 in ML-ML.
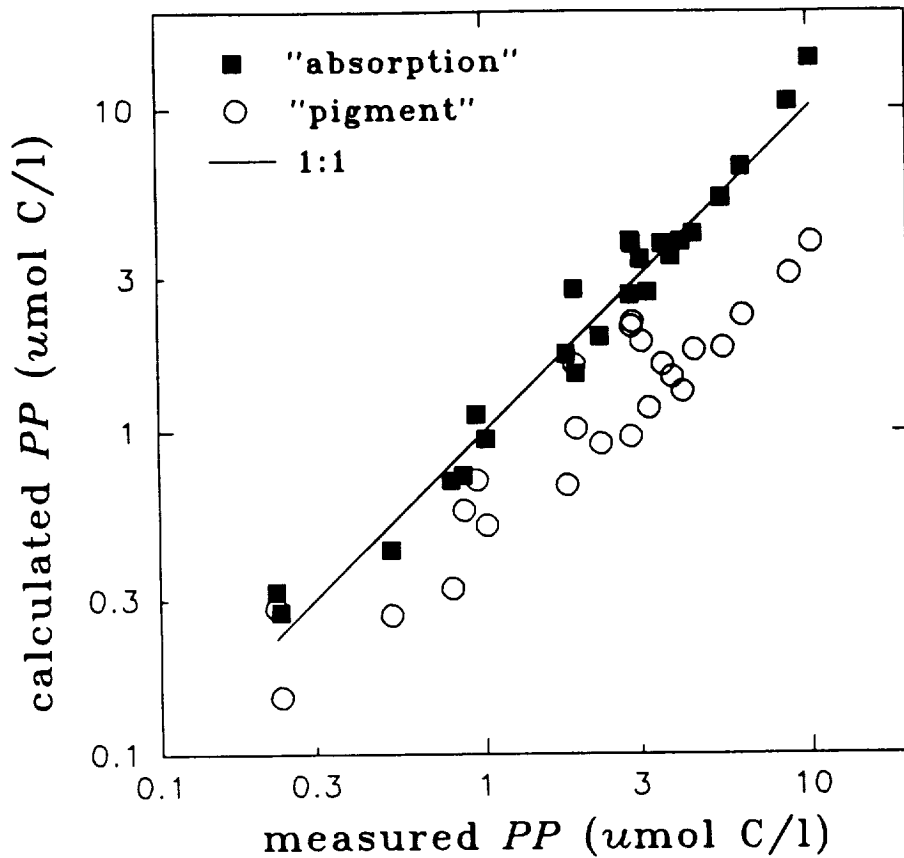
Figure 25. Measured vs. Modeled *PP* of ML-ML, May 1991.

"pigment" and "absorption" methods occurred on the only sunny day of the cruise, May 22, where measured surface layer production was smaller than in the second layer. Other than measurement errors, this is an indication of increased photoinhibition, as suggested by the calculated values of the "absorption" method. The calculated *PP* values by the "absorption" method, however, are greater than the measured values for the first four depths ($\sim 40\%$). Possible reasons for this difference might be an overestimation of ϕ_m or an underestimation of ν for the phytoplankton in

this environment, since ϕ_m and ν might be a function of light history. The other 3 cruise days were overcast with an expected adaptation of the plants to a low light environment. The sudden exposure to the bright light probably caused extreme photoinhibition in the dark-adapted phytoplankton population with the resultant overestimation of PP by the "absorption" method.

The PP values calculated by the "pigment" method for the sunny day, however, do not show a photoinhibition response in the surface waters (Figure 24c). One reason for this is that $\overline{a}_\phi{}^*$ not only varies with the chlorophyll-specific absorption coefficient, but it also varies with the light field (Eq. 64). An $\overline{a}_\phi{}^*$ value for surface water is not necessarily appropriate for the whole water column, even for well-mixed oceans [Kishino et al. 1986]. So, the $\overline{a}_\phi{}^*$ value is one of the major sources of error in PP calculations by the traditional method.

For the waters studied, PP values calculated by the "pigment" method were significantly lower than the measured rates. Since PP values calculated by the "absorption" method were close to measured values, our value of ϕ_m, 0.074 mol C (Ein absorbed)$^{-1}$, is apparently close to the actual value. Therefore, the differences between the "pigment" method calculated and measured PP are largely due to the estimation of $[C]$ and the product of $\gamma[C]\overline{a}_\phi{}^*$. However, when only remote-sensing data are available, it is difficult to know which are the "correct" $\overline{a}_\phi{}^*$ and $\gamma[C]$ values, as they depend upon empirical parameters. What makes things interesting is that a factor of 2 increase in both $[C]$ and $\overline{a}_\phi{}^*$ will make calculated PAR and PP both close to the measured values. Table 7 pigment data, however, suggest that the CZCS

algorithm accounts for most of the error. This is consistent with the speculation of

Platt et al. [1988] that determination of biomass by remote sensing dominates the

error in primary production estimation.

Comparing Eqs. 69 and 73, the main difference between the "absorption" and

"pigment" methods is how $AP(z)$, the absorbed energy by phytoplankton pigments, is

obtained from remote-sensing data. In the traditional method, calculation of AP

depends heavily on 4 parameters: γ, A_1, A_2, and $\overline{a_\phi^*}$. When only remote-sensing

signals exist, it is difficult to verify which values should be used for each of these

parameters, although each of them could be tuned empirically to specific regions and

specific seasons [Platt et al. 1991]. Since there are errors associated with each

number, the cumulative error in AP could then be very high even if PAR is correct.

In the AP calculation by the "absorption" method, however, the phytoplankton

absorption and the total absorption are analytically derived from measured R_{rs}. Thus,

most of the error comes from the R_{rs}-inversion process. It is believed that absorption

coefficients derived from R_{rs} inversion have an accuracy better than 50% for "case 1"

and "case 2" waters (Chapter 7). This means that the accuracy in the AP calculation

by the "absorption" method could be within 50% compared to the errors as great as

400% derived using the traditional method. In this "absorption" method suggested

here, the mid-step, i.e. deriving [chl a] and estimating a value for $\overline{a_\phi^*}$, is eliminated.

The result is highly improved accuracy in deriving AP and PP. The remaining

challenge for the calculation of PP through remote sensing is how to remotely obtain

accurate estimation of the physiological parameters [Balch et al. 1992] such as ϕ_m,

PAR_ϕ and ν, that could perhaps be based on light history, chlorophyll fluorescence efficiency [Chamberlin et al. 1990], and surface temperature anomalies [Kamykowski and Zentara 1986].

In conclusion of this section:

a) Based on the results presented here, the a_ϕ simulation works very well in modeling $PAR(z)$ from $PAR(0)$ and measured R_{rs}. Combined with parameters regarding photosynthesis, the PP values calculated by the "absorption" method were close to the measured ones with $r^2 = 0.95$ and slope $= 1.26$; which is a factor of 3 improvement in PP estimation accuracy over the traditional method. These results also indicate that the combined PP model,

$$PP(z) = AP(z) \frac{\phi_m PAR_\phi}{PAR_\phi + PAR(z)} e^{-\nu PAR(z)}, \tag{74}$$

works well for the ML-ML waters.

b) It is not necessary to know [chl a] and $\overline{a_\phi}^*$ for the calculation of PP. In the traditional method, the estimation of [chl a] (or [C]) and $\overline{a_\phi}^*$ separately is an inherent disadvantage in calculating PP based upon satellite or aircraft remote sensing of ocean color. From the remote-sensing point of view with regard to remote estimation of PP, what is really needed is the absorbed energy by phytoplankton and the physiological parameters regarding the photosynthesis by phytoplankton. So, it is preferable to shift the primary production model from the pigment-concentration based to the pigment-absorption based.

8.7 Modeling Total Radiance (L_t) Measured from a Low-flying Aircraft (Blimp Shamu)

In January 1993, the total radiance, L_t, of Tampa Bay was measured from the SeaWorld blimp "Shamu". These L_t measurements covered waters over sandy and grassy bottoms and dark, gelbstoff-rich waters. Although values of E_d were measured before and after the flight, no E_d or proper L_{sky} data could be collected when L_t was measured, so no precise R_{rs} could be derived using standard methods. However, L_{sky} from part of the sky was measured, and its spectral shape might be considered approximately correct. Then, with the method discussed in Chapter 7, the parameters r and Δ were used to estimate the sky radiance which enters the sensor. Thus the measured L_t could be modeled, and the in-water absorption coefficient and the water depth for optically shallow water could be derived.

The total radiance entering a sensor in clear air is [Gordon and Wang 1994]

$$L_t = L_u(0^+)e^{-(\tau_A + \tau_G)} + L_R + L_A \, , \tag{75}$$

where L_R is the contribution due to Rayleigh scattering in the atmosphere, L_A is the contribution due to aerosol scattering, and $\exp(-\tau_A - \tau_G)$ determines the attenuation of atmosphere to the upwelling radiance.

Since the altitude of the blimp was only about 50 m over the water surface, $\exp(-\tau_A - \tau_G)$ is ≈ 1 and the small contributions due to L_R and L_A are combined into rL_{sky} and ΔE_d of Eq. 40, so

Figure 26a. Measured vs. Modeled L_t of Station SH04.
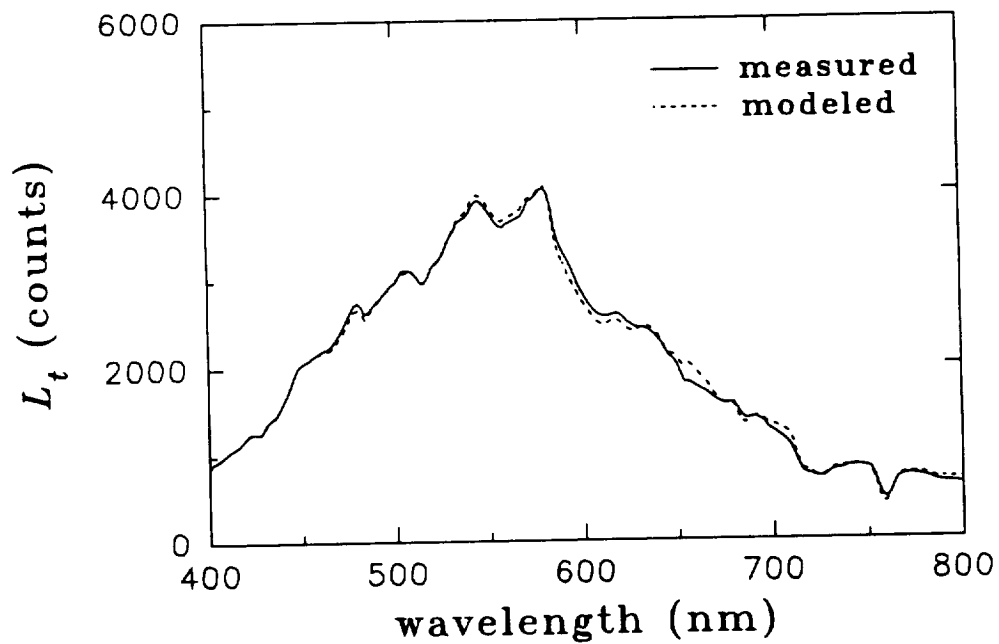
Figure 26b. Measured vs. Modeled L_t of Station SH34.
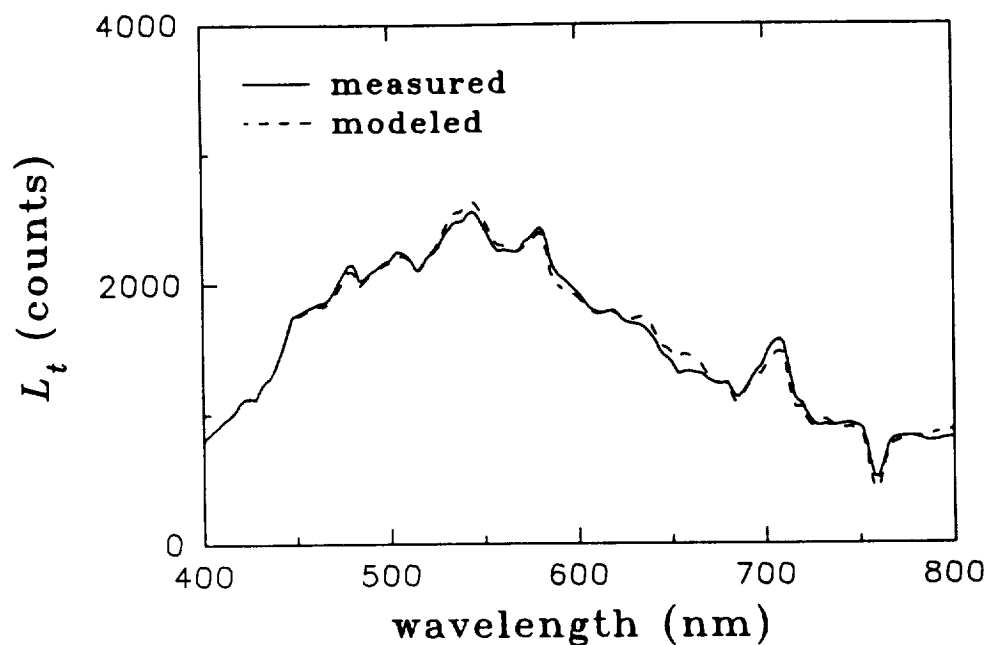
Figure 26c. Measured vs. Modeled L_t of Station SH35.

$$L_t \approx (R_{rs} + \Delta) \frac{\pi L_G}{R_G} + r L_{sky} \ . \tag{76}$$

L_G was estimated by interpolation between the pre- and post-flight measurements of L_G. With the a_ϕ simulation discussed in section 6.2, L_t of waters over sandy bottoms (SH04), grassy bottoms (SH35), and dark waters (SH34) were modeled. Since R_{rs} and L_t are interchangeable when other terms are certain, R_{rs} curves of above situations were also modeled at the same time.

Figures 26a - 26c show the measured and modeled L_t, while Figures 27a - 27c show the measured and modeled R_{rs}. It can be seen that excellent model results were achieved for these waters. The bottom albedo of the sandy bottoms came
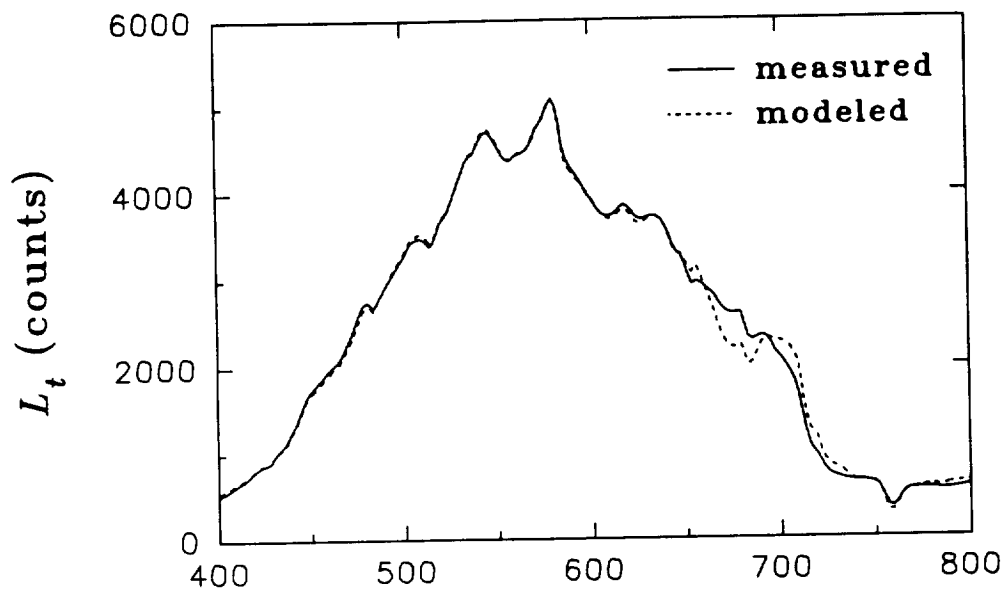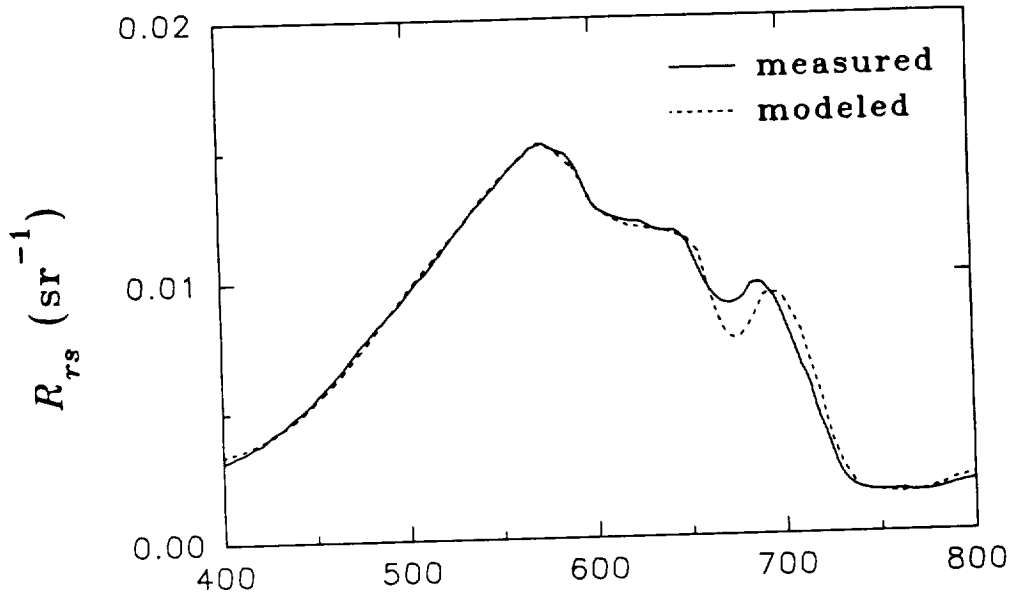
Figure 27a. Measured vs. Modeled R_{rs} of Station SH04.
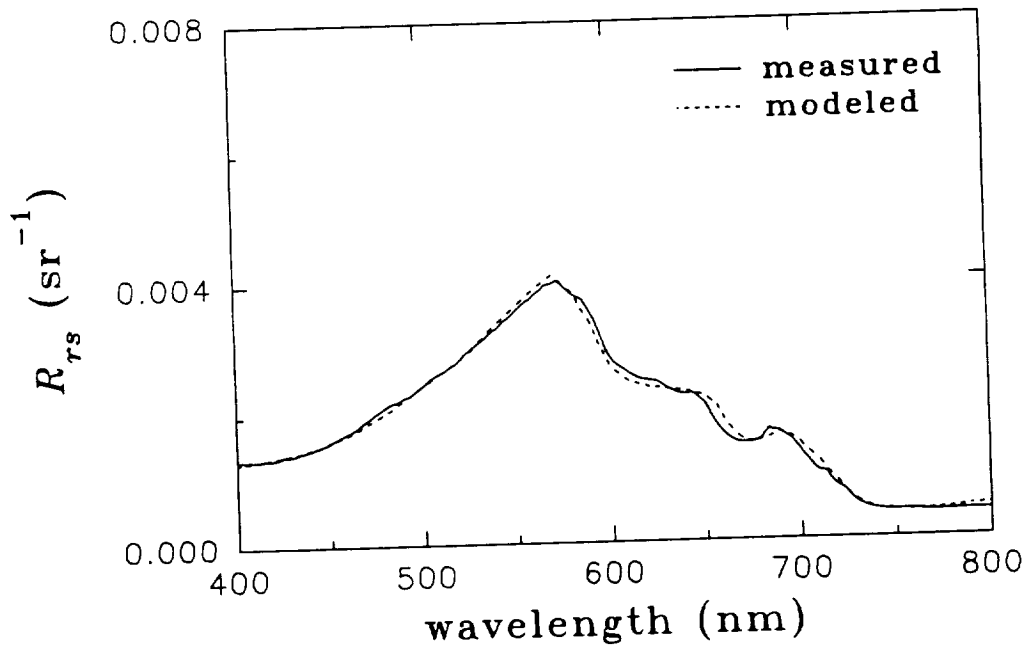
Figure 27b. Measured vs. Modeled R_{rs} of Station SH34.
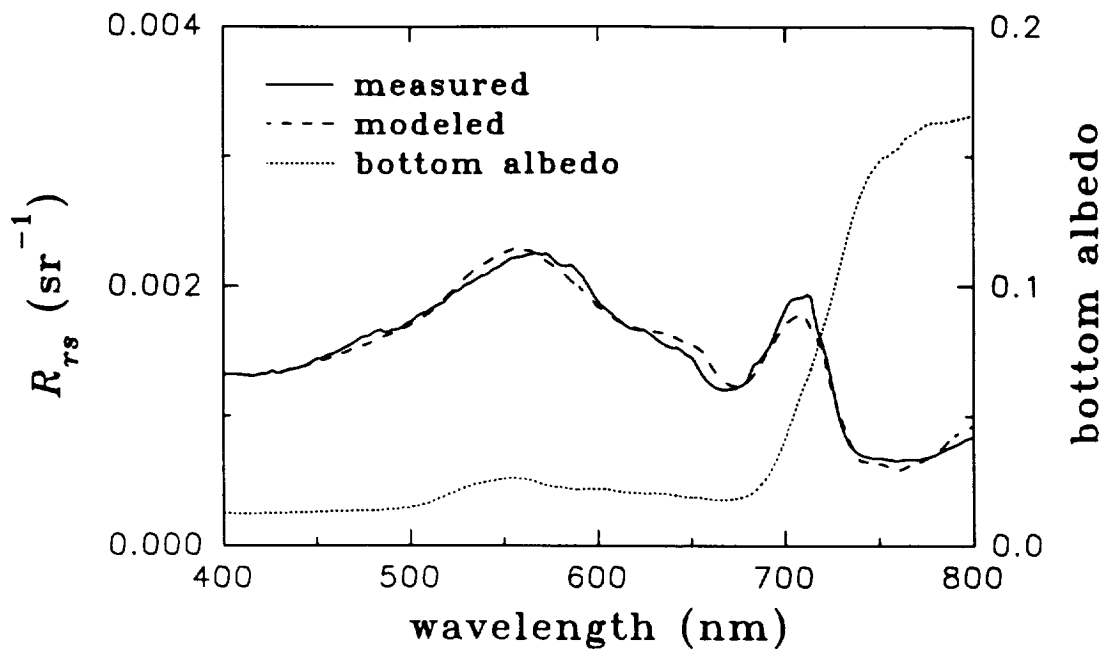
Figure 27c. Measured vs. Modeled R_{rs} of Station SH35.

from Figure 10, while the bottom albedo of the grassy bottoms came from reflectance of vegetation [Tucker and Miller 1977].

CHAPTER 9

CONCLUSIONS OF PART B

9.1 The phytoplankton absorption coefficient, $a_\phi(\lambda)$, can be simulated using the following expressions:

1) mathematical functions:

$$400 \leq \lambda \leq 570, \quad a_\phi(\lambda) = a_{\phi 1} e^{-F\left(\ln\frac{\lambda - \lambda_1}{100}\right)^2}, \qquad (77)$$

$$570 < \lambda < 656, \quad a_\phi(\lambda) = a_\phi(570) + \frac{a_\phi(656) - a_\phi(570)}{656 - 570}(\lambda - 570), \qquad (78)$$

and

$$656 \leq \lambda \leq 700, \quad a_\phi(\lambda) = a_{\phi 2} e^{-\frac{(\lambda - \lambda_2)^2}{2\sigma_2^2}}. \qquad (79)$$

2) empirical relationships:

$$a_\phi(\lambda) = [a_0(\lambda) + a_1(\lambda)\ln(a_\phi(440))]a_\phi(440). \qquad (80)$$

The mathematical expression involves 6 parameters, but only 4 of them $(a_{\phi 1}, F, a_{\phi 2}$ and $\sigma_2)$ vary significantly among different waters. 3 of the 4 parameters, F, σ_2 and $a_{\phi 2}/a_{\phi 1}$ could be estimated from the value of $a_{\phi 1}$ through

$$a_{\phi 2}/a_{\phi 1} = 0.86 + 0.16\ln(a_{\phi 1}),$$

$F = 2.89\exp[-0.505\tanh[0.56\ln(a_{\phi l}/0.043)]]$,

$\sigma_2 = 14.17 + 0.9\ln(a_{\phi l})$.

$a_0(\lambda)$ and $a_1(\lambda)$ of Eq. 80 for each wavelength were empirically derived (Table 6). So, using either method, $a_\phi(\lambda)$ curve can be simulated when $a_\phi(440)$ is known. Comparing the two methods, mathematical functions create a smooth a_ϕ curve, but with more potential to adjust the curve shape. The empirical relationships, however, provide empirical spectral finesse to the a_ϕ curves.

9.2   With the above $a_\phi(\lambda)$ expressions, the inverse problem of R_{rs} can be reasonably well solved. For waters of Monterey Bay and the Gulf of Mexico, the R_{rs}-derived total absorption coefficients at 440 nm, 486 nm and 550 nm were consistent with the values derived from K_d. When using the mathematical simulation, the average difference is 31% for $a(440)$, 21% for $a(486)$ and 25% for $a(550)$ for $a(440)$ ranged from 0.03 m^{-1} to 2.5 m^{-1}. These results were also consistent with the values derived using measured a_p curves. These results demonstrate that the $a_\phi(\lambda)$ simulations can be used in remote-sensing applications without prior knowledge of the in-water optical properties, such as chlorophyll-specific absorption coefficient.

9.3   The ranges for the 5 variables ($a_{\phi l}$, $a_{dg}(440)$, S_{dg}, X, and Y) are close to realistic situations.

9.4   With the $a_\phi(\lambda)$ simulation, the estimation of primary production in the euphotic zone can be carried out just from measured R_{rs} and surface PAR. The problems associated with the traditional method, i.e. estimating [chl a] and using a chlorophyll-specific absorption coefficient, are avoided. For data collected in the ML-

ML May 1991 waters, r^2 is 0.95 between the calculated and measured *PP* values, with a slope of 1.26 and 32% average error. This is a factor of 3 improvement in the accuracy of *PP* estimation by using the suggested method over the traditional method for those waters. However, challenges remain to remotely estimate the physiological parameters since they might be functions of nutrient stress, life stage, light history, etc.

CHAPTER 10

SUMMARY AND FUTURE WORK

10.1 Summary

a. A remote-sensing reflectance (R_{rs}) model is developed, including terms for the contributions of bottom reflectance, gelbstoff fluorescence, and water Raman scattering.

b. The remote-sensing reflectance model is tested for a wide range of water types, and an average error of 3.4% is obtained between the measured and modeled remote-sensing reflectance curves. This result indicates that the forward problem, to interpret the water color or remote-sensing reflectance in terms of in-water constituents, is well solved.

c. A six parameter model is developed to simulate the spectral absorption coefficient of phytoplankton pigments $(a_\phi(\lambda))$ with an average error of about 11%. It can be used in the remote-sensing reflectance modeling and inversion.

d. Using the $a_\phi(\lambda)$ model and the R_{rs}-inversion methodology developed above, in-water absorption and scattering coefficients can be analytically derived solely from the remotely measured signals. For $a(440)$ ranging from 0.03 to 2.5 m^{-1}, the remote-sensing-derived $a(440)$ values are within 31% of the in-water measured values. This

indicates that the inverse problem, to analytically derive in-water optical components from remotely measured signals alone, is reasonably well solved.

e. A new approach is suggested for the estimation of primary production based on remote-sensing measurements. In this new approach, the primary production model is based on the phytoplankton pigment absorption coefficient, instead of the phytoplankton pigment concentration.

f. Using the new approach for a study in the North Atlantic during May 1991, the estimated primary production at depth in the euphotic zone based on remote sensing was within 32% of the measured values. This result is about a factor of 3 improvement in the estimation accuracy over a traditional method, which is based on the pigment concentration.

10.2 Future Work

a. Validation for values of X and Y is not complete, which requires independent in-water measurements of the values and distributions of the spectral volume scattering function and radiance field. Hopefully, this will be solved in the coming years with the development of new, sophisticated instrumentation.

b. Further coupled in-water and remote-sensing measurements for a wide range of waters are necessary in order to improve and expand the usefulness of the model and simulations suggested in this study.

c. Part of the errors in the component derivation come from the internal compensations among the parameters. In order to improve the accuracy of derived in-water components from remotely sensed signals alone, theoretical and experimental studies about the parameters need be carried out. For example, how great is the compensation among the parameters? What should be the right ranges for Y and S_{d_g}? How to determine their ranges? etc.

d. Methods to accurately derive $a(\lambda)$ from $K_d(\lambda)$ need further study.

e. Coupled investigations between primary production and remote-sensing reflectance measurements need to be carried out widely to generate more data to test and improve the suggested new approach.

f. For the remote estimation of primary production, methods must be pursued to remotely or empirically estimate changes of the physiological parameters, perhaps by their co-variance with some remotely measured variables such as sea-surface-temperature anomalies, wind-stress history, and light history, etc.

REFERENCES CITED

Austin, R. W. 1974. Inherent spectral radiance signatures of the ocean surface. *Ocean Color Analysis. SIO Ref.* 7410.

Austin, R. W. 1979. Coastal zone color scanner radiometry. *Ocean Optics VI, Proc. SPIE.* 208:170-77.

Austin, R. W., and T. J. Petzold. 1981. The determination of the diffuse attenuation coefficient of sea water using the coastal zone color scanner. In *Oceanography from space*, ed. J. F. R. Gower, 239-56. New York: Plenum Press.

Balch, W. M., R. W. Epply, M. R. Abbott, and F. M. H. Reid. 1989. Bias in satellite-derived pigment measurements due to coccolithophores and dinoflagellates. *J. Plankton Res.* 11:575-81.

Balch, W. M., R. Evans, J. Brown, G. Feldman, C. McClain, and W. Esaias. 1992. The remote sensing of ocean primary productivity: use of a new data compilation to test satellite algorithms. *J. Geophys. Res.* 97:2279-293.

Bannister, T. T. 1974. Production equations in terms of chlorophyll concentration, quantum yield, and upper limit to production. *Limnol. Oceanogr.* 19:1-12.

Bannister, T. T. 1979. Quantitative description of steady state, nutrient-saturated algal growth, including adaptation. *Limnol. Oceanogr.* 24:76-96.

Bannister, T. T., and A. D. Weidemann. 1984. The maximum quantum yield of phytoplankton photosynthesis *in situ*. *J. Plankton. Res.* 6:275-94.

Bidigare, R. R., M. E. Ondrusek, J. H. Morrow, and D. A. Kiefer. 1990. In vivo absorption properties of algal pigments. *Ocean Optics X, Proc. SPIE.* 1302:290-302.

Bidigare, R. R., B. B. Prezelin, and R. C. Smith. 1992. Bio-optical models and the problems of scaling. In *Primary production and biogeochemical cycles in the sea*, ed. P. G. Falkowski and A. D. Woodhead, 1175-212. New York: Plenum Press.

Bishop, J. K., and W. B. Rossow. 1991. Spatial and temporal variability of global surface solar irradiance. *J. Geophys. Res.* 96:16,839-16,858.

Bricaud, A., A. Morel, and L. Prieur. 1981. Absorption by dissolved organic matter of the sea (yellow substance) in the UV and visible domains. *Limnol. Oceanogr.* 26:43-53.

Bricaud, A., and A. Morel. 1986. Light attenuation and scattering by phytoplanktonic cells: a theoretical modeling. *Appl. Opt.* 25:571-80.

Bricaud, A., A. L. Bedhomme and A. Morel. 1988. Optical properties of diverse phytoplanktonic species: experimental results and theoretical interpretation. *J. Plankton Res.* 10:851-73.

Bricaud, A., and D. Stramski. 1990. Spectral absorption coefficients of living phytoplankton and nonalgal biogenous matter: A comparison between the Peru upwelling area and the Sargasso Sea. *Limnol. Oceanogr.* 35:562-82.

Carder, K. L., and R. G. Steward. 1985. A remote-sensing reflectance model of a red tide dinoflagellate off West Florida. *Limnol. Oceanogr.* 30:286-98.

Carder, K. L., R. G. Steward, J. H. Paul and G. A. Vargo. 1986. Relationships between chlorophyll and ocean color constituents as they affect remote-sensing reflectance models. *Limnol. Oceanogr.* 31:403-13.

Carder, K. L., R. G. Steward, G. R. Harvey, and P. B. Ortner. 1989. Marine humic and fulvic acids: their effects on remote sensing of ocean chlorophyll. *Limnol. Oceanogr.* 34:68-81.

Carder, K. L., W. W. Gregg, D. K. Costello, K. Haddad, and J. M. Prospero. 1991. Determination of Saharan dust radiance and chlorophyll from CZCS imagery. *J. Geophys. Res.* 96:5369-378.

Carder, K. L., S. K. Hawes, K. A. Baker, R. C. Smith, R. G. Steward, and B. G. Mitchell. 1991. Reflectance model for quantifying chlorophyll a in the presence of productivity degradation products. *J. Geophys. Res.* 96:20,599-20,611.

Carder, K. L., Z. P. Lee, T. G. Peacock, R. G. Steward, and C. O. Davis. 1992. Aircraft algorithms for water absorption coefficients: rain or shine. *EOS* 73, April.

Carder, K. L., P. Reinersman, R. F. Chen, F. Muller-Karger, C. O. Davis, and

M. Hamilton. 1993. AVIRIS calibration and application in coastal oceanic environments. *Remote Sens. Environ.* 44:205-16.

Carder, K. L., S. K. Hawes, and Z. P. Lee. 1994. SeaWiFS algorithm for chlorophyll *a* and colored dissolved organic matter in a subtropical environment. *SeaWiFS working group report.*

Chamberlin, W. S., C. R. Booth, D. A. Kiefer, J. H. Morrow, and R. C. Murphy. 1990. Evidence for a simple relationship between natural fluorescence, photosynthesis and chlorophyll in the sea. *Deep-Sea Res.* 37:951-973.

Clark, D. K. 1981. Phytoplankton algorithm for the Nimbus-7 CZCS. In *Oceanography from space.* ed. J. R. F. Gower, 227-38. New York: Plenum Press.

Clark, R. K., T. H. Fay, and C. L. Walker. 1987. Bathymetry calculations with Landsat 4 TM imagery under a generalized ratio assumption. *Appl. Opt.* 26: 4036-4038.

Cleveland, J. S., M. J. Perry, D. A. Kiefer, and M. C. Talbot. 1989. Maximal quantum yield of photosynthesis in the northwestern Sargasso Sea. *J. Marine Res.* 47:869-86.

Cleveland, J. S., and A. D. Weidemann. 1993. Quantifying absorption by aquatic particles: A multiple scattering correction for glass-fiber filters. *Limnol. Oceanogr.* 38:1321-327.

Coble, P. G., S. A. Green, N. V. Blough, and R. B. Gagosian. 1990. Characterization of dissolved organic matter in the Black Sea by fluorescence spectroscopy. *Science* 348:432-35.

Collins, D. J., J. A. Bell, R. Zanoni, I. S. McDermid, J. B. Breckinridge, and C. A. Sepulveda. 1984. Recent progress in the measurement of temperature and salinity by optical scattering. *Ocean Optics VII, Proc. SPIE* 489:247-69.

Cullen, J. J. 1990. On models of growth and photosynthesis in phytoplankton. *Deep-Sea Res.* 37:667-83.

Dubinsky, Z., T. Berman, and F. Schanz. 1984. Field experiments for *in situ* measurements of photosynthetic efficiency and quantum yield. *J. Plankton Res.* 6:339-49.

Gordon, H. R., and O. B. Brown. 1974. Influence of bottom depth and albedo on the diffuse reflectance of a flat homogeneous ocean. *Appl. Opt.* 13:2153-159.

Gordon, H. R., and W. R. Mcluney. 1975. Estimation of the depth of sunlight penetration in the sea for remote sensing. *Appl. Opt.* 14:413-16.

Gordon, H. R., O. B. Brown, and M. M. Jacobs. 1975. Computed relationship between the inherent and apparent optical properties of a flat homogeneous ocean. *Appl. Opt.* 14:417-27.

Gordon, H. R. 1979. Diffuse reflectance of the ocean: the theory of its augmentation by chl *a* fluorescence at 685nm. *Appl. Opt.* 18:1161-166.

Gordon, H. R., and D. K. Clark. 1980. Remote sensing optical properties of a stratified ocean: an improved interpretation. *Appl. Opt.* 19:3428-430.

Gordon, H. R., D. K. Clark, J. L. Mueller, and W. A. Hovis. 1980. Phytoplankton pigments from the Nimbus-7 coastal Zone Color Scanner: Comparisons with surface measurements. *Science* 210:63-66.

Gordon, H. R., R. C. Smith, and J. R. V. Zaneveld. 1980. Introduction to ocean optics. *Ocean Optics VI, Proc. SPIE.* 208:1-43.

Gordon, H. R., and A. Morel. 1983. *Remote assessment of ocean color for interpretation of satellite visible imagery: A review.* pp. 44. New York: Springer-Verlag.

Gordon, H. R., D. K. Clark, J. W. Brown, O. B. Brown, R. H. Evans, and W. W. Broenkow. 1983. Phytoplankton pigment concentrations in the Middle Atlantic Bight: Comparison of ship determinations and CZCS estimates. *Appl. Opt.* 22:20-36.

Gordon, H. R. 1985. Ship perturbation of irradiance measurements at sea, 1: Monte Carlo simulations. *Appl. Opt.* 24:4172-182.

Gordon, H. R. 1986. Ocean color remote sensing: Influence of the particle phase function and the solar zenith angle. *Eos Trans. AGU* 14:1055.

Gordon, H. R., O. B. Brown, R. H. Evans, J. W. Brown, R. C. Smith, K. S. Baker, and D. K. Clark. 1988. A semianalytic radiance model of ocean color. *J. Geophys. Res.* 93:10,909-10,924.

Gordon, H. R. 1989a. Can the Lambert-Beer law be applied to the diffuse attenuation coefficient of ocean water?. *Limnol. Oceanogr.* 34:1389-409.

Gordon, H. R. 1989b. Dependence of the diffuse reflectance of natural waters on the sun angle. *Limnol. Oceanogr.* 34:1484-489.

Gordon, H. R. 1994. Modeling and simulating radiative transfer in the ocean. In *Ocean optics*, ed. R. W. Spinrad, K. L. Carder and M. J. Perry, 3-39. New York: Oxford University.

Gordon, H. R. 1992. Diffuse reflectance of the ocean: influence of nonuniform phytoplankton pigment profile. *Appl. Opt.* 31:2116-2129.

Gordon, H. R., and M. Wang. 1994. Retrieval of water-leaving radiance and aerosol optical thickness over oceans with SeaWiFS: A preliminary algorithm. *Appl. Opt.* 33:443-452.

Gregg, W. W., and K. L. Carder. 1990. A simple spectral solar irradiance model for cloudless maritime atmospheres. *Limnol. Oceanogr.* 35:1657-675.

Hawes, S. K., K. L. Carder, and G. R. Harvey. 1992. Quantum fluorescence efficiencies of marine humic and fulvic acids: effects on ocean color and fluorometric detection. *Ocean Optics XI, Proc. SPIE.* 1750:212-23.

Hawes, S. K. 1992. Quantum fluorescence efficiencies of marine fulvic and humic acids. Master's Thesis. Dept. of Marine Science, University of South Florida.

Hoepffner, N., and S. Sathyendranath. 1991. Effect of pigment composition on absorption properties of phytoplankton. *Mar. Ecol. Prog. Ser.* 73:11-23.

Hoge, F. E., A. Vodacek, and N. V. Blough. 1993. Inherent optical properties of the ocean: Retrieval of the absorption coefficient of chromophoric dissolved organic matter from fluorescence measurements. *Limnol. Oceanogr.* 38:1394-402.

Hojerslev, N. K., and I. Trabjerg. 1990. A new perspective for remote measurements of plankton pigments and water quality. Report #51. Copenhagen.

Jeffrey, S. W. 1980. Algal pigment systems. In *Primary productivity in the sea*, ed. P. G. Falkowski, 33-58. Plenum.

Jerlov, N. G. 1976. *Marine Optics. Vol. 14 of Elsevier Oceanography Series.* New York: Elsevier.

Jerome, J. H., R. P. Bukata, and J. E. Burton. 1988. Utilizing the components of vector irradiance to estimate the scalar irradiance in natural waters. *Appl. Opt.* 27:4012-4018.

Kamykowski, D., and S. Zentara. 1986. Predicting plant nutrient concentrations from temperature and sigma-t in the upper kilometer of the world ocean. *Deep-Sea Res.* 33:89-105.

Kiefer, D. A., and B. G. Mitchell. 1983. A simple, steady state description of phytoplankton growth based on absorption cross section and quantum efficiency. *Limnol. Oceanogr.* 28:770-776.

Kirk, J. T. O. 1984. Dependence of relationship between inherent and apparent optical properties of water on solar altitude. *Limnol. Oceanogr.* 29:350-56.

Kirk, J. T. O. 1986. *Light and photosynthesis in aquatic ecosystems.* pp. 117. Cambridge: Cambridge University.

Kirk, J. T. O. 1991. Volume scattering function, average cosines, and the underwater light field. *Limnol. Oceanogr.* 36:455-67.

Kishino, M., C. R. Booth, and N. Okami. 1984. Underwater radiant energy absorbed by phytoplankton, detritus, dissolved organic matter, and pure water. *Limnol. Oceanogr.* 29:340-349.

Kishino, M., M. Takahashi, N. Okami, and S. Ichimura. 1985. Estimation of the spectral absorption coefficients of phytoplankton in a thermally stratified sea. *Bull. Mar. Sci.* 37:634-42.

Kishino, M., N. Okami, M. Takahashi, and S. Ichimura. 1986. Light utilization efficiency and quantum yield of phytoplankton in a thermally stratified sea. *Limnol. Oceanogr.* 31:557-66.

Krijgsman, J. 1994. Optical remote sensing of water quality parameters: Interpretation of reflectance spectra. Ph.D. dissertation. Delft University. Netherlands.

Langdon, C. 1988. On the causes of interspecific differences in the growth-irradiance relationship for phytoplankton. *J. Plankton Res.* 10:1291-312.

Laws, E. A., G. R. Ditullio, K. L. Carder, P. R. Betzer, and S. K. Hawes. 1990. Primary production in the deep blue sea. *Deep-Sea Res.* 37:715-730.

Lee, Z. P., K. L. Carder, S. K. Hawes, R. G. Steward, T. G. Peacock, and C. O. Davis. 1992. An interpretation of high spectral resolution remote sensing reflectance. *Optics of the Air-Sea Interface, Proc. SPIE.* 1749:49-64.

Lee, Z. P., K. L. Carder, S. K. Hawes, R. G. Steward, T. G. Peacock, and C. O. Davis. 1994a. A model for interpretation of hyperspectral remote sensing reflectance. *Appl. Opt.* 33:5721-732.

Lee, Z. P., K. L. Carder, and T. G. Peacock. 1994b. Hyperspectral modeling of

remote sensing reflectance: from the Florida Shelf to the Mississippi river. *Eos Trans. AGU* 75:193.

Lyzenga, D. R. 1978. Passive remote-sensing techniques for mapping water depth and bottom features. *Appl. Opt.* 17:379-83.

Marra, J., T. Dickey, W. S. Chamberlin, C. Ho, T. Granata, D.A. Kiefer, C. Langdon, R. C. Smith, K. S. Baker, R. R. Bidigare, and M. Hamilton. 1992. Estimation of seasonal primary production from moored optical sensors in the Sargasso Sea. *J. Geophys. Res.* 97:7399-412.

Marra, J., C. Langdon, and C. A. Knudson. 1994. Primary production and water column changes and the demise of a *phaeocystis* bloom at the Marine Light-Mixed Layers site (59°N/21°W, North Atlantic Ocean). *J. Geophys. Res.* Accepted.

Marshall, B. R., and R. C. Smith. 1990. Raman scattering and in-water ocean properties. *Appl. Opt.* 29:71-84.

Mitchell, B. G., and D. A. Kiefer. 1988. Chl-*a* specific absorption and fluorescence excitation spectra for light limited phytoplankton. *Deep-Sea Res.* 35:635-63.

Mitchell, B. G. 1990. Algorithms for determining the absorption coefficient for aquatic particles using the quantitative filter technique. *Ocean Optics X, Proc. SPIE* 1302:137-48.

Mitchell, B. G., and O. Holm-Hansen. 1991. Bio-optical properties of Antarctic Peninsula waters: differentiation from temperate ocean models. *Deep-Sea Res.* 38:1009-1028.

Mobley, C. D., B. Gentili, H. R. Gordon, Z. Jin, G. W. Kattawar, A. Morel, P. Reinersman, K. Stamnes, and R. H. Stavn. 1993. Comparison of numerical models for computing underwater light fields. *Appl. Opt.* 32:7484-504.

Montgomery K., J. J. Petrovic, and N. P. Murarka. 1994. Guidance and control of unmanned air vehicles. *Association for unmanned vehicle systems symposium.* Detroit, MI. May 23-25.

Morel, A. 1974. Optical properties of pure water and pure sea water. In *Optical aspects of oceanography,* ed. N. G. Jerlov and E. S. Nielsen, 1-24. New York: Academic.

Morel, A., and L. Prieur. 1977. Analysis of variations in ocean color. *Limnol. Oceanogr.* 22:709-22.

Morel, A. 1978. Available, usable, and stored radiant energy in relation to marine photosynthesis. *Deep-Sea Res.* 25:673-688.

Morel, A. 1980. In-water and remote measurements of ocean color. *Boundary-Layer Meteorology* 18:177-201.

Morel, A., and A. Bricaud. 1981. Theoretical results concerning light absorption in a discrete medium, and application to specific absorption of phytoplankton. *Deep-Sea Res.* 28:1375-393.

Morel, A. 1988. Optical modeling of the upper ocean in relation to its biogenous matter content (Case I waters). *J. Geophys. Res.* 93:10,749-10,768.

Morel, A., and J. F. Berton. 1989. Surface pigments, algal biomass profiles, and potential production of the euphotic layer: relationships reinvestigated in review of remote-sensing applications. *Limnol. Oceanogr.* 34:1545-562.

Morel, A., and Y. H. Ahn. 1990. Optical efficiency factors of free-living marine bacteria: Influence of bacterioplankton upon the optical properties and particulate organic carbon in oceanic waters. *J. Mar. Res.* 48:145-75.

Morel, A. 1991. Light and marine photosynthesis: a spectral model with geochemical and climatological implications. *Prog. Oceanogr.* 26:263-306.

Morel, A., and B. Gentili. 1991. Diffuse reflectance of oceanic waters: its dependence on sun angle as influenced by the molecular scattering contribution. *Appl. Opt.* 30:4427-438.

Morel, A., and B. Gentili. 1993. Diffuse reflectance of oceanic waters (2): Bi-directional aspects. *Appl. Opt.* 32:6864-879.

Nelson, J. R., and C. Y. Robertson. 1993. Detrital spectral absorption: Laboratory studies of visible light effects on phytodetritus absorption, bacterial spectral signal, and comparison to field measurements. *J. Mar. Res.* 51:181-207.

Patch, J. S., W. P. Bissett, K. L. Carder, and Z. P. Lee. 1994. Comparisons of in vivo and in vitro particulate absorption. II. Spectrophotometric determination of chl *a* concentration in the presence of chl *b*. In preparation.

Peacock, T. G., K. L. Carder, C. O. Davis, and R. G. Steward. 1990. Effects of fluorescence and water Raman scattering on models of remote-sensing reflectance. *Ocean Optics X, Proc. SPIE.* 1302:303-19.

Peacock, T. G. 1992. Some marine light sources and their effects on remote sensing reflectance models. Master's Thesis. Dept. of Marine Science, University of South Florida.

Peacock, T. G., K. L. Carder, P. G. Coble, Z. P. Lee, and S. K. Hawes. 1994. Long-path spectrometer for measuring gelbstoff absorption in clear waters. *Eos Trans. AGU* 75:22.

Pegau, W. S., and J. R. V. Zaneveld. 1993. Temperature-dependent absorption of water in the red and near-infrared portions of the spectrum. *Limnol. Oceanogr.* 38:188-92.

Petzold, T. J. 1972. Volume scattering functions for selected natural waters. *Scripps Inst. Oceanogr. Visibility Lab. SIO Ref.* 72-78.

Platt, T., C. L. Gallegos, and W. G. Harrison. 1980. Photoinhibition of photosynthesis in natural assemblages of marine phytoplankton. *J. Mar. Res.* 38:687-701.

Platt, T. 1986. Primary production of ocean water column as a function of surface light intensity: algorithms for remote sensing. *Deep-Sea Res.* 33:149-63.

Platt, T., S. Sathyendranath, C. M. Caverhill, and M. R. Lewis. 1988. Ocean primary production and available light: further algorithms for remote sensing. *Deep-Sea Res.* 35:855-79.

Platt, T., C. Caverhill, and S. Sathyendranath. 1991. Basin-scale estimates of oceanic primary production by remote sensing: the North Atlantic. *J. Geophys. Res.* 96: 15,147-15,159.

Polcyn, F. C., W. L. Brown, and I. J. Sattinger. 1970. The measurement of water depth by remote-sensing techniques. *Report 8973-26-F, Willow Run Laboratories, the University of Michigan, Ann Arbor.*

Preisendorfer, R. W. 1976. *Hydrologic optics vol. 1: introduction.* NTIS PB-259 793/8ST. National Technical Information Service, Springfield, Ill.

Roesler, C. S., M. J. Perry, and K. L. Carder. 1989. Modeling in situ phytoplankton absorption from total absorption spectra in productive inland marine waters. *Limnol. Oceanogr.* 34:1510-523.

Roesler, C .S., and M. J. Perry. 1994. A robust model for determining in situ phytoplankton absorption and fluorescence emission spectra from reflectance. *J. Geophys. Res..* Submitted.

Sathyendranath, S., and T. Platt. 1988. The spectral irradiance field at the surface and in the interior of the ocean: a model for applications in oceanography and remote sensing. *J. Geophys. Res.* 93:9270-280.

Sathyendranath, S., L. Prieur, and A. Morel. 1989a. A three-component model of ocean colour and its application to remote sensing of phytoplankton pigments in coastal waters. *Int. J. Remote Sensing* 10:1373-394.

Sathyendranath, S., T. Platt, C. M. Caverhill, R. E. Warnock, and M. R. Lewis, 1989b. Remote sensing of oceanic primary production: computations using a spectral model. *Deep-Sea Res.* 36:431-53.

Smith, R. C., and K. S. Baker. 1981. Optical properties of the clearest natural waters. *Appl. Opt.* 20:177-84.

Smith, R. C., B. B. Prezelin, R. R. Bidigare, and K. S. Baker. 1989. Bio-optical modeling of photosynthetic production in coastal waters. *Limnol. Oceanogr.* 34: 1524-544.

Spitzer, D., and R. W. J. Dirks. 1985. Contamination of the reflectance of natural waters by solar-induced fluorescence of dissolved organic matter. *Appl. Opt.* 24:444-45.

Spitzer, D., and R. W. J. Dirks. 1987. Bottom influence on the reflectance of the sea. *Int. J. Remote Sensing* 8:279-90.

Stavn, R. H., and A. D. Weidemann. 1988. Optical modeling of clear ocean light fields: Raman scattering effects. *Appl. Opt.* 27:4002-4011.

Stavn, R. H. 1990. Raman scattering effects at the shorter visible wavelengths in clear ocean waters. *Ocean Optics X, Proc. SPIE.* 1302:94-100.

Stramski, D., and A. Morel. 1990. Optical properties of photosynthetic picoplankton in different physiological states as affected by growth irradiance. *Deep-Sea Res.* 37:245-66.

Tam, A. C., and C. K. N. Patel. 1979. Optical absorptions of light and heavy water by laser optoacoustic spectroscopy. *Appl. Opt.* 18:3348-358.

Tucker, C. J., and L. D. Miller. 1977. Soil spectra contributions to grass canopy spectral reflectance. *Photogrammetric Engineering and Remote Sensing* 43(6): 721-26.

Vargo, G. A., K. L. Carder, W. Gregg, E. Shanley, and C. Heil. 1987. The potential contribution of primary production by red tides to the west Florida shelf ecosystem. *Limnol. Oceanogr.* 32:762-67.

Whitlock, C. H., L. R. Poole, J. W. Usry, W. M. Houghton, W. G. Witte, W. D. Morris, and E. A. Gurganus. 1981. Comparison of reflectance with backscatter and absorption parameters for turbid waters. *Appl. Opt.* 20:517-22.

Yentsch, C. S., and C. M. Yentsch. 1979. Fluorescence spectral signatures: the characterization of phytoplankton populations by the use of excitation and emission spectra. *J. Mar. Res.* 37:471-83.

Yentsch, C. S., and D. A. Phinney. 1985. Spectral fluorescence: an ataxonomic tool for studying the structure of phytoplankton populations. *J. of Plankton Res.* 7: 617-32.

Yentsch, C. S., and D. A. Phinney. 1992. Spectral diffuse attenuation of phytoplankton measured by the filter pad technique - are we on the right track? *Ocean Optics XI, Proc. SPIE* 1750:180-86.

Zaneveld, J. R. V. 1982. Remote sensed reflectance and its dependence on vertical structure: a theoretical derivation. *Appl. Opt.* 21:4146-150.

Zaneveld, J. R. V, J. C. Kitchen, and J. L. Mueller. 1993. Vertical structure of productivity and its vertical integration as derived from remotely sensed observations. *Limnol. Oceanogr.* 38:1384-393.

Zaneveld, J. R. V. 1994. A theoretical derivation of the dependence of the remotely sensed reflectance on the inherent optical properties. *Eos Trans. AGU* 75: 192.

APPENDICES

APPENDIX 1. EXACT SOLUTION OF NADIR $R_{rs}(0^-)$ BY THE RADIATIVE TRANSFER EQUATION

The radiative transfer equation for nadir radiance $L_u(z)$ is

$$\frac{dL_u(z)}{dz} = -cL_u(z) + L_u^* ,$$
(1)

where L_u^* is

$$L_u^* = \int_{4\pi} \beta(\alpha) L(\theta', \varphi', z) d\omega' .$$
(2)

If we separate the radiance field L into two parts: L_d for the radiance in the downwelling field, and, L_u for the radiance in the upwelling field, then Eq. 2 can be re-written as

$$L_u^* = \int_{2\pi} \beta(\alpha_b) L_d d\omega' + \int_{-2\pi} \beta(\alpha_f) L_u d\omega' .$$
(3)

Define the light-averaged-backward-VSF $\overline{\beta}_b$ and VSF-averaged-upwelling-radiance $\overline{L}_u$ similarly to Zaneveld [1982, 1994], respectively:

$$\overline{\beta}_b = \frac{\int_{2\pi} \beta(\alpha_b) L_d(\theta') d\omega'}{\int_{2\pi} L_d(\theta') \cos(\theta') d\omega'} ,$$

$$\overline{L}_u = \frac{\int_{-2\pi} \beta(\alpha_f) L_u(\theta') d\omega'}{\int_{-2\pi} \beta(\alpha_f) d\omega'} ,$$
(4)

then Eq. 1 becomes

$$\frac{dL_u(z)}{dz} = -cL_u(z) + \overline{\beta}_b E_d + \overline{L}_u(z)b_f \ . \tag{5}$$

If we define the diffuse-attenuation-coefficient for nadir-viewed radiance L_u as

$$k_L(z) = -\frac{dL_u(z)}{L_u(z)dz} \ , \tag{6}$$

then from the R_{rs} definition, the nadir in-water remote-sensing reflectance $R_{rs}(0^-)$ is

$$R_{rs}(0^-) \equiv \frac{\overline{\beta}_b}{c + k_L(0^-) - \epsilon b_f} \ , \tag{7}$$

where

$$\epsilon = \frac{\overline{L}_u}{L_u} \ . \tag{8}$$

APPENDIX 2. DIFFUSE ATTENUATION COEFFICIENT OF AN EXTENDED LAMBERTIAN RADIANCE SOURCE
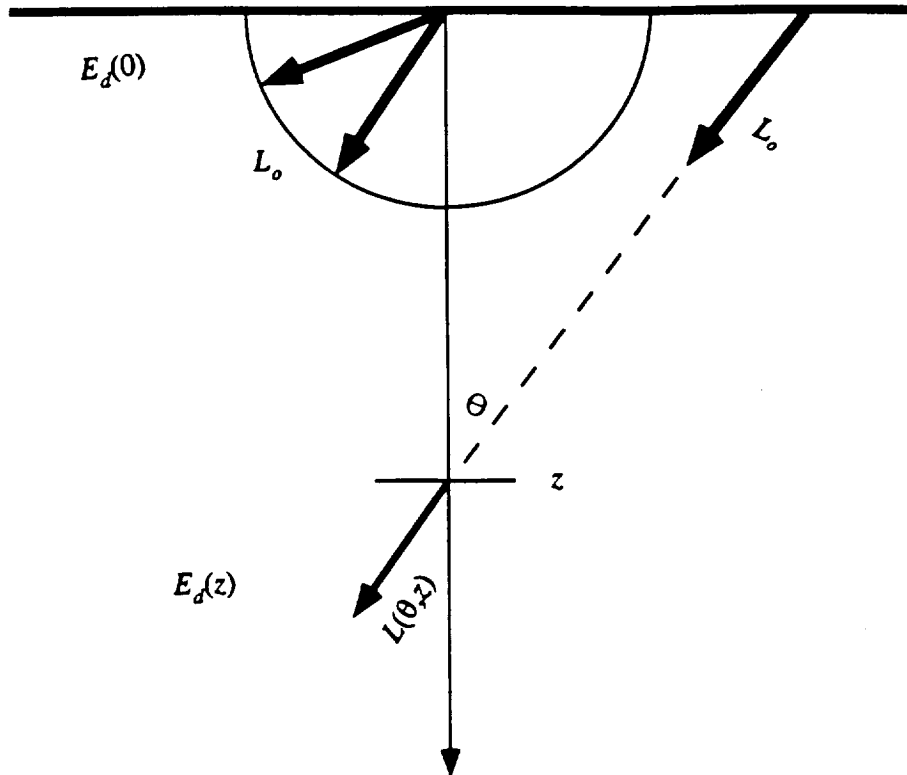

Figure 28. Schematic light field of an extended Lambertian source.

Figure 28 illustrates the light field illuminated by an extended Lambertian source. L_o is the source radiance and it is the same for all directions. Define k as the diffuse attenuation coefficient of radiance, then the radiance at distance z in direction Θ is

$$L(\theta,z) = L_o e^{-\frac{kz}{\cos(\theta)}} ,$$

(1)

and the irradiance at that distance is

$$E_d(z) = 2\pi L_o \int_0^{\frac{\pi}{2}} e^{-\frac{kz}{\cos(\theta)}} \cos(\theta)\sin(\theta)d\theta \ . \tag{2}$$

Notice that the source irradiance is

$$E_d(0) = \pi L_o \ , \tag{3}$$

then,

$$\frac{E_d(z)}{E_d(0)} = 2\int_0^{\frac{\pi}{2}} e^{-\frac{kz}{\cos(\theta)}} \cos(\theta)\sin(\theta)d\theta \ . \tag{4}$$

From Gordon [1989a], we have

$$\frac{E_d(z)}{E_d(0)} \approx e^{-1.08D_d(0)\kappa z} \ , \tag{5}$$

and for a Lambertian distribution, $D_d(0) = 2$, so

$$e^{-2.16\kappa z} \approx 2\int_0^{\frac{\pi}{2}} e^{-\frac{kz}{\cos(\theta)}} \cos(\theta)\sin(\theta)d\theta \ . \tag{6}$$

Define $k = \zeta\kappa$, $\kappa z = \tau$, then for τ in the range of 0.5 to 2.0, ζ varies from 1.37 to 1.62 for Eq. 6 to hold. So, in a general case, $\zeta \approx 1.5$ is used as an average.

Also, from Eq. 36, for bottom albedo $\rho = 0.5$, $\tau = 0.5$ means $R_{rs}^b \approx 0.022$ sr^{-1}, and $\tau = 2$ means $R_{rs}^b \approx 0.0004$ sr^{-1}. If the average remote-sensing reflectance from the water column is 0.005 sr^{-1}, $\tau = 0.5$ means R_{rs}^b may contribute $\sim 99\%$ of the total signal, and $\tau = 2$ means R_{rs}^b contribute less than 10% of the total signal, which indicates 0.5 to 2 of τ is the general range where remote-sensing reflectance from the bottom could be verified.

APPENDIX 3. REMOTE-SENSING REFLECTANCE FROM GELBSTOFF FLUORESCENCE (R_{rs}^f) AND WATER RAMAN SCATTERING (R_{rs}^R)

For z positive downward from the surface (Figure 5), with the consideration of isotropic β_{ie}, to first order the inelastic radiance $(L_{u,ie})$ in the direction Θ and the upwelling irradiance $(E_{u,ie})$ at depth z due to the depth interval dz are simplified to

$$dL_{u,ie}(z,\theta,\lambda) = \int_{\lambda_x} \beta_{ie}(\lambda_x,\lambda)E_o(z,\lambda_x)d\lambda_x \frac{dz}{\cos(\theta)}, \qquad (1)$$

and

$$
\begin{aligned}
dE_{u,ie}(z,\lambda) &= -2\pi \int_{\pi/2}^{\pi} dL_{u,ie}(z,\theta,\lambda)\cos(\theta)\sin(\theta)d\theta \\
&= 2\pi \int_{\lambda_x} \beta_{ie}(\lambda_x,\lambda)E_o(z,\lambda_x)d\lambda_x dz,
\end{aligned}
\qquad (2)
$$

where $E_o(z,\lambda_x)$ is the scalar irradiance at depth z, and $E_o(z,\lambda_x) = E_{od}(z,\lambda_x) + E_{ou}(z,\lambda_x) \approx D_d(1+2R(\lambda_x))E_d(z,\lambda_x)$. Considering that $R(\lambda_x)$ is small (<0.05) and $D_u/D_d \approx 2$ [Gordon et al. 1975] is independent of depth, the subsurface irradiance due to the inelastic scattering for a deep water column is

$$E_{u,ie}(0^-,\lambda) \approx 2\pi \int_{\lambda_x} \frac{\beta_{ie}(\lambda_x,\lambda)E_d(0^-,\lambda_x)}{2\kappa(\lambda)+\kappa(\lambda_x)}d\lambda_x. \qquad (3)$$

Defining Q_{ie} as the "Q factor" for the inelastic scattering field, the subsurface upwelling radiance due to inelastic scattering is

$$L_{u,ie}(0^-,\lambda) \approx \frac{2\pi}{Q_{ie}} \int_{\lambda_x} \frac{\beta_{ie}(\lambda_x,\lambda)E_d(0^-,\lambda_x)}{2\kappa(\lambda)+\kappa(\lambda_x)} d\lambda_x. \qquad (4)$$

The inelastic total scattering coefficient $\psi(\lambda_x,\lambda)$ (m^{-1}/nm) is defined as

$$\psi(\lambda_x,\lambda) = \int_{4\pi} \beta_{ie}(\alpha,\lambda_x,\lambda)d\omega. \qquad (5)$$

Since $\beta_{ie}(\alpha,\lambda_x,\lambda)$ is considered isotropic, then

$$\psi(\lambda_x,\lambda) = 4\pi\beta_{ie}(\lambda_x,\lambda). \qquad (6)$$

According to the definition of remote-sensing reflectance, with Eq. 4 and Eq. 6, we have

$$R_{rs,ie}(\lambda) \approx \frac{t^2}{2Q_{ie}n_w^2} \int_{\lambda_x} \frac{\psi(\lambda_x,\lambda)E_d(0^-,\lambda_x)}{[2\kappa(\lambda)+\kappa(\lambda_x)]E_d(0^-,\lambda)} d\lambda_x. \qquad (7)$$

For gelbstoff fluorescence, defining $\eta(\lambda_x)$ as the quantum efficiency for the emission band excited by λ_x, then [Gordon 1989, Carder and Steward 1985]

$$\eta(\lambda_x) = \int_\lambda \frac{\lambda}{\lambda_x} \frac{\psi(\lambda_x,\lambda)}{a_g(\lambda_x)} d\lambda. \qquad (8)$$

$\psi(\lambda_x,\lambda)$ can be characterized by a log-normal curve [Hawes et al. 1992], so

$$\psi(\lambda_x,\lambda) = \frac{\eta(\lambda_x)\lambda_x a_g(\lambda_x)}{\lambda A} e^{-s\left[\ln\frac{\lambda-\lambda_f}{\sigma}\right]^2}, \qquad (9)$$

in which

$$A = \int_\lambda e^{-s\left[\ln\frac{\lambda-\lambda_f}{\sigma}\right]^2} d\lambda, \tag{10}$$

where $\eta(\lambda_x)$, λ_f, s and σ may vary with the type of gelbstoff and λ_x.

In general, $b_b < < a$ for most oceanic waters [Morel and Prieur 1977], so κ is close to a. And, based on the calculation for chlorophyll a fluorescence made by Gordon [1989], the Q_{ic} factor for inelastic scattering is ~ 3.7. Then combining Eq. 7 and Eq. 9 with $t \approx 0.98$, $n_w \approx 1.34$, the remote-sensing reflectance due to gelbstoff fluorescence can be reduced to

$$R_{rs}^f(\lambda) \approx 0.072 \int_{\lambda_x} \eta(\lambda_x) \frac{\lambda_x}{\lambda} \frac{a_g(\lambda_x)E_d(0^-,\lambda_x)}{[2a(\lambda)+a(\lambda_x)]E_d(0^-,\lambda)} \frac{e^{-s\left[\ln\frac{\lambda-\lambda_f}{\sigma}\right]^2}}{A} d\lambda_x. \tag{11}$$

Unlike broad-band (~ 100 nm) gelbstoff fluorescence, the water Raman emission has a half-band width of about 20 nm [Collins et al. 1984]. Omitting this band width, i.e. assuming a narrow Raman emission, the inelastic scattering coefficient $\psi(\lambda_x,\lambda)$ for water Raman can be related to Raman scattering coefficient as

$$\psi(\lambda_x,\lambda)d\lambda_x = b^R(\lambda_x)$$

and from Eq. 7, with $\kappa \approx a$, the remote-sensing reflectance for water Raman is

$$R_{rs}^R(\lambda) \approx 0.072 \frac{b^R(\lambda_x)E_d(0^-,\lambda_x)}{[2a(\lambda)+a(\lambda_x)]E_d(0^-,\lambda)}. \tag{12}$$